Macrophage-hitchhiking Anisotropic Microparticles for Therapeutic and Diagnostic Applications

By

Li-Wen Wang

B.Sc. in Materials Science and Engineering
National Tsing Hua University (NTHU), Hsinchu, Taiwan, 2014
M.Sc. in Materials Science and Engineering
National Tsing Hua University (NTHU), Hsinchu, Taiwan, 2016

Submitted to the Harvard-MIT Program in Health Science & Technology
in partial fulfillment of the requirements for the
degree of
Doctor of Philosophy in Medical Engineering and Medical Physics
at the
Massachusetts Institute of Technology

February 2023

Author _____
Harvard-MIT Program in Health Sciences and Technology
Jan 24, 2023

Certified by _____
Samir Mitragotri, PhD
Hiller Professor of Bioengineering at Harvard University
Wyss Professor of Biologically Inspired Engineering at Harvard University
Thesis Supervisor

Accepted by _____
Collin M. Stultz, MD, PhD
Director, Harvard-MIT Program in Health Sciences and Technology
Nina T. and Robert H. Rubin Professor in Medical Engineering and Science
Professor of Electrical Engineering and Computer Science

Thesis Supervisor:
Samir Mitragotri, PhD
Hiller Professor of Bioengineering at the John A. Paulson School of Engineering and Applied Sciences, Harvard University

Thesis Committee Chair:
Sangeeta Bhatia, MD, PhD
John J. and Dorothy Wilson Professor at the Electrical Engineering & Computer Science and Institute for Medical Engineering & Science, MIT

Thesis Readers:
David J. Mooney, PhD
Robert P. Pinkas Family Professor of Bioengineering at the John A. Paulson School of Engineering and Applied Sciences, Harvard University

Jeffrey Karp, PhD
Professor, Anaesthesia, Brigham and Women's Hospital and Harvard Medical School

Macrophage-hitchhiking Anisotropic Microparticles for Therapeutic and Diagnostic Applications

by

Li-Wen Wang

Submitted to the Harvard-MIT Program in Health Sciences and Technology in Partial Fulfillment of the Requirements for the Degree of Doctor of Philosophy in Medical Engineering and Medical Physics

ABSTRACT

Cell therapies represent a major paradigm shift of biotechnology in medicine due to its transformative potential in treating previously incurable diseases. A variety of cells have been applied for cell therapies, including stem cells, tissue-specific cells, and hematopoietic cells. Particularly, immune cells, a subset of blood cells, have gained significant attention owing to their inflammation-homing ability as well as inherently critical roles in disease progression and tissue regeneration. The prosperity of immune cell-based therapies in the clinic has fueled the efforts in immune cell engineering. Several approaches have been taken to functionalize immune cells, among which biomaterial-assisted cellular platforms, marrying the strengths of biomaterials and leukocytes, become a new pillar of immune cell engineering. In my thesis work, I provide a brief overview on the cell therapies in the clinic, followed by introducing two projects of biomaterial-assisted cellular platforms, where anisotropic microparticles and macrophage, a type of innate immune cells, were employed. Specifically, I developed and engineered discoidal microparticles that can hitchhike on the macrophage surface but resist phagocytosis due to their anisotropic morphology. This approach takes advantage of inflammation-homing capability of macrophages and enables stable loading of therapeutic and imaging agents in the extracellular space for therapeutic and diagnostic applications.

Thesis Supervisor: Samir Mitragotri
Title: Hiller Professor of Bioengineering and Wyss Professor of Biologically Inspired Engineering at Harvard University.

Acknowledgements

To Samir, I will be forever grateful for your strong supports, mentorship, and all the learning opportunities you provided throughout my PhD. I am honored to be your first student after you moved to Boston and your first HST student. You are such a genuinely kind person full of wisdom. I am always amazed by your insights into science as well as your advice on research, career development, and life. Having the chance to be your mentee is the best thing that happened to me during PhD. I have learned so much from you, but I know I still have so much to learn. You will definitely be my mentor of life!

To Wyatt, you are such a genuinely kind, brilliant, and warm person. I sincerely appreciate your mentorship when I first joined the lab and your kindness that helped me adapt to the new environment. Thank you for being my good colleague and good friend during PhD. I believe we will be lifelong friends!

To Neha, my sister in the lab, you have helped me and supported me in so many ways. I am glad that we shared tons of sweet memories together and supported each other through multiple tough situations. I do not know how to express my appreciation to you, but I will be there to support you whenever you need me!

To Yongsheng, thank you for always being willing to help me and provide your advice when I need you! You are such a wonderful colleague and friend. I know you will have a fantastic career in the upcoming future!

To Zongmin, you are the scientific wizard in our lab! Your projects are all amazing. I sincerely appreciate your guidance and advice on coordinating people for writing the review paper. Also, thank you for showing and teaching me lots of useful lab techniques!

I would like to thank the team who helped me with the pig studies, including Neha, Supriya, Ninad, Suyog, Morgan, Charles, Kolade, Michael, Rick, and Vinny. Special thanks to Vinny for spending so many late nights with me to develop the procedure for MRI analysis.

I also want to thank all my lab members (both alumni and current members) for their supports, helps, and advice. With you all, we have formed such a wonderful Mitragotri family filled with love, joy, kindness, and supports.

To my collaborators at Boston Children's Hospital - - Dr. Mannix, you are so kind and supportive. Without your advice and coordination, there is no way for us to achieve such a great milestone for the imaging project. I am sincerely grateful to have the chance to work with you. Masen, thank you for always being so nice and accommodating. I really enjoyed the times we worked with each other. All the best for your next journey! Camilo, thank you for always being so enthusiastic and providing so many insights from clinical radiology perspective. I have learned so much from you!

To my committee members - - Prof. Sangeeta Bhatia, Prof. David Mooney, and Prof. Jeff Karp, you all are wonderful! Thank you so much for your participation, advice, and guidance along the way. I have learned how to see things from different interesting perspectives because of you!

To the director of Education and Senior Lecturer at HST, Julie, you have always been one of the strongest supports to me in these few years. I sincerely appreciate your advice on finding the lab and your supports when I was struggling. Thank you so much!

I also want to thank my friends in Taiwan who have gave me tons of encouragements, love, and supports during the darkest period of my life. You helped me survive and get through all the pain and suffering. The only thing I can do to pay you back is to be your loyal friend forever!

To my sister, mom, and dad, I am always fearless and dare to dream because I know you all will be my strongest support and hold me tight when I fall. I am sorry that I cannot physically be with you in the past few years and thank you for your understanding. You know all the ups and downs of my PhD journey, and I hope I make you proud. I love you!!!

There are so many people who have/had participated in my PhD journey and have provided me with tons of love, supports, and guidance. It is not possible to name everyone, but I just want to let you know that I remember every single piece of sweet memories with you all and I will cherish them for life.

Table of Contents

List of Figures

List of Tables

Chapter 1: Overview

Cell therapies represent a major paradigm shift in biotechnology due to its transformative potential in addressing previously untreatable diseases (*1-3*). Indeed, it offers unique advantages over conventional small molecules and the growing number of biologics. Specifically, living cells can simultaneously respond to both local or systemic stimuli (e.g., chemical, physical, and biological cues), overcome biological barriers (*4*), target and interact with specific cell types and tissues (*5*), and serve as a template to be modified with additional functions (e.g. cellular hitchhiking, genetic engineering) (*6-8*). A variety of cells have been applied for cell therapies, including stem cells, tissue-specific cells, and blood cells (*9-11*). Among them, immune cells have gained significant attention due to their inflammation-homing ability (*12*) and inherently critical roles in disease progression (*13, 14*) and tissue regeneration (*15*).

The proven success of immune cell-based therapies in the clinic has energized the field of cellular engineering with the aim of endowing cells with additional functions. Several approaches have been used to engineer immune cells in the clinical settings, including *i*) ex vivo education by incubating cells with soluble factors (*16, 17*), *ii*) in vivo condition by co-administrating supporting adjuvant drugs in a bolus form with cells (*18, 19*), and *iii*) cell programming via genetic engineering (*20, 21*). While the first two strategies mainly induce transient effects (*22*), genetic engineering offers a more robust and persistent cell reformation based on cellular biochemistry (*23*). However, it is impossible to genetically modify cells with non-biological substances (e.g., non-biological small molecules, imaging agents, and synthetic polymers) (*24*). Biomaterials provides a new means to engineer cells. Specifically, biomaterials can be loaded with a wide range of cargos (*25-28*), prevent biological cargos from being damaged or compromised in the harsh environment (*29*), release the cargos in a responsive manner (*30*), provide biomechanical cues and/or structural support to the cells (*31*), modulate functions or phenotypes of adoptively transferred cells in vivo (*32*), and interact with host immunity for immunomodulation (*33*). Hence, material-assisted immune cell therapies, marrying the strengths of biomaterials and leukocytes, provided an opportunity to broaden the applications of immune cell-based technologies.

In my thesis work, I provide a brief overview on the cell therapies in the clinic, followed by introducing two projects of biomaterial-mediated cellular platforms. I open my thesis in Chapter 2 by providing a snapshot of the clinical landscape of cell therapies. 33 cell therapy products approved for clinical use and 1705 clinical trials employing cells for therapeutic purposes were identified. I highlighted the approved cell products and discussed their applications as well as summarize the current clinical trials based on their cell type, indication, source, and phase.

In Chapter 3, I described my work in collaboration with Dr. Wyatt Shields, where we introduced a cytokine-loaded discoidal microparticle that can attach on the immune cell surface without phagocytosis. I designed the flow panel for immunophenotyping, and we showed that controlled release of cytokines can modulate cell phenotype in vitro. We further demonstrated the cell fate and effector functions of immune cells can be modulated and maintained in vivo using a mouse model with the final application as cancer therapy.

In Chapter 4, I describe my principal work, where I expanded the application of cell-hitchhiking micro-disks to the imaging field. I developed hydrogel-based discoidal microparticles, where MRI contrast agents were loaded. I also engineered a methodology to fabricate hydrogels, made of biomolecules with a high molecular weight and viscosities, into microparticles of a subcellular size at scale. I further examined the contrast efficacy of the

system in vitro and demonstrated the potential of biomaterial-mediated cellular platforms in diagnosing CNS disorders using a pig model of mild traumatic brain injury.

Finally, I conclude my thesis in Chapter 5 with a summary of conclusions drawn from the data and future perspectives.

Permissions and Attributions:

1. Content from Chapter 2 was adapted from ref (*34*), published in the *Bioengineering and Translational Medicine*.
2. Content from Chapter 3 was adapted from ref (*32*), published in the *Science Advances*.
3. Content from Chapter 4 has been submitted to *Science Translational Medicine* for review.

Chapter 2: Clinical Landscape of Cell Therapies

2.1 Clinically Approved Products

The global market for cell therapy is predominantly shared by stem cells and tissue-specific cells (e.g., skin cells, chondrocytes), followed by blood cells (*35-37*). Current approved stem-cell therapies include hematopoietic stem cells (HSCs), mesenchymal stem cells (MSCs), and to a lesser extent limbal stem cells (LSCs). HSC products are predominantly approved for the treatment of blood disorders. MSC therapies are indicated for a broad variety of diseases, including cardiovascular diseases, graft versus host diseases (GvHD), degenerative disorders, and inflammatory bowel diseases. The single LSC product is approved for LSC deficiency. Distinct from stem cell products, terminally differentiated tissue-specific cells are mainly used for regenerative medicine and tissue engineering applications, such as autologous skin cells (i.e., keratinocytes, fibroblasts, and melanocytes) for the treatment of thermal burns (*38*), bi-layers of living cellular skin substitute for venous leg ulcers and diabetic foot ulcers (*39*), and autologous chondrocyte scaffolds for repair of cartilage defects (*40*). These tissue-specific-cell therapies are beyond the scope of this section because they are mostly applied as tissue scaffolds instead of use as a single-cell suspension, and they have been extensively reviewed elsewhere (*9, 41, 42*). The third group of cell therapies consist of blood cells, including leukocytes, red blood cells (RBCs), and platelets; however, only T cells and dendritic cells (DCs) have been approved as therapeutic products in the market to date. Most approved T cell products are chimeric antigen receptor (CAR)-T therapies for hematologic malignancies, whereas DC products are used as vaccines for solid cancers. Of note, RBCs and platelets, while not associated with a specific product, are widely used in clinical settings for blood transfusions (*43*). In addition, the cell source of these approved products can be originated either from the patients themselves (autologous) or other donors (allogeneic).

In the following sub-sections, I provide additional details on approved cell therapy products that presently include T cells, stem cells, and DCs **(Table 2.1)**. I also discuss closely related modalities, namely the applications of donor blood products and microbe-based therapies in the clinic. Of note, many of these approved cell therapies are being developed and evaluated in current trials for additional indications, as summarized in **Table 2.2**.

2.1.1 T cells

A total of seven T cell products have been approved globally as of 2022, six by the FDA (USA) and one by the Korea Food & Drug Administration (KFDA) **(Table 2.1)**. All FDA-approved T cell products are for ***CAR-T therapy***, which is a form of immunotherapy that uses T cells genetically modified with a chimeric antigen receptor (CAR) to recognize and destroy cancer cells (*44*). The two essential components of a CAR include *i*) an *extracellular target binding* domain used to identify surface antigens on cancer cells, and *ii*) an *intracellular signaling* portion comprised of costimulatory and activation domains that initiate processes including activation, clonal expansion, and cell killing (*45*). New functional domains are now being explored in both preclinical and clinical settings with the aim of providing safer and more effective CAR-T therapies. Of note, all approved CAR-T products are autologous and contain CARs targeting either CD19 or B-cell maturation antigen (BCMA), biomarkers that are selectively expressed on the surface of B cells. Accordingly, CAR-T cells are indicated for relapsed or refractory (r/r) B-cell malignancies.

Kymriah®, approved by the FDA in 2017, was the first T-cell therapy available in the US (*46*). Kymriah®, CD19-targeted CAR-T therapy, is indicated for the treatment of children and young adults with r/r B-cell precursor acute lymphoblastic leukemia (r/r B-cell ALL) and adult

patients with certain types of r/r large B-cell lymphoma after the failure of at least two lines of systemic therapy. Another CD19-targeted CAR-T therapy, Yescarta®, also received FDA approval in 2017 for the treatment of certain types of r/r large B-cell lymphoma in adult patients who resist two or more lines of systemic therapy. Both Kymriah® and Yescarta® are being investigated in current clinical trials for additional indications (e.g., liquid cancers, lymphomas, **Table 2.2**). Though both targeting to CD19, notable differences between Kymriah® and Yescarta® include their costimulatory domains (4-1BB vs. CD28) and the associated persistence of the infused CAR-T cells (1-7 years vs. < 6 weeks) (*47, 48*). In 2020, a third CAR-T product also targeting to CD19, Tecartus™, received approval from the FDA to treat adults with r/r mantle cell lymphoma (MCL), which is an aggressive, rare form of non-Hodgkin lymphoma. Unlike the two previously approved CAR-T therapies, the Tecartus™ manufacturing process incorporates an additional step to enrich the T cell population and remove circulating tumor cells (CTCs) from patients' leukapheresis material. This process prevents CAR-T cell activation and subsequent exhaustion during *ex vivo* manufacturing (*49*). Of note, in April 2022, Yescarta® received FDA approval as first CAR T-cell therapy for initial treatment of r/r large B-cell lymphoma, i.e., serving as the treatment after the failure of first-line chemoimmunotherapy. Shortly after this announcement, Breyanzi® received FDA approval for the same indication yet with a broader patient population. In addition to CAR-T cells targeting CD19, BCMA-targeted CAR-T cells also made their way to the market. Abecma® and Carvykti™, respectively approved by the FDA in 2021 and 2022, were indicated for the adult patients with r/r multiple myeloma after four or more prior lines of therapy, including an immunomodulatory agent, a proteasome inhibitor, and an anti-CD38 monoclonal antibody.

Although CAR-T products are indicated solely for hematological malignancies, other T cells have been used to treat solid tumors. ImmunCell-LC®, an autologous cytokine-induced-killer (CIK) cell–based immunotherapy, was approved by the KFDA in 2007 and earned orphan drug designation from the FDA in 2018. It is employed as an adjuvant therapy after tumor resection and has been used for the treatment of hepatocellular carcinoma, brain tumors, and pancreatic cancer by eliminating residual tumor cells. ImmunCell-LC® is manufactured by isolating PBMCs and incubating them with interleukin-2 (IL-2) and anti-CD3 antibody (*50*), to collect activated T lymphocytes. ImmunCell-LC® showed an increased rate of recurrence-free and overall survival in patients who underwent tumor resection (*51*). Additional clinical trials of ImmunCell-LC® are underway for hepatocellular carcinoma.

2.1.2 Stem cells

My search revealed a total of 22 stem cell products that have been approved globally, with 12 approved by the FDA (USA) or European Medicines Agency (EMA, Europe). The remaining products are mainly approved in other countries, particularly in Asia **(Table 2.1)**. Notably, all but one product are composed of HSCs or MSCs.

2.1.2.1 Hematopoietic stem cells (HSCs)

There are 11 approved HSC products globally, with 10 approved by the FDA as of 2022 **(Table 2.1)**. The FDA approved the first batch of products, Allocord and Hemacord™, in 2011. Subsequently, six more similar products were FDA approved, with the most recent in 2018. All these products are cord blood-based therapies that have applications for malignant and non-malignant blood disorders and immunodeficiency disorders. Notably, cord blood-based HSCs offer considerable advantages over other forms of allogeneic HSCT, such as easier accessibility, higher tolerance for human leukocyte antigen (HLA) mismatch, and a lower risk of GvHD (*52*).

While pediatric HSCT is still exclusively performed with HLA-matched cord blood from a sibling (*53*), the tolerance for 1-2 HLA-A, -B and -DR mismatches has loosened to enable the considerable expansion of the HSCT-eligible adult patient population.

In addition, Strimvelis®, Zynteglo™, and Skysona are autologous HSC-based gene therapies. Strimvelis®, EMA approved in 2016, is indicated for adenosine deaminase deficiency (ADA-SCID), an immunodeficiency disorder caused by mutations in the gene coding for adenosine deaminase (ADA). Zynteglo™ received EMA and FDA approval in 2019 and 2022, respectively. It is employed for transfusion-dependent thalassemia, a genetic disorder caused by mutations in the β-globin gene that result in considerably reduced or absent adult hemoglobin. Zynteglo™ uses the lentiviral vector LentiGlobin BB305 to transduce autologous CD34+ cells with the β-globin gene. These cells are then infused back to the patient and traffic to the bone marrow, where they differentiate into mature RBCs with functional hemoglobin (*54*). Several current clinical trials are exploring the use of LentiGlobin BB305 for applications including thalassemia and sickle cell disease. In 2022, Skysona received FDA approval as the treatment for the male patients aged 4-17 years with early, active cerebral adrenoleukodystrophy (CALD). Before Skysona, the only treatment for CALD was an allogeneic HSC transplant that requires a matching donor. However, Skysona is prepared by patient's own HSCs via ex vivo transduction with the Lenti-D lentiviral vector to add functional ABCD1 genes, with the goal of slowing the progression of neurologic dysfunction in CALD patients.

2.1.2.2 Mesenchymal stem cells (MSCs)

There are 10 MSC products that have been approved globally as of 2022 **(Table 2.1)**, although none have been approved by the FDA. The current MSC products fall into two major categories according to their mechanisms of action and approved indications: *i)* tissue repair, and *ii)* immunomodulation.

MSCs have multipotent potential and can differentiate into a variety of cell types, such as osteoblasts, chondrocytes, myocytes, adipocytes, and neuronal cells (*55, 56*). Based on this biological function, three MSC therapies have been approved for tissue repair applications **(Table 2.1)**. Cellgram™, an autologous MSC therapy, was approved by the KFDA in 2011 for acute myocardial infarction. Mechanisms of action of Cellgram™ are reported to involve *i)* MSCs' capability to differentiate into cardiac myocytes, and *ii)* MSCs' pleiotropic secretomes that promote angiogenesis (*57*). Another MSC-based tissue repair product, Cartistem®, was approved by the KFDA in 2012 for repetitive and/or traumatic cartilage degeneration, including degenerative osteoarthritis (*58*). Queencell®, an autologous adipose-derived cell product, was also approved by the KFDA, in 2010, for the treatment of subcutaneous tissue defects. However, unlike other approved MSCs, Queencell® is not composed of pure MSCs and is instead comprised of a mixture of MSCs, pericytes, mast cells, fibroblasts, and endothelial progenitor cells.

MSCs also have immunomodulatory capabilities that can be used to regulate immune responses in many pathologies. Based on this capability, 7 MSC products have been approved for indications including Crohn's fistula (Alofisel®, Cupistem®), acute GvHD (aGvHD) (Prochymal®, TEMCELL®), amyotrophic lateral sclerosis (ALS) (NeuroNata-R®), spinal cord injury (Stemirac), and critical limb ischemia due to Buerger's disease (Stempeucel®) **(Table 2.1)**. Alofisel®, an allogeneic MSC therapy for complex perianal fistula in Crohn's disease, is the only MSC product approved by the EMA. Its mechanism of action seems to involve MSCs'

ability to inhibit the proliferation of activated lymphocytes and thereby reduce pro-inflammatory cytokine production (*59*). A similar product, Cupistem®, is an autologous adipose-derived MSC product that received approval from the KFDA in 2012 to treat patients with Crohn's fistula. In 2012, Prochymal® received approval from the Canadian Food Inspection Agency (CFIA) for the treatment of steroid-refractory acute GvHD (SR-aGvHD) in pediatric patients. Of note, Prochymal® showed evidence of safety, tolerability, and efficacy as a first-line therapy after initial steroid failure in pediatric patients with SR-aGvHD in a Phase 3 trial (*60*). However, the FDA denied its approval in 2020 and recommended at least one more randomized controlled trial in adults and/or children to provide additional information about the therapeutic mechanism and efficacy.

A few of these MSCs (e.g., Cellgram™, Cartistem®, Prochymal®) are being evaluated in current clinical trials for additional indications including alcoholic liver cirrhosis, acute respiratory distress syndrome (ARDS) due to coronavirus disease, and osteochondral lesions **(Table 2.2)**. In addition to the approved HSC and MSC products, Holoclar®, an autologous LSC product, won EMA approval in 2015 for the treatment of LSC deficiency secondary to ocular burns. However, since Holoclar® is given to patients in the form of a cornea sheet rather than a single-cell suspension, it is not within the scope of the analysis.

2.1.3 Dendritic cells (DCs)

There are currently three DC products in the global market with approvals by the FDA, KFDA, and Indian FDA **(Table 2.1)**. Provenge® won FDA approval in 2010 for the treatment of metastatic castrate-resistant prostate cancer. Of note, it is the first cell therapy used as a cancer vaccine in the US (*61*). To produce Provenge®, the patient's leukocytes are collected and then expanded *ex vivo* with a prostate cancer tissue antigen (prostatic acid phosphatase (PAP)) and granulocyte macrophage colony-stimulating factor (GM-CSF). This autologous multi-cell suspension composed primarily of DCs, but also other leukocytes, is administered intravenously in three doses, each separated by two weeks. The main mechanism of action is the DC-mediated presentation of PAP to the patient's T cells, which elicits an adaptive immune response against the prostate cancer cells. While Provenge® is the only DC therapy approved by the FDA, CreaVax®, an autologous DC therapy, was approved by the KFDA in 2007 for renal cell carcinoma. Similarly, APCeden® is an autologous DC therapy approved by the Indian FDA in 2017 for the treatment of prostate, ovarian, colorectal, and non-small cell lung cancers.

2.1.4 Other cell-based therapies (Transfusions, Transplants, and Supplements)

While donor blood products have a long history in the treatment of some blood disorders and deficiencies (*43*), there are no specific approved products for RBCs and platelets. RBCs are administered to patients who are anemic due to a blood disorder (i.e., thalassemia, sickle cell disease, iron or other vitamin deficiency, aplastic anemia), or as a result of trauma or injury. Prior to intravenous administration, blood must be ABO and RhD matched. Packed RBC infusions are given most commonly, although whole blood can also be administered. In many cases, autologous blood is isolated prior to a surgical procedure in anticipation of potential blood loss. Currently, drugs cannot be mixed with donor blood prior to infusion. Platelet transfusions are indicated for the treatment of thrombocytopenia, which can occur as a result of disease or in response to cancer treatment. Current clinical studies continue to investigate the range of suitable storage conditions and dosing regimens for donor platelets.

FDA approved first microbiota-based treatment, Reybota™, in Dec 2022. Reybota™ is a type of fecal microbiota transplant (FMT), in which a solution of fecal matter from a healthy donor is supplied to the intestinal tract of the patient. It is used to restore the microbiome balance after *Clostridioides difficile* infection (CDI) and prevention of recurrence of CDI in adult patients, following antibiotic treatment for recurrent CDI. In addition to FMT, another closely related modalities currently used in the clinic is probiotics, which includes living microorganisms that are widely available over the counter and can also be prescribed by clinicians (*62-64*). However, they are also beyond the scope of this section because they are typically categorized as foods, functional foods, or supplements, and as such do not undergo the same regulatory process as pharmaceuticals (*65*).

Table 2.1: Clinically approved cell therapies, grouped by cell type as of 2022.

Name / Trade Name (Manufacturer)	Cell Source	Approved Indications	Approval Year	Notes
T Cell				
Tisagenlecleucel / Kymriah® (Novartis)	Autologous	[adult patients] relapsed or refractory (r/r) follicular lymphoma or diffuse large B-cell lymphoma (DLBCL) after two or more lines of therapy [pediatric and young adult (≤25 years of age) patients] r/r acute lymphoblastic leukemia (ALL)	2017 (USFDA), 2018 (EMA), 2018 (Health Canada), 2019 (JMHW), Australia, Israel, Switzerland	GM; CAR/CD19 (receptor/ target)
Axicabtagene ciloleucel / Yescarta® (Kite)	Autologous	[adult patients] r/r large B-cell lymphoma after two or more lines of systemic therapy or first-line chemoimmunotherapy	2017 (USFDA), 2018 (EMA), 2019 (Health Canada)	GM; CAR/CD19 (receptor/ target)
Brexucabtagene autoleucel / Tecartus™ (Kite)	Autologous	[adult patients] r/r mantle cell lymphoma (MCL) or r/r B-cell precursor acute lymphoblastic leukemia (ALL)	2019 (Orphan Medicine Designation by EMA), 2020 (USFDA)	GM; CAR/CD19 (receptor/ target)
Lisocabtagene maraleucel / Breyanzi® (Juno Therapeutics)	Autologous	[adult patients] r/r large B-cell lymphoma after two or more lines of systemic therapy or first-line chemoimmunotherapy	2022 (USFDA) 2022 (EMA)	GM; CAR/CD19 (receptor/ target)
Idecabtagene vicleucel / Abecma® (Celgene)	Autologous	[adult patients] r/r multiple myeloma after four or more prior lines of therapy	2017 (as Orphan Medicine Designation by EMA), 2021 (USFDA)	GM; CAR/BCMA (receptor/ target)
Ciltacabtagene autoleucel / Carvykti™ (Janssen)	Autologous	[adult patients] r/r multiple myeloma after four or more prior lines of therapy	2020 (as Orphan Medicine Designation by EMA), 2022 (USFDA)	GM; CAR/BCMA (receptor/ target)
N/A / ImmunCell-LC® (Green Cross Cell)	Autologous	Hepatocellular carcinoma, brain tumors, and pancreatic cancer	2007 (KFDA), 2018 (Orphan Drug Designation by USFDA), India	NGM; TAA (target)
Stem Cell - Hematopoietic Stem Cells				
HPC, Cord Blood / Allocord (SSM Cardinal Glennon	Allogeneic	Disorders affecting the hematopoietic system that are inherited, acquired, or result from myeloablative treatment	2011 (USFDA)	NGM

Children's Medical Center)				
HPC, Cord Blood / Clevecord™ (Cleveland Cord Blood Center)	Allogeneic	Disorders affecting the hematopoietic system that are inherited, acquired, or result from myeloablative treatment	2016 (USFDA)	NGM
HPC, Cord Blood / Ducord™ (Duke University School of Medicine)	Allogeneic	Disorders affecting the hematopoietic system that are inherited, acquired, or result from myeloablative treatment	2012 (USFDA)	NGM
HPC, Cord Blood / Hemacord™ (New York Blood Center)	Allogeneic	Disorders affecting the hematopoietic system that are inherited, acquired, or result from myeloablative treatment	2011 (USFDA)	NGM
HPC, Cord Blood / N/A (Clinimmune Labs, University of Colorado Cord Blood Bank)	Allogeneic	Disorders affecting the hematopoietic system that are inherited, acquired, or result from myeloablative treatment	2012 (USFDA)	NGM
HPC, Cord Blood / N/A (MD Anderson Cord Blood Bank)	Allogeneic	Disorders affecting the hematopoietic system that are inherited, acquired, or result from myeloablative treatment	2018 (USFDA)	NGM
HPC, Cord Blood / N/A (LifeSouth Community Blood Centers)	Allogeneic	Disorders affecting the hematopoietic system that are inherited, acquired, or result from myeloablative treatment	2013 (USFDA)	NGM
HPC, Cord Blood / N/A (Bloodworks)	Allogeneic	Disorders affecting the hematopoietic system that are inherited, acquired, or result from myeloablative treatment	2016 (USFDA)	NGM
Betibeglogene autotemcel / Zynteglo™ (bluebird bio)	Autologous	Transfusion-dependent thalassemia	2019 (EMA) 2022 (USFDA)	GM
Elivaldogene autotemcel / Skysona (bluebird bio)	Autologous	Active cerebral adrenoleukodystrophy	2022 (USFDA)	GM
N/A / Strimvelis® (GlaxoSmithKline)	Autologous	Adenosine deaminase-severe combined immunodeficiency (ADA-SCID)	2016 (EMA)	GM
Stem Cell - Mesenchymal Stem Cells				
N/A / Cellgram™ (Pharmicell)	Autologous	Acute myocardial infarction	2011 (KFDA)	NGM; BM-MSC (cell subtype)
N/A / Cartistem® (Medipost)	Allogeneic	Repetitive and/or traumatic cartilage degeneration, including degenerative osteoarthritis without age limit	2012 (KFDA)	NGM

N/A / Queencell® (Anterogen)	Autologous	Subcutaneous tissue defects	2010 (KFDA)	NGM; Adipose-derived MSC (cell subtype)
Darvadstrocel / Alofisel® (TiGenix NV/ Takeda)	Allogeneic	Complex perianal fistulas in Crohn's disease	2018 (EMA)	NGM; Adipose-derived MSC (cell subtype)
N/A / Cupistem® (Anterogen)	Autologous	Crohn's fistula	2012 (KFDA)	NGM; Adipose-derived MSC (cell subtype)
Remestemcel-L / Prochymal® (Osiris Therapeutics/ Mesoblast Limited)	Allogeneic	Steroid-refractory acute GvHD (pediatric)	2012 (Health Canada) 2012 (New Zealand)	NGM; BM-MSC (cell subtype)
N/A / TEMCELL® HS Inj. (JCR Pharmaceutics)	Allogeneic	Acute GvHD following hematopoietic stem cell transplant	2015 (Japan)	NGM; BM-MSC (cell subtype)
Lenzumestrocel / NeuroNata-R® (Corestem)	Autologous	Amyotrophic lateral sclerosis	2014 (KFDA)	NGM
N/A / Stemirac (Unique Access Medical)	Autologous	Spinal cord injury	2018 (JMHW, conditional approval)	NGM
N/A / Stempeucel® (Stempeutics)	Allogeneic	Critical limb ischemia due to Buerger's disease	2017 (DCGI, limited marketing approval)	NGM
Stem Cell - Limbal Stem Cell				
N/A / Holoclar® (Chiesi)	Autologous	Limbal stem cell deficiency	2015 (European Commission)	NGM
Dendritic Cell				
Sipuleucel-T / Provenge® (Dendreon Corporation)	Autologous	Asymptomatic or minimally symptomatic metastatic castrate-resistant (hormone-refractory) prostate cancer	2010 (USFDA), 2013 (EMA)	NGM
N/A / CreaVax-RCC® (JW CreaGene)	Autologous	Metastatic renal cell carcinoma (post-nephrectomy)	2007 (KFDA)	NGM
N/A / APCeden® (APAC Biotech)	Autologous	Prostate cancer, ovarian cancer, colorectal cancer, non-small cell lung carcinoma	2017 (CDSCO)	NGM

Abbreviations:
Indications*:* Graft versus host disease (GvHD)
Agencies*:* The United States Food and Drug Administration (USFDA); European Medicines Agency (EMA); Korea Food and Drug Administration (KFDA); Drug Controller General of India (DCGI); CDSCO (Central Drugs Standard Control Organization, aka Indian FDA), Japanese Ministry of Health and Welfare (JMHW)
Notes*:* Genetically modified (GM), non-genetically modified (NGM), bone marrow (BM), chimeric antigen receptor (CAR), tumor-associated antigen (TAA); B-cell maturation antigen (BCMA)

Table 2.2: Clinically approved cell therapies being investigated for additional indications in the clinical trials as of 2020.

Name / Trade Name (Manufacturer)	Investigated Indications	ClinicalTrials.gov *Identifier Trial Status*
T Cell		
Tisagenlecleucel / Kymriah® (Novartis)	Various liquid cancers: primary CNS lymphoma, r/r primary CNS lymphoma, follicular lymphoma, recurrent mantle cell lymphoma, acute biphenotypic leukemia, minimal residual disease, small lymphocytic lymphoma, stage III & IV chronic lymphocytic leukemia	20 studies: 4 Not yet recruiting; 11 Recruiting; 5 Active
Axicabtagene ciloleucel / Yescarta® (Kite)	Various liquid cancers: follicular lymphoma, marginal zone lymphoma, indolent non-Hodgkin lymphoma, primary mediastinal (thymic) large B-Cell lymphoma, transformed follicular lymphoma to Diffuse large B-cell lymphoma, mantle cell lymphoma	12 studies: 2 Not yet recruiting; 4 Recruiting; 6 Active
Brexucabtagene autoleucel / Tecartus™ (Kite)	Various liquid cancers: r/r chronic lymphocytic leukemia, r/r small lymphocytic lymphoma, r/r mantle cell lymphoma, r/r non-Hodgkin lymphoma	4 studies: 2 Recruiting; 2 Active
N/A / ImmunCell-LC® (Green Cross Cell)	Hepatocellular carcinoma	2 Recruiting
Stem Cell - HSC		
HPC, Cord Blood / Hemacord™ (New York Blood Center)	Acute ischemic stroke	1 not yet recruiting
Betibeglogene autotemcel / Zynteglo™ (bluebird bio)	Beta thalassemia major, sickle cell disease	4 studies 2 Recruiting; 2 Active
Stem Cell - MSC		
N/A / Cellgram™ (Pharmicell)	Acute myocardial infarction, alcoholic liver cirrhosis, spinal cord Injury, erectile dysfunction	4 Recruiting
Darvadstrocel / Alofisel® (TiGenix NV/ Takeda)	Complex perianal fistulas in Crohn's disease	3 studies: 2 Recruiting; 1 Active
Remestemcel-L / Prochymal® (Osiris Therapeutics/ Mesoblast Limited)	ARDS, COVID-19, ulcerative colitis	3 Recruiting
N/A / Cartistem® (Medipost)	Chondral or osteochondral lesion of talus	1 Enrolling by invitation
Stem cell - Other		
N/A / Holoclar® (Chiesi)	Limbal stem cell deficiency	1 Active
Dendritic Cell		
Sipuleucel-T / Provenge® (Dendreon)	Prostate cancer	5 Active

Abbreviations: Acute respiratory distress syndrome (ARDS), coronavirus disease 2019 (COVID-19)

2.2 Cell Therapies in the Clinical Trials

Although stem cells and tissue-specific cells account for the vast majority of approved cell therapies in the current market, blood cells have emerged as the dominant cell type that is being developed and evaluated in clinical trials. Just a few years ago, the number of trials for MSCs alone was greater than the number of trials for all lymphocytes and DCs combined (*9*). Currently, T cell trials individually outnumber ***all*** stem cell trials, and far exceed those for tissue-specific cells. This ongoing shift is driven primarily by the recent clinical success of CAR-T therapy, which is in turn a product of major breakthroughs in our understanding of how immune modulatory approaches can be used to treat disease (*66-69*). In light of this trend, clinical trials were collected for analysis in this section if they use blood cells, with additional focus on stem cells delivered as single-cell suspensions, and microbes (including non-single-cell suspension dosage forms). Specifically, the trials were identified on clinicaltrials.gov by searching for each cell type with the following key words (listed in parentheses) in the "Intervention/treatment" category: T cells ('T cell'), stem cells ('stem cell'), natural killer cells ('natural killer', 'NK'), monocytes ('monocyte'), macrophages ('macrophage'), bone marrow-derived mononuclear cells ('bone marrow-derived mononuclear cell'), peripheral blood mononuclear cells ('peripheral blood mononuclear cell'), red blood cells ('red blood cell'), platelets ('platelet'), and microbes ('live biotherapeutic', 'bacteria', 'consortia'). The collected data capture the clinical landscape as of August 2020. In the "Status" category under "Recruitment," trials with a status of not yet recruiting, recruiting, enrolling by invitation, or active/not recruiting were selected. Next, the trials that mentioned the cell types of interest but did not use them as therapeutic interventions were manually filtered. Finally, long-term follow-up studies that did not involve re-administration of the therapy were also excluded. A total of 1705 unique, active cell therapy clinical trials have been identified for therapeutic purposes **(Figure 2.1)**.

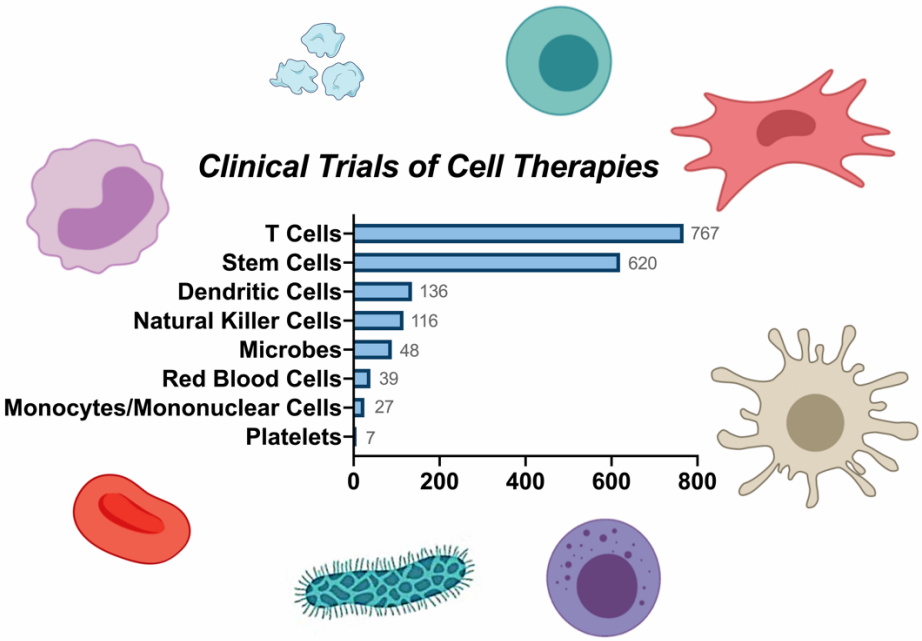

Figure 2.1: Various types of cell therapies in clinical trials. T cells dominate the current clinical studies of cell therapies, followed by stem cells, dendritic cells, natural killer cells, microbes, red blood cells, mononuclear cells, and platelets.

The clinical trials have been categorized according to cell type, general indication, trial phase, and cell source **(Figure 2.2)**. Amongst only leukocytes, T cells account for the largest portion

of all current trials (767/1705, 45%), followed by DCs (136/1705, 8%), NK cells (116/1705, 7%), and the remaining mononuclear cells (27/1705, 2%). It is unsurprising that the main indication of T cells, DCs, and NK cells is cancer (85% in T cells; 93% in DCs; 95% in NK cells), as they play major roles in anti-cancer immunity. T cells are adaptive immune cells capable of directly eliminating mutated or infected host cells, activating other immune cells, and producing cytokines to regulate immune responses (*70*). NK cells are innate immune cells that destroy tumor cells and virally infected cells via release of lytic molecules from granules and rapid production of pro-inflammatory cytokines (*71*). DCs are professional antigen-presenting cells (APC) that regulate adaptive immune cells by delivering antigens to draining lymph nodes and presenting them to cytotoxic and helper T cells (*72*). In the case of cancer treatment, T and NK cells are employed as cytotoxic agents, while DCs primarily serve as cancer vaccines. From the perspective of cell source, autologous cells are mainly used in T cell (74%) and DC (87%) therapy, as allogeneic cells increase the risk of allograft rejection (recipient cells against donor cells) or, more considerably, GvHD (donor cells against recipient cells) (*73*).

While the aforementioned leukocytes are mainly indicated for the treatment of cancer, the remaining mononuclear cells are used mostly for cardiovascular diseases (39%) and cancer (29%). Mononuclear cells here refer to one of the following cell populations: monocytes, macrophages, bone marrow-derived mononuclear cells (BMMCs), or peripheral blood mononuclear cells (PBMCs). Monocytes are circulatory cells of the innate immune system that extravasate into tissue in response to inflammation, infection, or injury (*74*). Once in the tissue, they terminally differentiate into macrophages, which are tissue-resident innate immune cells that *i*) phagocytose dead cells, debris, and foreign materials/pathogens, *ii*) modulate innate immune responses, and *iii*) maintain homeostatic growth, repair, and metabolism (*75*). BMMCs are a heterogeneous group of cells composed of lymphoid cells, myeloid cells, HSCs, and MSCs. They have major clinical applications in cardiovascular tissue regeneration due to their ability to differentiate into various lineages (*76*). Similar to BMMCs, PBMCs also contain a variety of cells including lymphocytes, monocytes, and a small percentage of DCs, and are mainly indicated for cancers. Currently, there are no Phase 4 trials employing mononuclear cells, with similar representations across Phases 1, 2, and 3. In addition, autologous mononuclear cells are employed almost exclusively (89%), likely to reduce the risk of graft rejection and GvHD.

The remaining blood cells, RBCs and platelets, are used as cell therapies for treatment of blood disorders and in trauma care via blood transfusions and account for 2% (39/1705) and <0.4% (7/1705) of all current cell therapy trials, respectively **(Figure 2.2)**. Typically, they are used to replenish lost or dysfunctional cells to maintain homeostasis in the body. The RBC is a critical transporter of oxygen and nutrients to tissues as well as an inter-organ communicator, with additional roles in the regulation of pH, redox homeostasis, and molecular metabolism (*77*). Hence, loss of RBC integrity and/or number can lead to severe pathologies and heighten the incidence of vascular disease. Similarly, platelets serve as a key element in blood vessels by regulating hemostasis under normal conditions and thrombosis upon vascular damage (*78*). Thrombocytopenia (i.e., platelet deficiency) that results from either trauma or blood disorders can lead to hemorrhage in tissues or uncontrolled bleeding of wounds. Both RBC and platelet therapy largely apply allogeneic cells (77% and 86%, respectively) in clinical settings. Still, the use of allogeneic RBCs requires blood type matching between donor and recipient. The major efforts in current RBC and platelet clinical trials are focused on optimizing transfusion protocols and verifying the durability of transfused cells.

Other than blood cells, stem cells account for 36% of current cell therapy trials (620/1705) as the second largest cell category of focus. The trials of stem-cell therapy, primarily those of HSCs and MSCs, encompass a wide range of indications covering 10 broad disease classifications **(Figure 2.2)**. HSCs are multipotent stem cells capable of self-renewing and differentiating into mature blood cells that form the myeloid and lymphoid cell lineages. As a result, hematopoietic stem cell transplant (HSCT) can be used to reconstitute the hematopoietic and immunologic systems for the treatment of inherited and acquired blood disorders. HSCT is also used frequently to treat blood cancers after cancerous cells are eliminated by a myeloablative treatment (*79*). While autologous HSCs or matched sibling donor HSCs are the most ideal candidates for HSCT due to the reduced risk of GvHD, graft rejection, and engraftment syndrome (*80*), allogeneic HSCs have an advantage in cancer treatment because they can elicit graft-versus-tumor effects (*81*). MSCs, also a type of multipotent stem cell, are capable of effectively differentiating into a wide variety of cell types in mesodermal (e.g., chondrocytes), ectodermal (e.g., neurocytes), and endodermal lineages (e.g., hepatocytes) (*82*). As a result, they have broad applications in clinical settings for the treatment of degenerative diseases, autoimmune diseases, inflammatory diseases, and trauma, among others. Notably, most stem-cell therapy trials are in early stages with nearly equal representation in Phase 1 (44%) and Phase 2 (47%), showing their considerable potential to affect the future scope of cell therapies. Finally, microbes comprise 3% of the total trials (48/1705) with major indications including cancer (44%), infectious diseases (19%), and inflammatory diseases (13%). Although metabolic disorders account for only 8% of the indications for microbes, it is worth mentioning this unique niche, as very few cell therapies are investigated for this indication. Microbes exert therapeutic mechanisms of action by *i)* displacing pathogenic microbiomes to restore symbiosis and *ii)* producing therapeutic biomolecules, a function enabled by genetic modification (*83*).

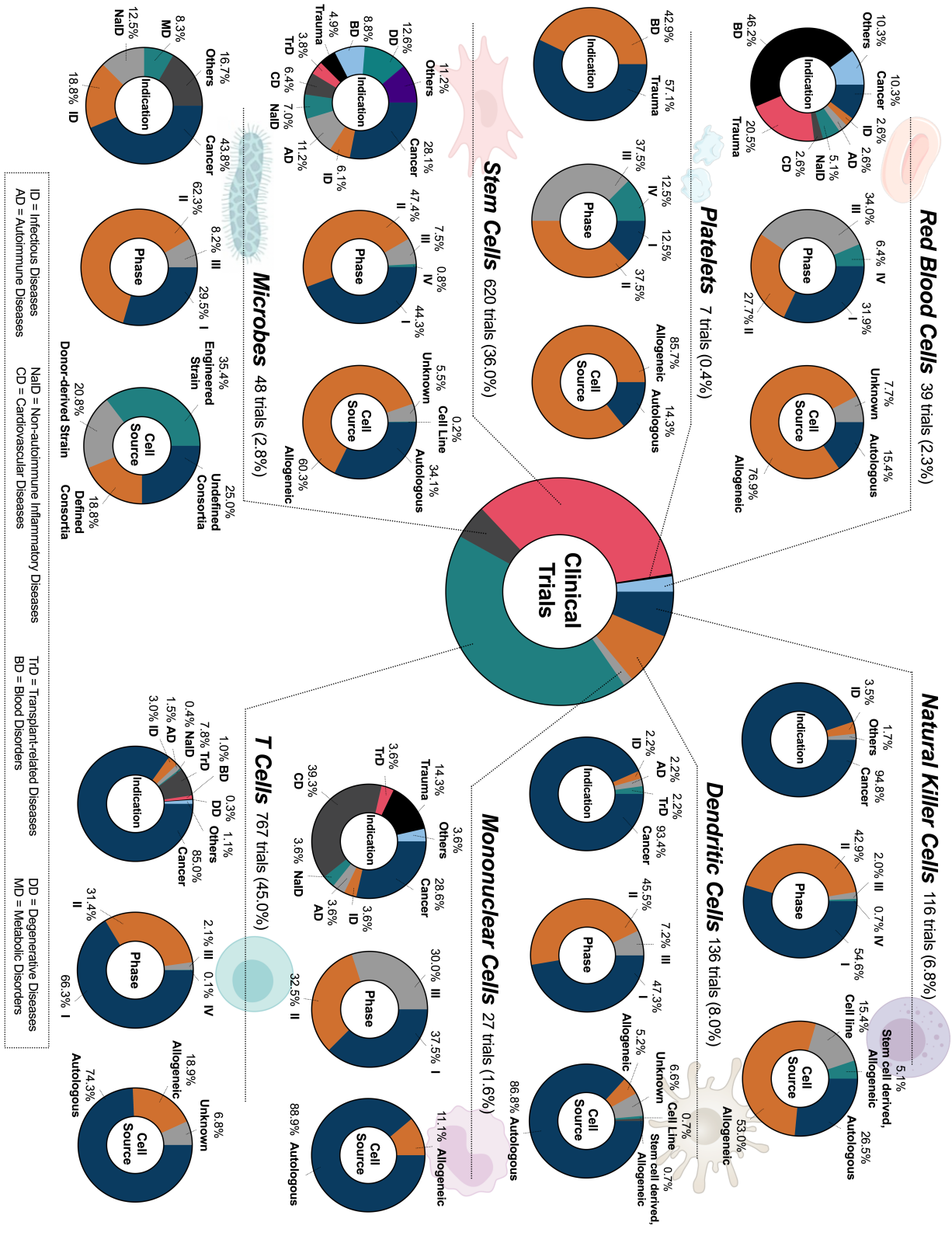

Figure 2.2: Current landscape of cell therapies in clinical trials. All clinical trials that include blood cells and stem cells delivered as a suspension, and microbes (delivered via various routes and dosage forms) were catalogued. The relevant cell types include T cells, NK cells, mononuclear cells, DCs, RBCs, platelets, stem cells, and microbes. Tissue-specific cells were excluded from the analysis. The total number of trials identified for each cell type is displayed in the figure, however the sum of these trials for all cell types (1760) exceeds the

total number of analyzed trials (1705) because some trials use two or more cell therapies in combination. For phase classification, dual-phase trials (e.g., Phase 1/2) were counted as both Phase 1 and 2. Eleven broad indications were identified for the purpose of trial classification (i.e., cancer, infectious diseases, autoimmune diseases, non-autoimmune inflammatory diseases, cardiovascular diseases, transplant-related diseases, trauma, blood disorders, degenerative diseases, metabolic disorders, others), with relevant abbreviations listed in the box on the bottom. Because some trials are used to treat more than one of these conditions, the total number of indications used to generate each pie chart exceeds the total number of trials for that cell type.

2.3 Conclusion

The proven clinical success and ongoing clinical advances of cell therapies foresees their promising future and expanding market on a global scale. Based on our analysis, about 95% of analyzed trials employed immune cells, with 'cancer' as the major indication. The prosperity of leukocyte-based cancer therapies has fueled efforts exploring immune cell engineering. While the most frequently used strategies to engineer immune cells in the clinics are *i*) ex vivo manipulation by soluble factors (*84, 85*), in vivo condition by co-administrating a bolus of supporting adjuvant drugs with cells (*18, 19*), and *iii*) genetic engineering (*20, 21*), biomaterials emerges as the fourth pillar for cell engineering (*86*). Biomaterial-assisted cellular platform serves as a more adaptable system for specific indications and broadens the applications of cell-based technologies (*28, 87*). I have collaborated with Dr. Wyatt Shields to review the biomaterials at nano-, micro-, and macro-scales for immune cell modulation or immunotherapies **(Figure 2.3)**, where we discussed materials that have been used in preclinical studies and poised for clinical translation to enhance the specificity and durability of immune cells for a range of indications (*88*).

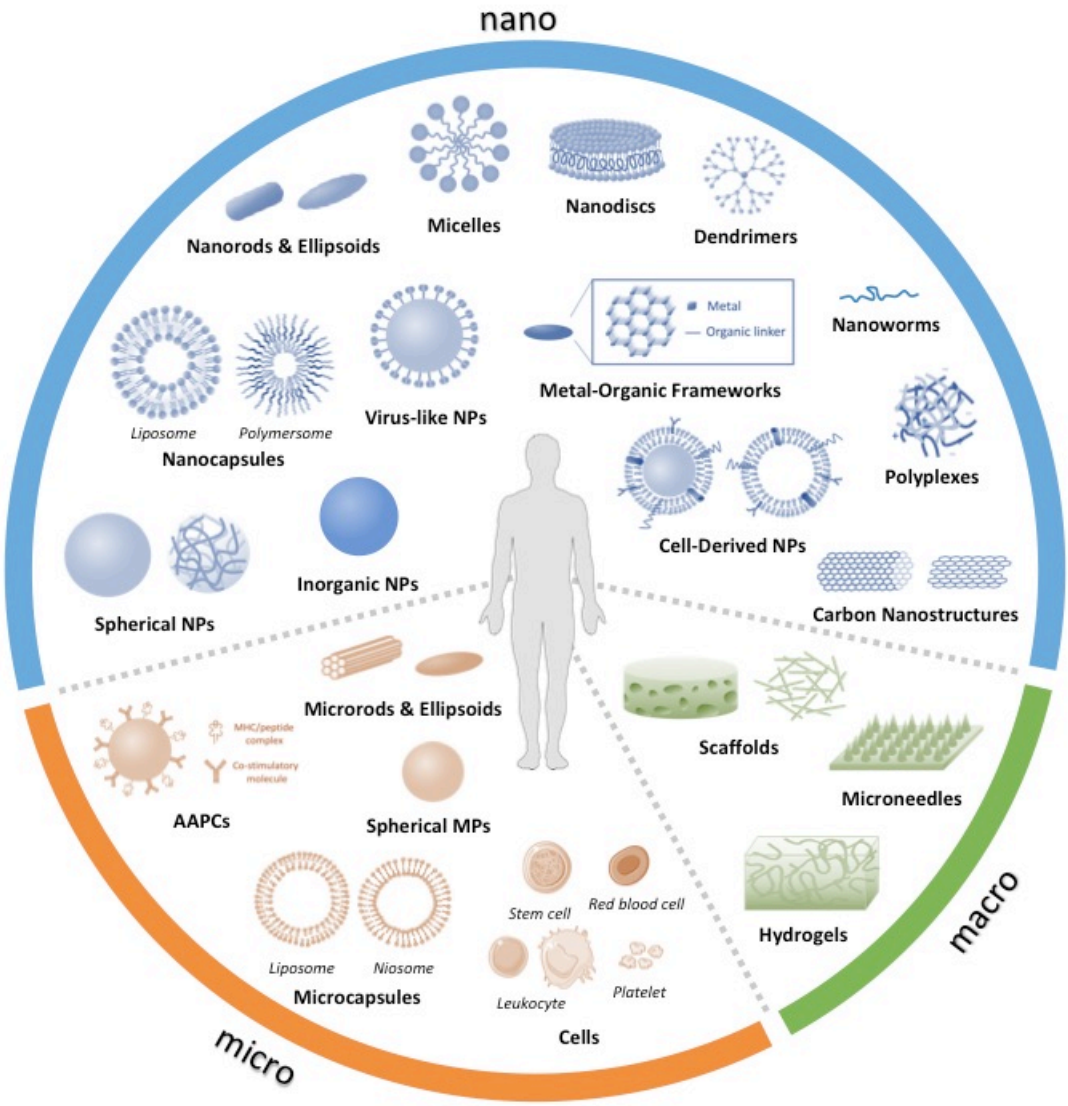

Figure 2.3: Materials for immunotherapy. Overview of material-based strategies to amplify or rewire immunotherapies, organized by their characteristic length scales (*88*).

Chapter 3: Modulate Macrophage Phenotype via Cytokine-loaded Micro-disks for Cancer Immunotherapy

In this work, collaborating with Dr. Wyatt Shields, I have contributed to discoidal particle fabrication, particle characterization (i.e., cytokine release test and adhesion studies), and macrophage culture (bone marrow extraction and macrophage differentiation). I also designed the multicolor flow cytometry panel and cooperatively performed the study to examine the macrophage phenotype in vitro. Further, I participated in designing and conducting the animal studies to determine the macrophage phenotype persistence in vivo and the therapeutic efficacy of our biomaterial-aided cell therapy.

3.1 Introduction

3.1.1 Adoptive cell therapy: grant challenges and potentials

Adoptive cell therapy has revolutionized clinical approaches to treat cancer (*89*). The most prominent example to date is CAR-T cell therapy, which consists of engineered T cells that express chimeric antigen receptors. CAR-T cell therapies are on the cusp of a clinical revolution (*90*), leading to a full recovery in over 90% of patients with some blood borne cancers (*91*). Nevertheless, the success of CAR-T cell therapy generally depends on (i) a prior knowledge and presence of tumor-specific antigens, (ii) tumors that are not solid (i.e., liquid cancers) and (iii) several weeks to prepare and expand cell populations (*92*). In contrast, macrophages are able to kill tumor cells where tumor-specific antigens are spare or unknown in a more immediate fashion, giving them the potential to succeed where T cell therapies have fallen short (*93*). However, a major hurdle that has slowed the adoption of macrophages in cancer immunotherapy is their tendency to shift to pro-tumoral phenotypes once injected into the body.

3.1.2 Plasticity of macrophage phenotype

Macrophages are perhaps the most plastic cell type in the hematopoietic system. This plasticity allows them to assume many roles like defending against foreign pathogens, aiding in wound healing and regulating tissue homeostasis (*94*). Furthermore, the phenotypic plasticity of macrophages makes them excellent candidates for addressing a range of diseases (*93*). Macrophages rely on soluble cues from the tissue microenvironment to guide their polarization into the appropriate phenotype. Polarization is best described as a multidimensional spectrum (*95*), which ostensibly can be simplified into classically activated (M1) and alternatively activated (M2) phenotypes. M1 macrophages produce nitric oxide (NO), reactive oxygen species (ROS), tumor necrosis factor alpha (TNFα), interleukin-12 (IL-12) and other cytokines that generate an inflammatory response (*96*). M2 macrophages, on the other hand, are associated with a broad range of phenotypes typically associated with wound healing and tissue regeneration. However, when tissues become dysfunctional, macrophages can develop phenotypes that promote disease pathogenesis (*97*). In the case of cancer, tumor-associated macrophages (TAMs) typically adopt an M2 (tumor-promoting) phenotype due to the immunosuppresive microenvironment of solid tumors (*98*), which is associated with tumor growth, agiogenesis, chemotherapy resistance and metastasis (*99*). To address these challenges, several clinical trials emerged in the 1990s to adoptively transfer macrophages polarized *ex vivo* with pro-inflammatory cytokines (*93*). These strategies ultimately failed, as macrophages eventually reverted to M2-phenotypes once embedded in the tumor microenvironment (**Figure 3.1A**). Thus, for macrophage-based therapies to induce robust therapeutic effects in the clinic, strategies must be developed to control phenotypes of adoptively transferred macrophages *in vivo*.

3.1.3 Our approach

We report a class of soft discoidal particles called “backpacks” capable of regulating the phenotype of macrophages *in vivo* (**Figure 3.1B**). This work builds upon the discovery that target geometry plays a deterministic role in the phagocytic fate of particles, and that anisotropically-shaped particles can evade phagocytosis for prolonged durations (*100*). Since phagocytosis occurs in an actin-dependent manner, the authors of this work postulated that particle shape determines the complexity of the actin filaments required to facilitate

internalization, and that anisotropic shapes frustrate the formation of filaments necessary to induce phagocytosis. Phagocytosis-resistant backpacks have formed the basis of several innovative demonstrations of drug delivery in the last several years (*27, 101-107*). However, these cell-based therapies are designed to transport payloads to target sites, whereby the payloads do not interact with the carrier cell (*108*). Here, we report a class of backpacks that guide the phenotype of cells to which they are bound, in this case toward pro-inflammatory phenotypes, and maintain those phenotypes deep in the immunosuppressive neoplasm of solid tumors, and that the backpacks can potentiate an antitumor response.

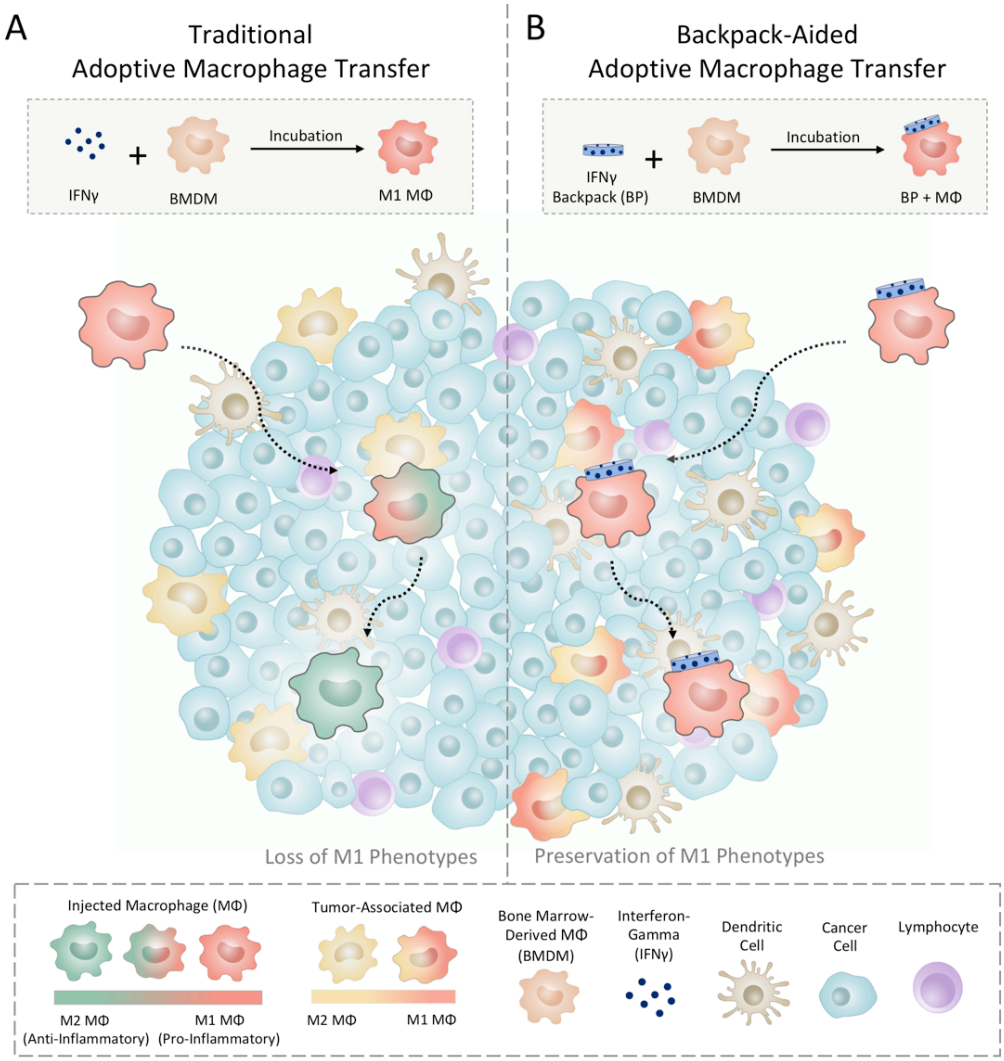

Figure 3.1: Schematic illustration of cellular backpacks for maintaining pro-inflammatory phenotypes of adoptive macrophage (MΦ) therapies. (A) MΦs polarized with IFNγ *ex vivo* quickly shift from pro-inflammatory to anti-inflammatory phenotypes after penetrating a solid tumor. (B) MΦs carrying IFNγ-loaded backpacks maintain their pro-inflammatory phenotypes deep within the tumor microenvironment, altering the phenotypes of endogenous TAMs (*32*).

3.2 Materials and Methods

Materials. 4T1 mammary carcinoma cells and 4T1-Fluc-Neo/eGFP-Puro cells expressing firefly luciferase were obtained from ATCC and Imanis Life Sciences, respectively. RPMI-1640 media, Dulbecco's modified eagle medium (DMEM) F12 media, fetal bovine serum (FBS), penicillin and streptomycin (Pen Strep), mouse IFNγ recombinant protein, Gibco™ Type 1 Collagenase, SYTOX™ blue dead cell stain, NucBlue stain, coumarin 6 membrane dye, heparin-coated plasma preparation tubes, and UltraComp eBeads™ compensation beads were obtained from Thermo Fisher Scientific. Materials for backpack fabrication, including polydimethylsiloxane (PDMS), poly(allylamine) hydrochloride (PAH), hyaluronic acid (HA), poly(vinyl alcohol) (PVA), poly(lactic-co-glycolic) acid (PLGA), and trichloro(1H,1H,2H,2H-perfluorooctyl)silane (FDTS) were obtained from Millipore Sigma. Red blood cell (RBC) lysing buffer Hybri-Max, Trypan Blue, DNAse I, trypsin, and all solvents used were obtained from Millipore Sigma. Cell culture flasks, plates, and conical tubes were obtained from Corning. Mouse Th1/Th2/Th17 cytokine quantification kits, cell fixation/permeabilization kits, and cell strainers (40 and 70 μm) were obtained from BD Biosciences. A QuadroMACS separator, a $CD45^+$ leukocyte isolation kit and a mouse tumor dissociation kit were obtained from Miltenyi Biotec. Bambanker cell freezing media and OCT compound were obtained from VWR International. Recombinant murine macrophage colony stimulating factor (M-CSF) was obtained from PeproTech. Murine IFNγ ELISA kits were obtained from R&D Systems. Female BALB/c mice (6–8 weeks old) were obtained from Charles River. Information about the antibodies and their related clones and fluorophores are detailed in Table 3.1.

Table 3.1 Antibodies used for flow cytometry.

Antibody Target	Fluorophore	Host/Isotype	Clone	Supplier
Ly-6G	PE-Cy7	Rat / IgG2b, kappa	RB6-8C5	Thermo Fisher Scientific
CD11c	PE	Armenian hamster / IgG	N418	
CD11b	FITC	Rat / IgG2b, kappa	M1/70	
CD206	PE-Cy7	Rat / IgG2b, kappa	MR6F3	
CD309 (VEGF)	APC	Rat / IgG2a, kappa	Avas12a1	
CD80	PE	Armenian hamster / IgG	16-10A1	
MHCII	FITC	Rat / IgG2b, kappa	M5/114.15.2	
iNOS	PE-Cy7	Rat / IgG2a, kappa	CXNFT	
iNOS	APC	Rat / IgG2a, kappa	CXNFT	
Isotype Control	PerCP-Cy5.5	Armenian hamster / IgG	eBio299Arm	
Isotype Control	PE-Cy7	Rat / IgG2a, kappa	eBR2a	
Isotype Control	PE	Rat / IgG2a, kappa	eBR2a	
Isotype Control	FITC	Rat / IgM, kappa	eBRM	
Isotype Control	PerCP-Cy5.5	Rat / IgG2a, kappa	eBR2a	
Isotype Control	PE-Cy7	Rat / IgG2b, kappa	eB149/10H5	
Isotype Control	PE	Armenian hamster / IgG	eBio299Arm	
Isotype Control	FITC	Rat / IgG2b, kappa	eB149/10H5	
Sheep IgG	FITC	Sheep / IgG	Polyclonal	Novus
HIF-1α	PE	Rat / IgG1	241812	
Arg-1	FITC	Sheep / IgG	Polyclonal	Fisher Scientific
F4/80	PerCP-Cy5.5	Rat / IgG2a, kappa	BM8.1	Millipore Sigma

Mold fabrication. Silicon molds were fabricated using standard monolithic photolithography via methods similar to those described previously (*109*). Briefly, hexamethyldisilazane adhesion promoter was spin-coated on 3" single-side polished silicon wafers (Addison Engineering, Inc.). SPR 220-7.0 (MicroChem Corp.) was spin-coated on each wafer at 4,000 rpm for 45 sec. Wafers underwent a soft bake at 115°C for 90 sec, and were exposed to UV light (405 nm, MA/BA6 Mask Aligner, Süss MicroTec AG) through a chrome-patterned photomask consisting of an array of 8 μm transparent circles with a 16 μm pitch (Photo Sciences, Inc.). Wafers underwent a post-exposure bake at 115°C for 90 sec and were submerged in MF-CD26 for 120 sec. Wafers were cleaned by rinsing with water and drying with a stream of nitrogen gas. Prior to use, molds were passivated with a thin film of trichloro(1H,1H,2H,2H-perfluorooctyl)silane (FDTS) by vapor deposition.

PDMS template preparation. PDMS templates were prepared by soft lithography using methods similar to those described previously (*109*). A 10:1 weight ratio of PDMS base to crosslinker from a Sylgard 184 kit was thoroughly mixed and poured on top of the silicon molds in separate Petri dishes (~20 g per mold). PDMS was degassed in a desiccator at 25°C until no visible bubbles remained. Dishes were then placed into an oven at 65°C overnight to cure the PDMS. After curing, PDMS templates were removed from the molds by cutting the Petri dishes and peeling away the PDMS.

Cell-adhesive coating. HA (2,500 kDa) was modified with aldehyde (HA-Ald) via methods described previously (*110*). A 2 mg/mL aqueous solution of HA-Ald was prepared in 150 mM NaCl (pH = 6.8), and a 2 mg/mL aqueous solution of PAH (17.5 kDa) in 150 mM NaCl (pH = 6.8) was prepared. HA-Ald, PAH, and 150 mM NaCl (pH = 6.8) solutions were separately poured into weigh boats. PDMS templates were rinsed with isopropyl alcohol and dried by a steady stream of air. Templates were then placed patterned side down in the HA-Ald solution for 15 min. Care was taken to ensure the templates were floating to maximize contact of the patterned PDMS with the solution. Templates were transferred to the NaCl solution for 2 min and were then rinsed with DI water to remove free HA-Ald. Templates were transferred to the PAH solution for 15 min in the same fashion, then transferred to new weigh boats with the NaCl solution for 2 min. Templates were rinsed with DI water, and the entire process was repeated once more to form a layer-by-layer (LBL) coating of HA-Ald/PAH/HA-Ald/PAH. Coated templates were rinsed with DI water for 30 sec and dried by a stream of air. Templates were stored in Petri dishes, patterned side up, at 4°C.

Backpack fabrication. An 8% w/v solution of PLGA in acetone was prepared from a 100:1 weight ratio of non-fluorescent PLGA (7–17 kDa, Resomer 502 H) and fluorescent PLGA (10–30 kDa, LG 50:50 rhodamine B; PolySciTech). PDMS templates with LBL coatings were cut into quadrants and spin-coated with 225 μL PLGA solution per quadrant at 2,000 rpm for 20 sec (at a 200 rpm/sec ramp). Quadrants were then plasma ashed with O_2 for 60 sec. A 0.5 wt.% solution of PVA (146–186 kDa, 99+% hydrolyzed) in PBS was prepared with 25 μg/mL IFNγ. Immediately after plasma treatment, 100 μL of the PVA solution was evenly spread onto each quadrant by pipette. Quadrants were then placed in a desiccator under vacuum with Drierite desiccant (W.A. Hammond Drierite Co.) until dry, making a 0.62 μm thick PVA film. A second PLGA layer was deposited using the same procedure as the first.

Microcontact printing. PVA-coated dishes were prepared by making a 3% w/v solution of PVA (13–23 kDa, 87% hydrolyzed) in DI water. The solution was stirred at 80°C for several hours, and excess crystals were filtered using a 0.22 μm filter. Sterile Petri dishes were coated with 2.5 mL of solution, placed in an oven at 60–75°C until dry. Backpacks were printed using

techniques similar to those described previously (*103*). Briefly, a beaker was filled with DI H_2O and heated to 65°C. The coated side of a PVA-coated dish was held ~2 cm over the beaker for 6–12 sec. A PDMS quadrant containing backpacks was immediately pressed onto the warmed PVA dish and consistent pressure was applied for 15–20 sec. The quadrant was then peeled away, leaving a coating of backpacks on the dish. This was repeated until the material had fully transferred. Backpacks were then stored at –80°C until needed. To harvest backpacks, dishes were covered with 2.5 mL of PBS and were gently washed. This was repeated until the surface appeared mostly clear (typically twice). The solution was collected, passed through a 40 μm cell strainer, and centrifuged at 2,500xG for 5 min. Backpacks were resuspended in 5 mL BMM- (i.e., 500 mL DMEM F12, 50 mL FBS, 5 mL Pen Strep, and 25 mL 200 mM GlutaMAX) or serum-free BMM- (i.e., BMM- sans FBS), depending on the application.

Atomic force microscopy (AFM). AFM (NanoWizard 4; JPK BioAFM GmbH) was used to characterize the stiffness and morphology of the different layers of the backpack. Layers were individually prepared on polydimethylsiloxane (PDMS) stamps and printed on glass slides treated with plasma for 60 s using the method described in the **Microcontact printing**. A 100 μm cantilever (All-In-One Al; BudgetSensors) with a stiffness of 40 N/m was used in tapping mode. To sample force curves and measure stiffness, a random number generator was used to sample 0.5 μm x 0.5 μm sections of the poly(lactic-co-glycolic acid) (PLGA) disks along their edges. A hertz-fit process was used, assuming a paraboloid tip with 10 nm radius and a Poisson's ratio of 0.265.

Cumulative IFNγ release assay. After harvesting, backpacks were centrifuged at 1,500xG for 5 min and were reconstituted in BMM- (comprising 500 mL DMEM F12, 50 mL FBS, 5 mL Pen Strep, and 25 mL 200 mM GlutaMAX). Backpacks were counted and diluted to a concentration of $2.0x10^5$ particles/mL. 1 mL sample volumes were transferred to non-stick Eppendorf tubes. For the first time point, each sample was centrifuged at 1,500xG for 5 min. Two 450 μL aliquots were transferred to separate Eppendorf tubes and were frozen at –80°C. 900 μL of fresh BMM- was added to each sample and the sample stored at 37°C until the next time point. The sampling procedure remained the same for all time points, except 925 μL of BMM- was sometimes added after sampling instead of 900 μL to account for liquid evaporation. After the last time point was collected, frozen samples were thawed, diluted 20−50x, and IFNγ concentrations were determined by an ELISA kit. The optical density at 450 nm was recorded using a plate reader (Spectramax i3), following instructions by the manufacturer for background corrections (Molecular Devices, LLC). Standard curves and cumulative IFNγ concentrations were determined in Microsoft Excel.

Bone marrow isolation. Progenitor cells were isolated from murine bone marrow following methods described previously (*111*). Briefly, 6–8 week old BALB/C mice were euthanized via CO_2 inhalation. Sterile surgical scissors were used to extract the tibias, femurs, and humeri. Isolated bones were submerged in 70% ethanol, rinsed with PBS, and then transferred to a separate PBS solution. In a sterile environment, epiphyses of each bone were cut and the bones were flushed with PBS via a syringe with a 31 G needle into a 50 mL collection tube. The solution was mixed thoroughly, passed through a 40 μm cell strainer, and centrifuged at 400xG for 10 min at 4°C. Cells were resuspended in Bambanker (2 mL per mouse equivalent; Lymphotec, Inc.) and stored in cryovials at –80°C until needed.

Bone marrow-derived macrophage (BMDM) culture. BMDMs were cultured from murine bone marrow progenitor cells following methods described previously (*98*). Briefly, frozen bone marrow was thawed and mixed with 4°C BMM- at 1:5 ratio by volume. The solution was

centrifuged, the liquid was aspirated, cells were resuspended in BMM+ (i.e., BMM- with 20 ng/mL M-CSF), and cells were counted with a hemocytometer. Approximately $4x10^6$ bone marrow cells were added to non-tissue culture (TC) treated T175 flasks containing 25 mL BMM+. Cells were incubated under standard culture conditions. 25 mL additional BMM+ was added to the flasks on Days 3 and 7. On Day 8, media was aspirated from the flasks, and cells were washed once with 10 mL PBS. To dislodge the cells, PBS was aspirated and replaced with 10 mL Accumax (Innovative Cell Technologies) at 4°C. Cells were incubated with the Accumax at 37°C for 10 min. The flask was then removed from the incubator and vigorously thumped several times. More Accumax (10 mL) was added to the flask, and cells were incubated for an additional 10 min and thumped again. The suspension of BMDMs was added to a 50 mL conical tube with an equal volume of BMM- and centrifuged. The supernatant was aspirated and replaced with BMM+. BMDMs were counted and plated on non-TC-treated 12-well plates at a concentration of $2.5x10^5$ cells/well in a volume of 1 mL/well and incubated under standard conditions for 24 h. All centrifugation steps were performed at 400xG for 10 min at 4°C.

Serial dilution. Due to extensive death of BMDMs from surface tension effects resulting from media removal in 12-well plates, which was reported in other studies (*98*), we utilized a special media exchange technique in wells or dishes with diameters smaller than 60 mm. Instead of aspirating the full liquid volume and adding fresh media, 0.5 mL media was removed from each well (leaving 0.5 mL media in each well), 5 mL of the desired media was added to each well, and then 5 mL of media was removed from each well. This process was repeated a total of two times to nearly replace the original media with the desired media. This procedure is herein referred to as serial dilution.

Hypoxia chamber. A hypoxia chamber (Stemcell Technologies) was used to culture bone marrow derived macrophages (BMDMs) under hypoxic conditions. Prior to incubation, paper towels soaked with PBS were placed along the bottom of the chamber to minimize evaporation. Plates containing BMDMs were sealed with parafilm and placed into the chamber (Parafilm limits evaporation, but allows for gas exchange). The chamber was flushed with a gas mixture containing 94% N_2, 5% CO_2 and 1% O_2 at a flow rate of 20 L/min for 10 min. The chamber was sealed and incubated at 37°C. The chamber was flushed again 2 h later and every 24 h thereafter to ensure consistent oxygen levels.

Binding backpacks to BMDMs. Backpacks were harvested and centrifuged at 2,500xG for 5 min at 4°C and resuspended in serum-free BMM-. Meanwhile, BMDMs cultured in 12-well plates for 24 h were removed from the incubator and BMM+ media was exchanged with serum-free BMM- media using a serial dilution. Backpacks were counted using a hemocytometer, and $0.375x10^5$ backpacks were added to each well of each 12-well plate (yielding a 3:2 ratio of backpacks:cells). Plates were then centrifuged at 300xG for 7.5 min to allow backpacks to gather along the bottom of the plate. Plates were then placed in a cell culture incubator for 1.5 h to allow BMDMs to bind to backpacks. After 1.5 h, serum-free BMM- media was exchanged with BMM- media via serial dilution. Plates were then incubated in either standard culturing conditions (normoxia; 74% N_2, 5% CO_2 and 21% O_2;) or hypoxic conditions (94% N_2, 5% CO_2 and 1% O_2), depending on the study. In cases where plates were stored in a hypoxia chamber, 100 µL BMM- from each well was replaced with 100 µL tumor-conditioned media (TCM), obtained from culture with 4T1 cells. In lieu of backpacks, free IFNγ was sometimes added at a concentration of 16 ng/mL to the appropriate wells.

Phenotyping *in vitro* cultures of BMDMs. Serial dilution was performed to replace media in each well of the 12-well plates with Hank's Balanced Salt Solution (HBSS). Then 500 µL HBSS was aspirated from each well and replaced with 2 mL Accumax. Plates were incubated at 37°C and 5% CO_2 for 10−15 min. Plates were then thumped to release BMDMs and the respective groups were collected into separate 50 mL tubes with an equal volume BMM-. Cells were centrifuged and pellets were resuspended in 1 mL of stain buffer, comprising 1% FBS in PBS without Mg^{2+} or Ca^{2+} (pH = 7.4−7.6). Cells were transferred into 1.5 mL Eppendorf tubes, where they were centrifuged again. Pellets were resuspended in 99 µL of stain buffer with 1 µL Fc block and were incubated for 15 min at 4°C. After incubation, samples were diluted with 1 mL stain buffer, centrifuged, and resuspended in 1 mL of stain buffer. Each sample was then split into two groups of 500 µL for surface marker staining and intracellular staining. For surface staining, samples were centrifuged and resuspended in an antibody mixture of anti-CD80, anti-MHCII, anti-VEGF, and stain buffer (at concentrations suggested by the manufacturer) in the dark at 4°C. After 30 min, cells were washed with 1 mL stain buffer, centrifuged, resuspended in 300 µL, and stored in the dark at 4°C until use. For intracellular staining, samples were fixed and permeabilized following instructions from the manufacturer (BD Biosciences). Cells were centrifuged and resuspended in 100 µL of an antibody solution comprising anti-iNOS, anti-HIF-1α, anti-CD206, and Perm/Wash™ Buffer (at concentrations suggested by the manufacturer) in the dark at 25°C. After 30 min, cells were diluted with 1 mL of Perm/Wash™ Buffer, centrifuged, resuspended in 300 µL of stain buffer, and stored in the dark at 4°C until use. All centrifugation steps were performed at 350xG for 5 min at 4°C. Compensation and voltage settings were determined one day prior using sets of compensation beads, each stained with one antibody. Up to 10,000 events were collected for each sample. Data were analyzed using FCS Express 6 Software (De Novo Software).

Tumor model establishment. Experiments involving animals were performed according to the protocols approved by the Institutional Animal Care and Use Committee of Harvard University. Two orthotopic breast cancer models were used in mice, 4T1 and 4T1-Fluc-Neo/eGFP-Puro cells expressing firefly luciferase (4T1-Luc). 4T1 cells were cultured in DMEM supplemented 10% FBS and 1% Pen Strep. 4T1-Luc cells were cultured in RPMI-1640 media supplemented with 10 % FBS, 1% Pen-Strep and 0.1 mg/mL G418. Both lines were cultured in a humidified incubator maintained at 37°C and 5% CO_2. Cells were passaged twice before inoculation. Cells were released via trypsin, centrifuged, and resuspended in physiological saline. Mice were inoculated with $1x10^5$ 4T1 cells or $1x10^6$ 4T1-Luc cells (>98% cell viability) in 50 µL by subcutaneous injection into the lower left inguinal mammary fat pad of BALB/c mice 42−56 days in age using a 25 G needle. Tumor-bearing mice were randomized before treatments and monitored for tumor growth and body weight changes throughout the study. Each mouse model received two treatments, which began 14 days post-inoculation in the 4T1 model (tumor volume ~100 mm^3) and 9 days post-inoculation in the 4T1-Luc model (tumor volume ~ 50 mm^3). Tumor volumes were calculated using the formula: $V = ½ L \times W^2$, where L and W were the longest and shortest dimensions of the tumor, respectively. Mice harboring 4T1 tumors were used for tumor-immune cell phenotyping. These mice were euthanized if L exceeded 15 mm or if body weight loss exceeded 15%. Mice in the 4T1-Luc model were enrolled in a survival study and were left alive until they succumbed to tumor burden or were euthanized with CO_2 if they became moribund.

Intratumoral injections. Mice received two intratumoral treatment injections, occurring 14 and 18 days after inoculation in the 4T1 model and 9 and 14 days after inoculation in the 4T1-Luc model. IFNγ was limited to 50 ng per administration (*112*). Mice requiring injected macrophages each received the same number of cells (i.e., $0.78x10^6$

macrophages/mouse/injection). Numbers were determined based on the number of macrophages necessary to deliver 50 ng worth of IFNγ backpacks. Determinations were based on ELISA data, which revealed ~85 fg IFNγ/backpack, and flow cytometry, which revealed ≥75% of macrophages were labeled with ≥1 backpack after the 1.5 h incubation period. In all groups (i.e., saline, free IFNγ, or groups with macrophages), injection volumes were 10 μL.

***In vivo* tracking of adoptively transferred macrophages.** Mice inoculated with 4T1 cells were treated with macrophages labeled with a near-infrared dye (VivoTrack 680, Perkin Elmer). Seven days prior to tumor inoculations through to the end of the study, mice were fed alfalfa-free diets to reduce background fluorescence levels (Picco Rodent 5V5R 50IF irradiated pelleted, Scott Pharma Solutions). Prior to imaging, hair over top and near the tumor was removed using a topical formulation (Nair, Church & Dwight). Mice were imaged under anesthesia (from isoflurane) using IVIS each day after the first therapeutic administration for a total of 5 days.

***In vivo* monitoring of lung metastases.** Lung metastases were evaluated 32 days after inoculation with 4T1-Luc. Mice were injected with 150 μL of 30 mg/mL XenoLight D-Luciferin potassium salt bioluminescence substrate (PerkinElmer) in saline via intraperitoneal injection. 15 min after injection, mice were imaged under anesthesia (from isoflurane) using IVIS. Primary tumors were covered with strips of black paper to eliminate signal washout from the main tumors, which were comparatively brighter than the metastatic colonies in the chest cavities.

Phenotyping tumor-associated immune cells. Procedures for isolating and staining tumor-associated immune cells were similar to those described previously (*113*). Briefly, mice were euthanized via CO_2 inhalation 2 days after administration of the second treatment. Primary tumors (from 4T1 cells) were harvested, cut into small pieces (<5 mm thick) and enzymatically degraded using a mouse tumor dissociation kit with a gentleMACS dissociator (Miltenyi Biotec). Cells were centrifuged and resuspended in ACK red cell lysis buffer supplemented with 50 U/mL of DNAse I for 5 min. Cells were again centrifuged and resuspended in PBS to quantify the remaining intact cells. Leucocytes were isolated from the general population using a $CD45^+$ isolation kit, following instructions from the manufacturer (Miltenyi Biotec). For the remainder of the study, $1x10^6$ cells per animal were used and all steps were performed in 100 μL FACS buffer (PBS with 3% FBS) supplemented with additional reagents as necessary. Cells were blocked for 30 min in a solution consisting of 5% rat serum, 5% mouse serum, and 1% anti-mouse CD16/32 antibody. Cells were stained with test and control antibodies (see **Figure 3.7** and **Table 3.1**) for 30 min at 25°C and for 20 min on ice in a dark enclosed space. Cells were then washed twice with ice-cold FACS buffer and resuspended in 500 μL PBS. Following instructions from the manufacturer, cells were stained with SYTOX™ blue to measure cell viability at the end of all treatment steps. Stained cells were then analyzed by flow cytometry (BD LSRII). Compensation and voltage settings were determined one day prior using sets of compensation beads, each stained with one antibody. Up to 100,000 events were collected for each sample. Data were analyzed using FCS Express 6 Software. All centrifugation steps were performed at 350xG for 5 min.

Immunohistochemical sectioning. Tumors embedded in OCT compound were cut into 5 μm thick sections using a Leica CM1950 cryostat and mounted on SuperFrost Plus microscope slides (Thermo Fisher). Once dried, slides were washed with PBS twice for 7 min. Slides were fixed with a 3.0 vol.% solution of paraformaldehyde in PBS for 15 min. Slides were washed once with PBS for 7 min. Slides were then mounted with ProLong Diamond antifade mountant

with DAPI following instructions from the manufacturer (Thermo Fisher). 24 h later, slides were sealed with nail polish and stored at −20°C until imaging. Sections were analyzed with a Zeiss Axio Scan.Z1 Slide Scanner Microscope (10x objective). Images were processed with ImageJ.

Statistical analysis. Unless otherwise indicated, the data were represented as mean ± standard error using GraphPad (Prism 8.0). For determination of statistical significance, multiple t-tests or one-way ANOVA with Tukey's multiple comparison tests were used, as applicable. Significance was determined at the following cutoff points ($p < 0.05$ = *, $p < 0.01$ = **, $p < 0.001$ = ***). Significance from the survival time was quantified using a Log-Rank test.

3.3 Results

3.3.1 Backpack fabrication and characterization

Backpacks were prepared from biodegradable polymers using microcontact printing (**Figure 3.2**) (*109, 114*). Each backpack contained a cell-adhesive layer, a poly(lactic-co-glycolic acid) (PLGA) layer, a polyvinyl alcohol (PVA) layer and a second PLGA layer (**Figure 3.3A, i and ii**). PVA was chosen as the interior layer due to its hydrophilicity, enabling facile incorporation of cytokine. We chose interferon gamma (IFNγ) due to its potency in stimulating pro-inflammatory macrophages and its robust antitumor activity (*115, 116*). PLGA was chosen to provide structural support to the PVA layer. The cell-adhesive layer was made by layer-by-layer (LBL) assembly. It comprised two sets of alternating layers of hyaluronic acid modified with aldehyde (HA-Ald) and poly(allylamine) hydrochloride (PAH) (*117*). Backpacks displayed an average stiffness of 292 ± 67 MPa, an average thickness of 1.49 ± 0.14 μm and an average width of 7.56 ± 0.37 μm, as determined by AFM (**Figure 3.3A (iii)**).

We investigated the role of PVA in the interior of the backpacks on stabilizing IFNγ. We found that increased thicknesses of PVA improved the activity of IFNγ, despite the same loading of IFNγ per backpack (**Figure 3.3B**). This is likely because the PVA stabilized the IFNγ when the second layer of PLGA dissolved in acetone was deposited. While thicker PVA layers improved the activity of IFNγ, we fixed the thickness to 0.62 μm for the remainder of the study, as higher PVA content reduced printing efficiency. Next, we investigated the release of IFNγ from the backpacks into serum media at 37°C over time (**Figure 3.3C**). We found that backpacks released IFNγ for at least 60 h.

Next, we evaluated the interaction of backpacks with primary BMDMs using two techniques. First, we examined the association of fluorescent backpacks with cells using flow cytometry, which included both surface-bound and phagocytosed backpacks (**Figure 3.3D**). We found that backpacks encapsulating IFNγ displayed a higher affinity to BMDMs than those without, which is likely due to the enhanced activity of macrophages when stimulated by IFNγ (*118*). Over 5 days, the association of IFNγ backpacks reduced from 83.6 to 75.4%, whereas the association of blank backpacks reduced from 77.5 to 61.2%. Second, we examined the resistance of IFNγ backpacks to phagocytosis compared to spheres of similar volumes using fluorescence microscopy (**Figure 3.3E**). We compared the number of surface-bound backpacks (V_{BP} = 49.8 μm^3) to the number surface-bound 3.3 μm spheres ($V_{3.3}$ = 18.8 μm^3) and 6.2 um spheres ($V_{6.2}$ = 124.8 μm^3). Over 5 days, the proportion of backpacks that remained surface-bound reduced from 89.1 to 77.3%, whereas spheres of both sizes were nearly completely internalized after 3 days (<5% remained surface-bound). Together, both sets of data suggest that the majority of cell-associated backpacks evaded phagocytosis for at least 5 days. We also

imaged cells (labeled with NucBlue, blue; coumarin 6, green) displaying backpacks made from rhodamine B PLGA discs (red) using confocal microscopy (**Figure 3.3F**).

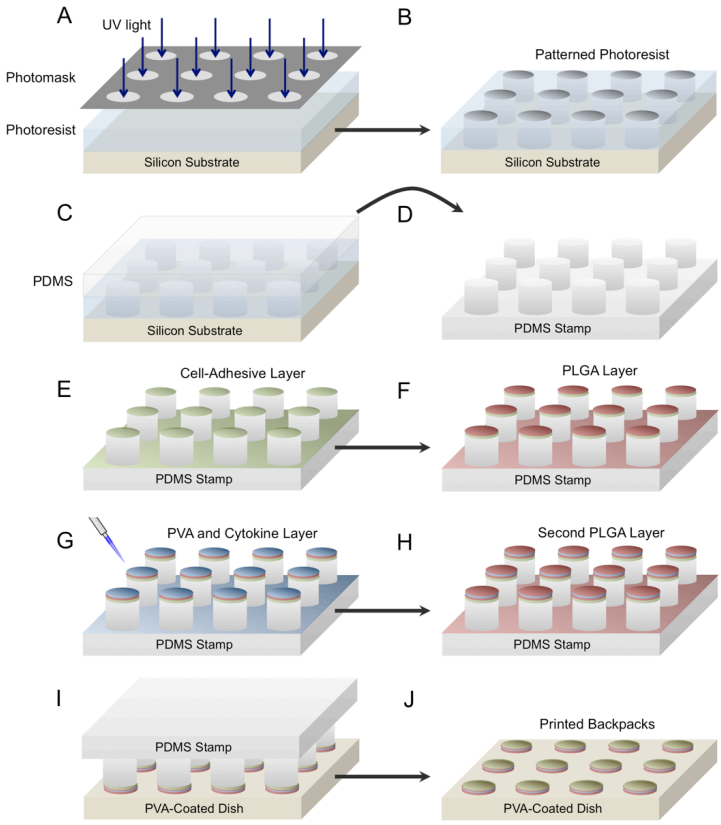

Figure 3.2: Fabrication of IFNγ backpacks. (A) Silicon molds were prepared by photolithography. (B) Molds contained an array of cylindrical holes, 8 μm across and 7 μm deep, with a pitch of 16 μm. Completed molds were treated with FDTS by vapor deposition. (C) Polydimethylsiloxane (PDMS) was poured over the molds, degassed, and cured. (D) PDMS was separated from the mold, forming a stamp. (E) PDMS stamps were coated with alternating layers of charged, cell-adhesive polymers. (F) A poly(lactic-co-glycolic acid) (PLGA) solution was spin coated over the stamps. (G) Stamps were plasma ashed, coated with an aqueous film of poly(vinyl alcohol) (PVA) containing IFNγ, and were dried by evaporation. (H) A second PLGA solution was spin coated over the stamps. (I) PVA-coated dishes were heated over a water bath. (J) PDMS stamps were pressed onto the dishes to transfer an array of the IFNγ backpacks by microcontact printing.

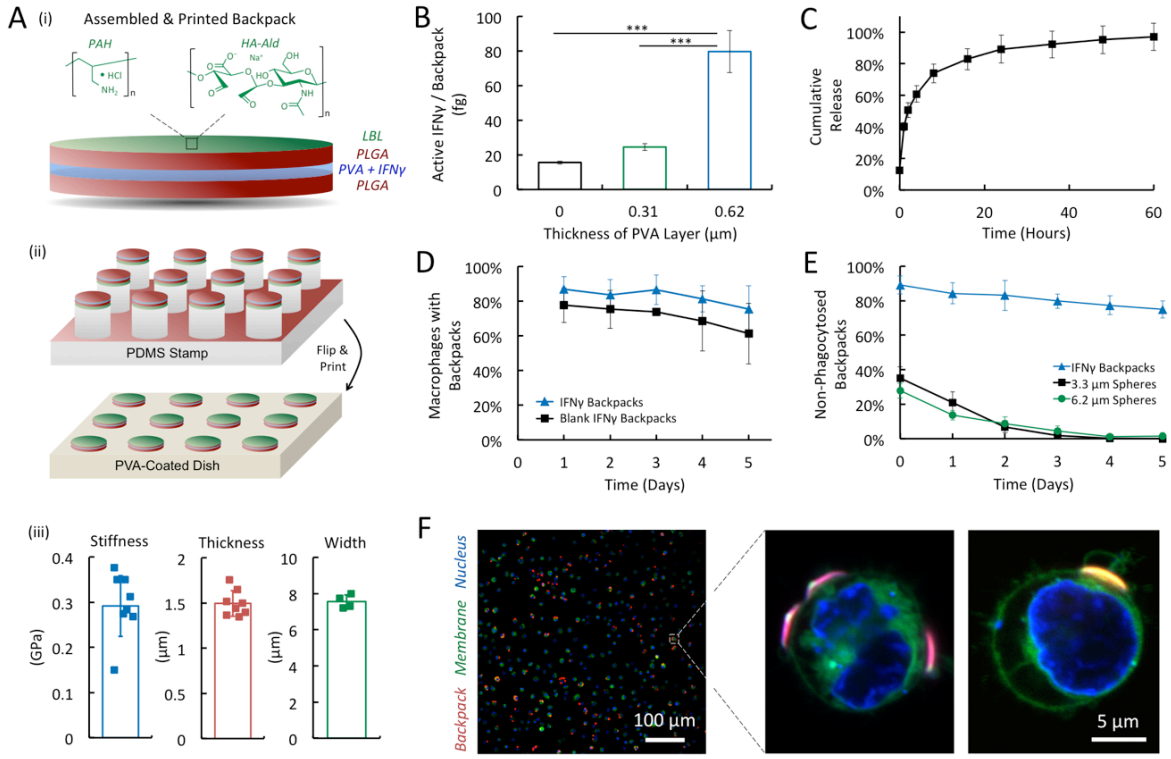

Figure 3.3: Backpack preparation and characterization. (A) Schematic illustrations of a backpack (i) and its method of printing (ii); graphs of average backpack stiffness, thickness and width (n ≥ 4) (iii). (B) Amount of active IFNγ per backpack, determined by ELISA (n = 5). (C) Cumulative release of IFNγ from backpacks over 60 h (n = 3). (D) Association of backpacks with primary murine macrophages over time *in vitro* (n = 3). (E) Proportion of backpacks that evaded phagocytosis over time compared to spheres of similar volume (n = 5). (F) Confocal micrographs of leukocytes (nucleus, blue; membrane, green) displaying PLGA discs (red).

3.3.2 IFNγ backpacks induce M1 phenotypes in vitro

To assess the potency of IFNγ backpacks to potentiate a durable shift in polarization, we evalulated the expression of several markers associated with M1 and M2 phenotypes (**Figure 3.4**). BMDMs were cultured from murine bone marrow progenitor cells and IFNγ backpacks were added to cells in a ratio of 3:2, respectively. After 1.5 hr, unbound backpacks were removed, and cells were cultured for 24–120 h. In addition to BMDMs with IFNγ backpacks in standard culture conditions, we also cultured BMDMs (i) without backpacks (no IFNγ), (ii) with blank backpacks (no IFNγ) and (iii) without backpacks yet with an equivalent dose of free IFNγ (16 ng/mL). We also cultured BMDMs with IFNγ backpacks in tumor-mimicking conditions (i.e., in hypoxia (1% O_2) and 10 vol.% 4T1-conditioned media). Each day for 5 days, cells were harvested, stained and analyzed for molecular expression by flow cytometry. Expression of each biomarker was normalized to unpolarized BMDMs.

Macrophages carrying IFNγ backpacks strongly exhibited traits of M1 phenotypes. We investigated the relative expression of M1 biomarkers, including inducible nitric oxide synthase (iNOS), major histocompatibility complex class II (MHCII) and CD80 due to their important role in innate immunity. iNOS is involved in the production of nitric oxide (NO), which serves as a potent tumoricidal and antimicrobial agent (*119*). MHCII proteins are involved in antigen presentation to T cells to facilitate adaptive immunity (*120*). MHCII is

expressed on macrophages with M1 and M2 phenotypes, but it is overexpressed on cells with M1 polarizations. CD80 is a co-stimulatory molecule used to trigger an adaptive immune response in the presence of an antigen-presenting cell (*121*).

Macrophages displaying IFNγ backpacks showed marked increases in iNOS, MHCII and CD80 expression relative to unpolarized cells (**Figure 3.4A**). Here, we make several important observations. First, expression of both iNOS and MHCII in cells displaying IFNγ backpacks was synergistic. Specifically, iNOS expression was 629.3-fold higher in the IFNγ backpack group compared to only 2.4-fold and 1.3-fold higher in groups treated with blank backpacks and IFNγ alone, respectively, after 48 h. Similarly, MHCII expression was 6.3-folder higher in the IFNγ backpack group compared to only 0.8-fold and 1.4-fold higher in groups treated with blank backpacks and IFNγ alone, respectively, after 48 h. While the origins of this apparent synergy are unknown, the effects may arise, at least in part, from local and sustained concentration gradients of IFNγ formed near the cells to which the backpacks are bound, thus enhancing the activity of IFNγ. Second, the data suggest that the presence of backpacks without IFNγ (blank backpacks) induces modest, but non-negligible phenotypic shifts toward M1 phenotypes, as evidenced by increased expressions of iNOS, MHCII and CD80. This effect could be due to frustrated phagocytosis, whereby macrophages enhance their inflammatory phenotypes upon encountering large foreign objects (*122, 123*). Third, the expression of M1-related markers in BMDMs carrying IFNγ backpacks was more durable than that of BMDMs cultured with free IFNγ. Specifically, the relative expression of iNOS decreased by 89.1% after 5 days in cells treated with free IFNγ, but only by 59.1% in cells with IFNγ backpacks. Further, the relative expression of MHCII and CD80 decreased by 30.1% and 37.6%, respectively, after 5 days for cells treated with free IFNγ; however, the relative expression of MHCII and CD80 in cells treated with IFNγ backpacks actually increased by 95.7% and 248.4%, respectively, after 5 days. Last, no major differences in marker expression were observed between BMDMs with IFNγ backpacks in standard culture conditions versus tumor-mimicking conditions, which we hypothesize will be critical to allow BMDMs to maintain M1 phenotypes *in vivo*. Overall, these data suggest that IFNγ backpacks potentiate a shift in macrophage polarization toward M1 phenotypes that is more potent and durable than free IFNγ.

We also investigated the expression of markers associated with M2 phenotypes: vascular endothelial growth factor (VEGF), hypoxia-inducible factor 1α (HIF-1α) and CD206 (**Figure 3.4B**). VEGF is often overexpressed in TAMs, which serves a source of angiogenic cytokines and proteases to promote tumor vascularization (*124*). HIF-1α is also overexpressed by TAMs, which suppresses T cell function and promotes tumor progression (*125*). CD206 is the mannose receptor, which has been linked to immunosuppression, angiogenesis and metastasis (*126*). Cells displaying IFNγ backpacks showed elevated levels of all three M2 markers relative to untreated controls; however, the magnitude of this increase was modest. The highest fold-changes observed were 2.7, 3.3 and 2.6 for VEGF, HIF-1α and CD206, respectively. These changes were less substantial than those observed for M1 markers, and the relative expression of all three M2 markers returned to values near the expression of untreated controls after 5 days.

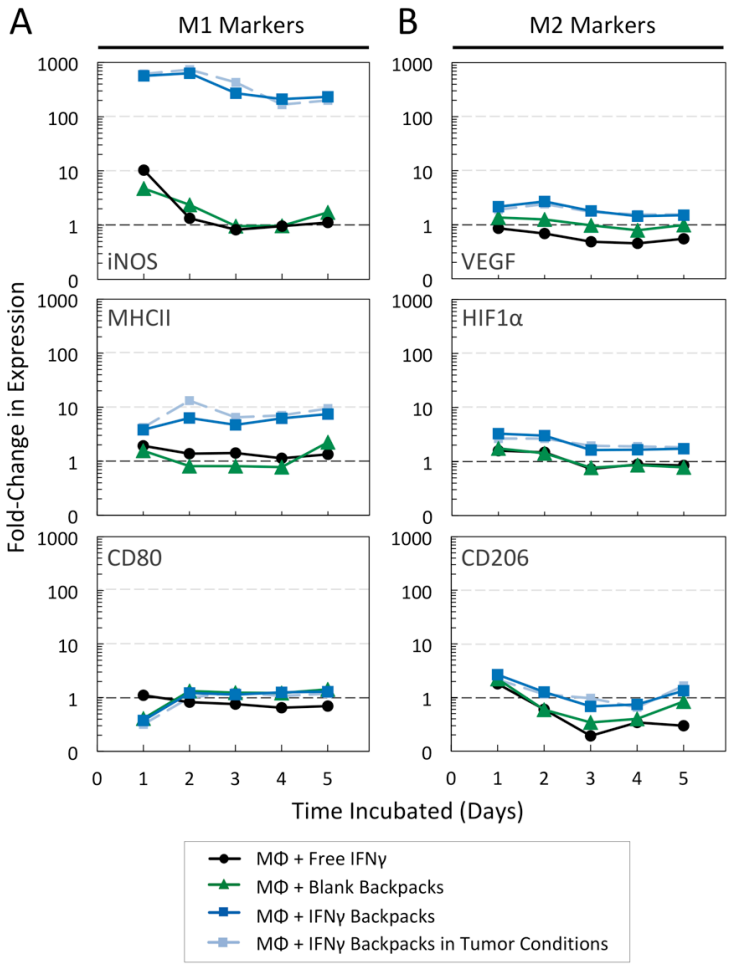

Figure 3.4: Phenotypic evaluation of macrophages (MΦs) carrying IFNγ backpacks *in vitro*. BMDMs were cultured for 5 days with free IFNγ (16 ng/mL; black lines), blank backpacks (0 ng/mL IFNγ; green lines) and IFNγ backpacks (16 ng/mL equivalent) in normoxia (dark blue lines) and tumor-mimicking conditions (1% O_2 and 10 vol.% tumor-conditioned media; light blue lines). Cellular expression of representative (A) M1 markers (iNOS, MHCII and CD80) and (B) M2 markers (VEGF, HIF-1α and CD206), relative to that of unpolarized macrophages (without IFNγ or backpacks). Graphs are logarithmic (n = 10,000 events / data point).

3.3.3 IFNγ backpacks enable macrophages to maintain M1 phenotypes in vivo

Next, we sought to test our central hypothesis that macrophages carrying IFNγ backpacks can maintain their M1 phenotypes *in vivo*. We chose orthotopic 4T1 breast tumors as a model immunosuppressive environment due to its association with chemotherapy resistance, tumor metastasis and lack of tumor-specific antigens, making them challenging targets for CAR T cell therapy (*113, 127, 128*). To distinguish injected macrophages from TAMs, we stained BMDMs with VivoTrack 680. Macrophages were injected intratumorally. Distributions of injected cells were monitored each day for 5 days using an *in vivo* imaging system (IVIS) (**Figure 3.5**). After 5 days, a second injection was administered as before. Mouse body weight, tumor growth, tumor radiance and necrosis were monitored to the end of the study (**Figure 3.6**). Two days after the second injection, mice were euthanized and their tumors were extracted, digested and tumor-associated immune cells ($CD45^+$) were isolated. Dendritic cells and macrophages were stained and identified by hierarchical gating (**Figure 3.7**). Macrophages

were phenotyped as the method used for in vitro phenotyping, except markers were used for arginase 1 (arg-1) instead of VEGF. Arg-1 affects NO synthase and downregulates NO production (*129*). Expression of each marker was normalized to that of endogenous TAMs in mice treated with saline.

Macrophages carrying IFNγ backpacks retained M1 polarizations in solid tumors for at least 48 h (**Figure 3.8A**). Relative to the TAMs of control mice (i.e., mice injected with saline), the expression of iNOS, MHCII and CD80 in injected macrophages displaying IFNγ backpacks was significantly higher than that of injected cells displaying blank backpacks or injected cells with free IFNγ. Interestingly, the relative increase in MHCII and CD80 expression of cells carrying IFNγ backpacks surpassed that of cells carrying IFNγ backpacks *in vitro* (12.3 and 3.0-fold *in vivo* versus 6.3 and 1.3-fold *in vitro* for MHCII and CD80, respectively; **Figure 3.4A**, **Figure 3.8A**). However, the relative increase in iNOS was less substantial *in vivo* (7.2-fold *in vivo* versus 629.3-fold *in vitro*). The reduction was due to an elevated basal expression of iNOS in the TAMs of control mice compared to untreated control cells *in vitro*. This observation is consistent with findings by others that iNOS expression can increase in M2-polarized TAMs (*130*). We also found no statistically significant differences in the relative expression of HIF-1α and CD206 between macrophages carrying IFNγ backpacks and those carrying free backpacks or injected with free IFNγ. Even though cells carrying IFNγ backpacks displayed significantly higher levels of Arg-1 relative to those carrying blank backpacks or injected with free IFNγ, they did not show a significant increase the expression of Arg-1 relative to untreated TAMs.

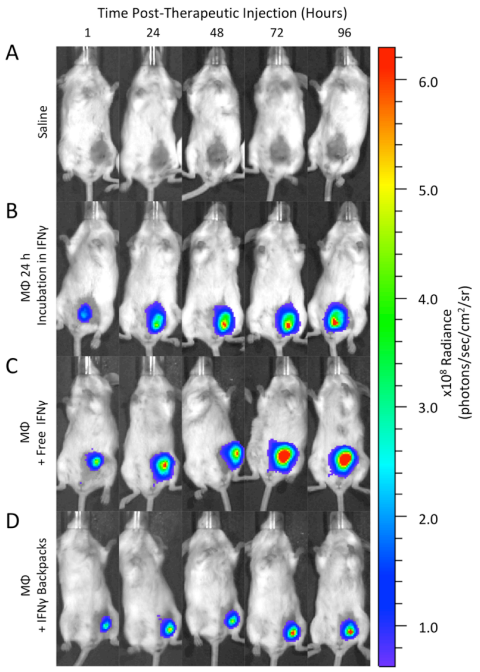

Figure 3.5: Intratumoral distribution of injected macrophages (MΦs) after a single injection. Grayscale images with overlaid recordings of average radiance, as determined by an *in vivo* imaging system (IVIS), of mice injected with: (A) saline and (B−D) MΦs labeled with VivoTrack 680 near-infrared dye. Prior to injection, MΦs were (B) polarized *ex vivo* for 24 h with 16 ng/mL IFNγ (MΦ 24 h incubation in IFNγ), (C) left unpolarized and mixed with 50 ng free IFNγ immediately prior to injection (MΦ + free IFNγ), and (D) left unpolarized and bound to IFNγ backpacks at a concentration of 50 ng equivalent IFNγ immediately prior to injection (MΦ + IFNγ backpacks).

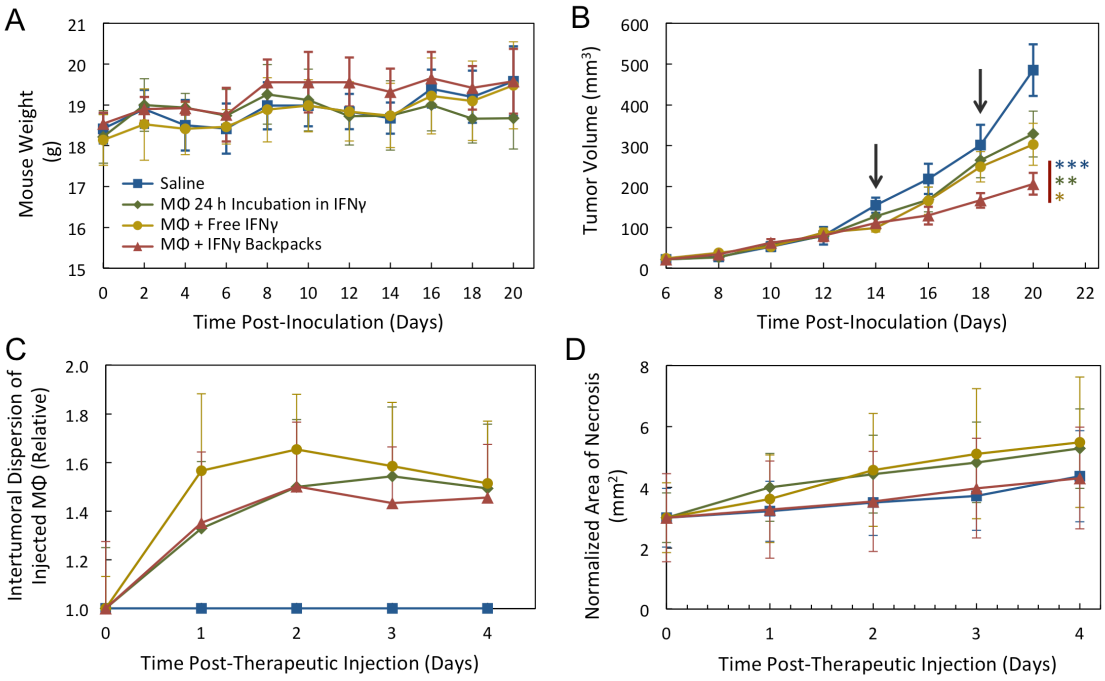

Figure 3.6: Efficacy of IFNγ backpacks to treat BALB/c mice with 4T1 triple negative breast carcinomas. Prior to injection, macrophages (MΦs) were (i) left unpolarized (saline, blue), (ii) polarized *ex vivo* for 24 h with 16 ng/mL IFNγ (MΦ 24 h incubation in IFNγ, green), (iii) left unpolarized and mixed with 50 ng free IFNγ immediately prior to injection (MΦ + free IFNγ, yellow) and (iv) left unpolarized and bound to IFNγ backpacks at a concentration of 50 ng equivalent IFNγ immediately prior to injection (MΦ + IFNγ backpacks, red). (A) Average mouse body weight in all groups. (B) Tumor growth curves for all groups. Solid arrows indicate days of intratumoral injections. (C) Distribution of injected MΦs relative to their distribution immediately after injection, as determined by an IVIS (raw images in Figure 3.5). (D) Progression of necrosis. Photographs of tumors on dehaired mice were taken each day after the first injection. To evaluate if the treatment group altered the rate of necrosis, the average area of necrosis was determined for each group by ImageJ (NIH) and normalized to the first day. No significant differences were observed. Time in (C) and (D) is with respect to the first therapeutic injection (n = 5 for all graphs).

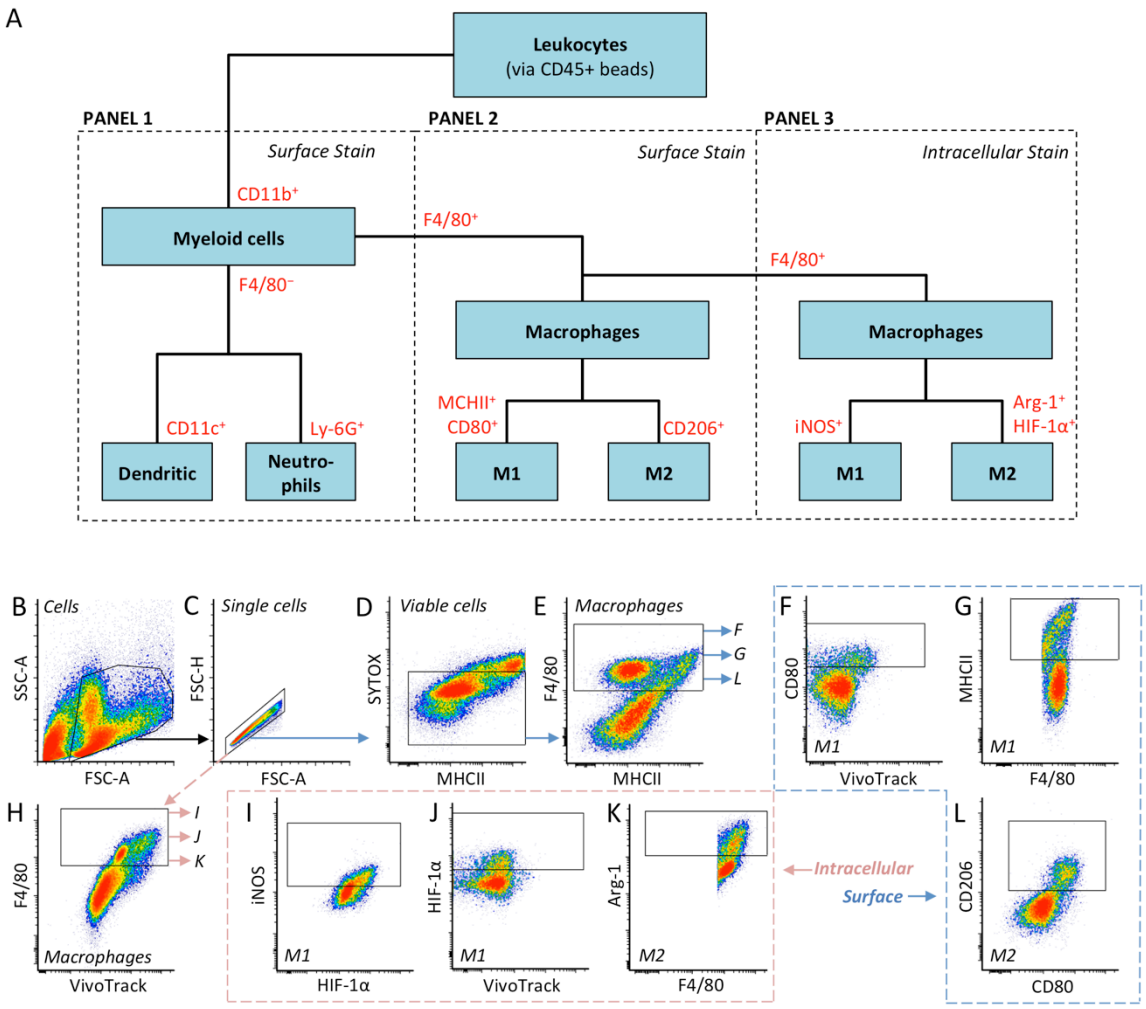

Figure 3.7: Phenotyping tumor-associated immune cells. (A) Panel organization for phenotyping tumor-associated immune cells from orthotopic 4T1 breast tumors. Tumor-associated leukocytes were split into 3 panels for separate staining and inspection by flow cytometry, as demarcated by the dotted grey boxes. Phenotypic markers used for identifying different cell populations are shown in red text. Corresponding isotype controls are listed in *Table 3.1*. (B–L) Gating schema for phenotyping TAMs by flow cytometry. Hierarchical gates were drawn for (B) cells, (C) single cells, (D) viable cells and then (E) macrophages. Subplots were drawn from (E) to stain for (F) CD80, (G) MHCII and (L) CD206 on cellular surfaces (light blue dotted lines). To stain for intracellular markers, a subplot was drawn from (C) to identify viable and non-viable macrophages (H). From (H), subplots were drawn for (I) iNOS, (J) HIF-1α and (K) Arg-1 (pink dotted lines). Figure 3.8B displays the relative change in the median intensity for (F, G, I, J, L and K). We note that the same schema was used for phenotyping injected macrophages, with the additional criteria of gating for macrophages stained with VivoTrack 680 near-infrared dye.

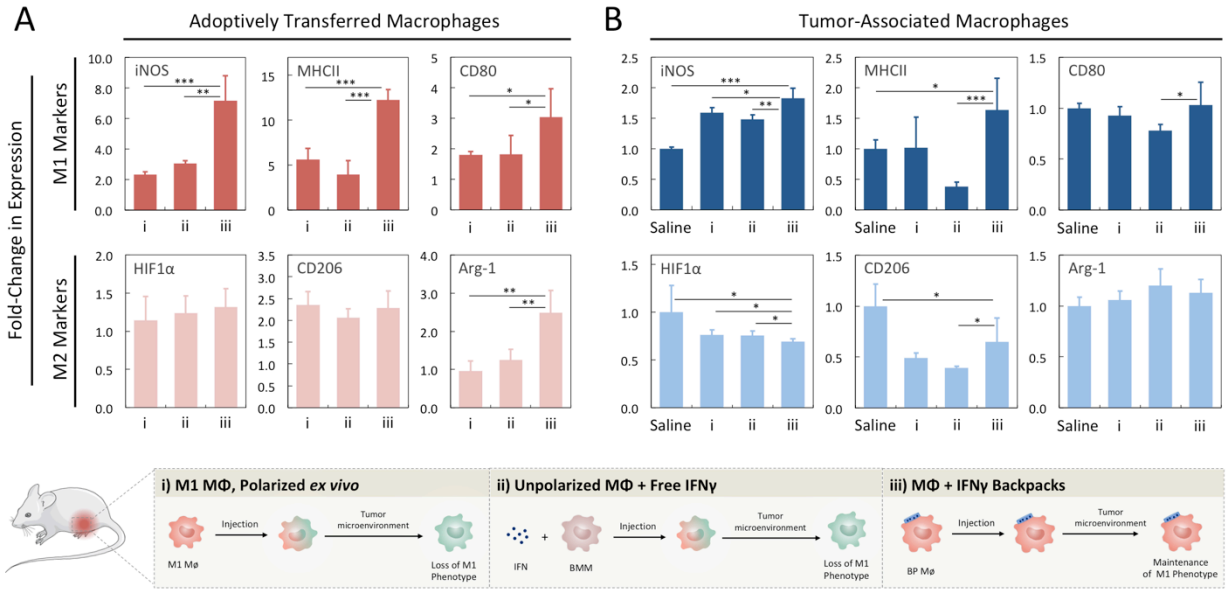

Figure 3.8 IFNγ backpacks promote pro-inflammatory phenotypes in solid tumors. (A) Polarization of adoptively transferred macrophages (MΦs) 48 h after injection. BMDMs were polarized *ex vivo* for 24 h with 16 ng/mL IFNγ (i), left unpolarized and injected with 50 ng free IFNγ (ii) or left unpolarized, bound to IFNγ backpacks at a dose of 50 ng equivalent IFNγ and injected (iii). Bar graphs indicate the fold-change in the median expression of representative M1 biomarkers (iNOS, MHCII and CD80; *top row*) and M2 biomarkers (HIF-1α, CD206 and Arg-1; *bottom row*), relative to their native expression in endogenous TAMs. (B) Polarization of endogenous TAMs 48 hours after injection of groups described in (A). Bar graphs indicate the fold-change in the median expression of representative M1 biomarkers (*top row*) and M2 biomarkers (*bottom row*) relative to the native expression of endogenous TAMs (*leftmost bars in* (B)). For all bar graphs, n = 5.

3.3.4 IFNγ backpacks shift the polarization of TAMs toward M1 phenotypes

After demonstrating that the IFNγ backpacks allowed macrophages to maintain their phenotypes *in vivo*, we sought to evaluate the phenotype of TAMs in response to adoptive transfer of macrophages carrying IFNγ backpacks (see **Figure 3.7** for hierarchical gating). An emergent therapeutic strategy to attack tumorous tissues is via repolarizing TAMs toward M1 phenotypes (*131-136*). TAMs affect cancer progression in a manner that is dependent on their polarization (*137-139*). Macrophages possessing M1 phenotypes have been shown to improve outcomes in cancer therapy due to their antigen-dependent and antigen-independent facets. This gives macrophages the potential to be useful in tumors that lack the tumor-specific antigens typically required for adoptive T cell therapy (*140-142*). This has been demonstrated by others through the delivery of nanoparticles with payloads that inhibit colony stimulating factor 1 receptor (CSF1-R) and Src homology region 2 (SH2) domain-containing phosphatase 1 (SHP2) pathways on macrophages (*143*) as well as the delivery of nanoparticles encapsulating microRNA-125b (*144*). Still, supplying a sufficient concentration of immunomodulatory factors to repolarize TAMs while minimizing toxicity remains a major challenge.

We administered two intratumoral injections of macrophages with 50 ng IFNγ per mouse, which is 100-fold lower than the maximum total dose (MTD) administered in other studies

(*145*). Our motivation for the comparatively low dose was to supply sufficient IFNγ to maintain the M1 polarization of adoptively transferred macrophages while minimizing toxic side effects (*146*). Here, mice received two equivalent injections of: (i) macrophages polarized *ex vivo* for 24 h in 20 ng/mL IFNγ (M1-polarized), (ii) unpolarized macrophages injected with 50 ng free IFNγ, (iii) macrophages carrying IFNγ backpacks that encapsulated 50 ng IFNγ, or saline (control) (**Figure 3.8B**). Administrations were separated by 5 days.

We found that TAMs of mice treated with the IFNγ backpack therapy were polarized toward M1 phenotypes, as evidenced by significantly increased expressions of iNOS (1.8-fold) and MHCII (1.6-fold) compared to TAMs of mice treated with saline (**Figure 3.8B**). Second, the relative increase of iNOS expression in TAMs of mice treated with the IFNγ backpack therapy was significantly higher than in TAMs of mice treated with macrophages polarized *ex vivo* (1.8-fold versus 1.0-fold, respectively) (ii). Third, the relative increase of CD80 expression in TAMs of mice treated with the IFNγ backpack therapy was significantly higher than in TAMs of mice treated with macrophages plus free IFNγ (1.03-fold versus 0.78-fold, respectively) (iii).

We also investigated the relative expression of M2 markers in TAMs. We found that relative HIF-1α expression in TAMs of mice treated with the IFNγ backpack therapy was significantly lower than all other groups (**Figure 3.8B**). This finding was particularly interesting, as relative HIF-1α expression in macrophages displaying IFNγ backpacks was higher *in vitro* (**Figure 3.4B**). TAM expression of CD206 was also significantly lower for mice treated with IFNγ backpacks than saline. However, the group that displayed the lowest relative expression of CD206 in TAMs was in mice treated with macrophages plus free IFNγ. No significant differences were observed in the relative expression of Arg-1. Overall, these data show that macrophages carrying IFNγ backpacks can shift the polarization TAMs toward M1 phenotypes at a drastically reduced dose, 100-fold lower than the MTD (*145*). Additionally, the same dose of free IFNγ was not able to potentiate a shift in TAM polarization. Given this these findings, we sought to examine the therapeutic efficacy of macrophages with IFNγ backpacks.

3.4.5 Antitumor efficacy of macrophages carrying IFNγ backpacks.

To evaluate the therapeutic efficacy of IFNγ backpacks, we investigated the formation of metastases, tumor growth kinetics and overall survival of immunocompetent BALB/c mice burdened with 4T1-Luc cells. 4T1-Luc cells were chosen due to their high luciferase expression, enabling bioluminescence imaging to visualize the formation of metastatic colonies in the chest cavities by radiance using an IVIS. We administered the same low dose of IFNγ as before to understand the influence of the IFNγ backpacks. After tumors became palpable (~50 mm^3), mice received two equivalent injections (separated by 5 days) of: (i) saline, (ii) unpolarized macrophages with 50 ng free IFNγ and (iii) macrophages carrying IFNγ backpacks encapsulating 50 ng IFNγ.

We found that mice treated with the IFNγ backpack therapy had significantly fewer metastatic nodules than control mice (**Figure 3.9A**). Chest cavities of mice given the IFNγ backpack therapy showed 5.2-fold lower radiance compared to that of mice treated with saline and 4.9-fold lower radiance compared to that of mice treated with macrophages and free IFNγ (**Figure 3.9B**). This suggests that, even at a low dose, IFNγ backpacks are able to significantly inhibit the formation of metastatic colonies. To assess toxicity, peripheral blood was isolated via cardiac puncture immediately after euthanasia and serum was analyzed for cytokines. Analysis revealed that all treatments were well-tolerated, and IFNγ levels were below the limit of

detection in all groups. This result was expected given that the dose of IFNγ was 100-fold lower than the MTD used previously (*145*).

We also assessed tumor morphology and dendritic cell infiltration. For both analyses, tumors from BALB/c mice burdened with 4T1 breast cancer (from the study in section 3.3.3; **Figure 3.8B**) were isolated and cut into four vertical portions. One portion was sectioned for histology and the remaining three portions were digested and stained for phenotypic evaluation by flow cytometry. The top half of the tumor revealed large areas of digested tissue, whereas the bottom half remained largely intact (**Figure 3.9C**). This finding suggests that the areas of highest tumor clearance occurred in regions where the injected cells resided, as all treatments were injected toward the top each tumor. Interestingly, we found that mice treated with the IFNγ backpack therapy had significantly higher infiltration of $CD11c^+$ dendritic cells (**Figure 3.9D**), as determined by the gating schema shown in **Figure 3.7**. While not studied here, we believe this could be a promising future direction of study, as higher dendritic cell populations could be used to instruct adaptive immunity as a cancer vaccine (*147, 148*).

Last, we evaluated the progression of tumor growth and overall survival of mice treated with the IFNγ backpack therapy (**Figure 3.9, E-G**). Consistent with the metastasis data, mice injected with the IFNγ backpack therapy showed significantly smaller tumors than the two controls 14−23 days after the second therapeutic injection. By 37 days post-inoculation, tumors of mice receiving the IFNγ backpack therapy were 51.9% and 48.3% smaller than those of mice receiving injections of saline and macrophages with free IFNγ, respectively. Mice receiving the IFNγ backpack therapy showed significantly improved survival, as determined by a log-rank test. The average time of survival for mice treated with saline, macrophages with free IFNγ and macrophages carrying IFNγ backpacks was 30.7, 31.7 and 35.9 days after inoculation, respectively. Together, the slowed tumor growth, smaller tumor volumes and decrease in serum IL-6 of mice treated with the IFNγ backpack therapy likely potentiated the reduced metastatic burdens and improved overall survival compared to controls.

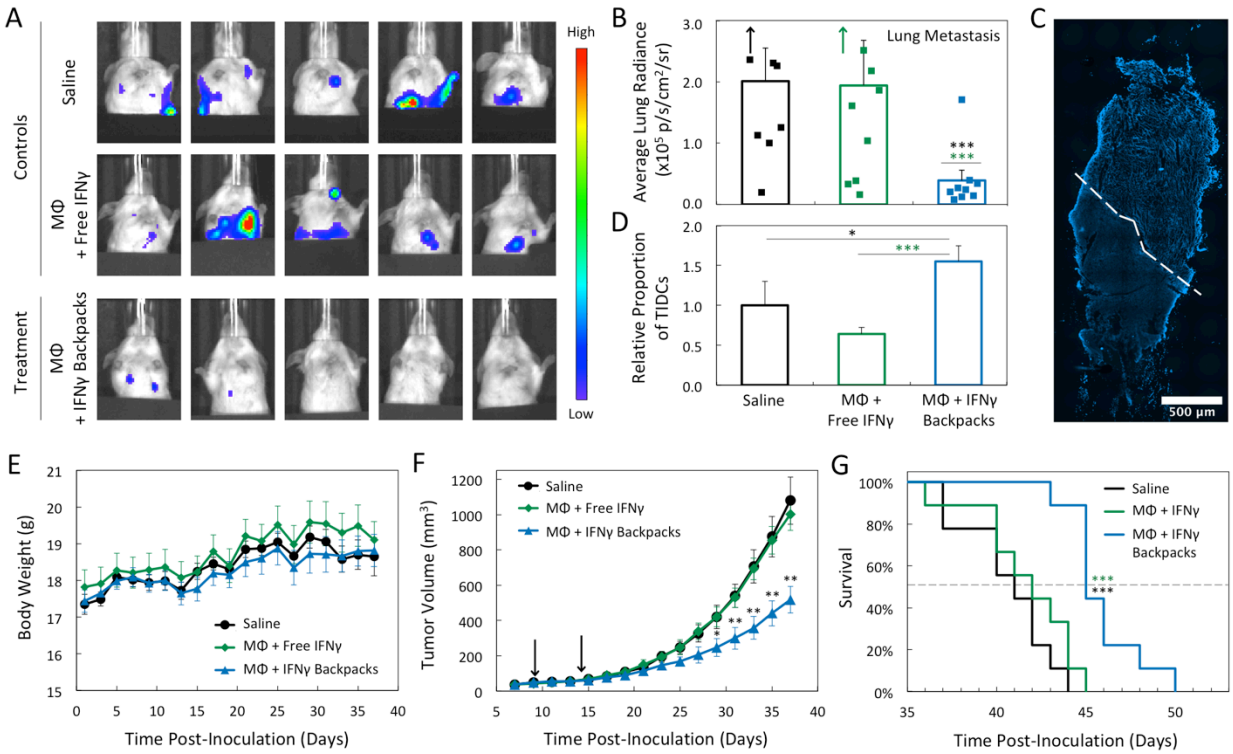

Figure 3.9: Efficacy of IFNγ backpacks for reducing metastasis and tumor burden of 4T1 mammary carcinomas. (A) *In vivo* bioluminescence imaging of metastatic colony formation in the chest cavities of mice burdened with 4T1-Luc cells 32 days after inoculation (primary tumor outside of view). Five representative images per treatment group are shown. (B) Average radiance from bioluminescence in the chest cavities of the mice in (A) (n = 9). (C) Representative histological section of a 4T1 tumor treated with macrophages carrying IFNγ backpacks. Dotted line separates regions of cleared (*top*) and intact tumorous tissue (*bottom*). (D) Relative proportion of tumor-infiltrating dendritic cells (TIDCs) in solid 4T1 tumors revealed through tumor-associated immune cell phenotyping (determined by $CD45^+$, $SYTOX^-$ and $CD11c^+$; n = 5). (E) Weight changes of mice burdened with 4T1-Luc tumors in different groups (n = 9). (F) Growth kinetics of tumors in the groups shown in (E). Black arrows indicate days of therapeutic injections. (G) Survival of mice in (E). Statistical significance was determined via a log-rank test.

3.4 Discussion

We have developed a particle-based strategy, referred to as backpacks, which can regulate the phenotype of adoptively transferred macrophages. We demonstrate that IFNγ backpacks: (i) securely attach to macrophage surfaces and evade phagocytosis for several days, (ii) show favorable release kinetics of encapsulated cytokines to induce potent and durable shifts in macrophage polarization and (iii) allow adoptively transferred macrophages to maintain their phenotypes deep within the immunosuppressive milieu of solid tumors. Backpacks were prepared from biodegradable materials that enable facile preparation, long-term storage and simple metabolic clearance, all of which are favorable for clinical translation. Furthermore, injected macrophages were allogeneic, which reduces the timescale of preparing cell transfers from weeks (i.e., for CAR T cell therapy (*31*)) to several hours.

In addition to validating our central hypothesis, we also show that low doses of IFNγ can induce a shift in the polarization of TAMs and potentiate an antitumor response against 4T1 triple negative breast tumors. While the doses reported here are not optimized, we show that the slowed tumor growth suppresses formation of metastases and improves overall survival. Future studies will investigate the optimal loading of IFNγ into backpacks and their release kinetics to enhance this therapeutic efficacy against solid tumors. Additionally, future work can combine backpacks with adjuvant therapies to enhance therapeutic effects.

3.5 Conclusion

In summary, this work offers a strategy to regulate the phenotype of adoptively transferred macrophages, which can further be used to address a broad range of inflammatory diseases, including cancer, autoimmune disorders, and infectious diseases.

Chapter 4: Macrophage-Hitchhiking Gadolinium Micro-patches for Detecting Traumatic Brain Injury

In this work, I invented discoidal hydrogel microparticles by identifying the main hydrogel components in collaboration with Dr. Yongsheng Gao, followed by independently developing and optimizing the fabrication process for particle production at scale. For all the in vitro and mouse studies, I designed experiments, developed protocols, performed tests, and analyzed and interpreted data. Special thanks to Dr. Tao Sun for operating MRI as well as Neha Kapate and Dr. Kyung Soo Park for helping with performing small animal studies. For large animal studies, I coordinated colleagues for scaling up material preparation, designed and modified the pig studies with clinical collaborators, and analyzed and interpreted MRI data. Many thanks to my collaborators at Boston Children Hospital (BCH), including Dr. Rebekah Mannix, Masen L. Boucher, and Kaitlyn Warren, for supporting the hands-on porcine works. Special thanks to the Dr. Camilo Jaimes Cobose, the radiologist at BCH, to provide clinical insights for MRI interpretation as well as Dr. Vineeth Chandran Suja for developing the procedures for imaging analysis with me. Many thanks to my wonderful collogues for helping with particle scale-up and macrophage collection for porcine studies, including Neha Kapate, Suyog Shaha, Ninad Kumbhojkar, Supriya Prakash, Andrew Lu, Bolu Ilelaboyea, Morgan Janes, Dr. Rick Liao, Dr. Kyung Soo Park, Dr. Michael Dunne, and Dr. Vineeth Chandran Suja.

4.1 Introduction

4.1.1 Choroid plexus (ChP)-mediated leukocyte recruitment

Choroid plexus (ChP), the primary source of cerebrospinal fluid (CSF) in the brain, is a highly vascularized structure lined by a specialized epithelial layer called ependyma and serves as the blood-CSF (BCSF) barrier (*149*). ChP has only recently gained attention for its role as the gatekeeper of the infiltration of peripheral immune cells into the CSF (*150*). Indeed, ChP orchestrates the recruitment of leukocytes into the central nervous system (CNS) during multiple pathologies by increasing the expression of adhesion molecules and enhancing the secretion of chemokines and cytokines, thus making it a key player in numerous CNS disorders (*151, 152*). Accordingly, though still understudied in clinical neuroimaging, there has been growing interest in imaging the morphological or functional changes in ChPs for diagnostic and prognostic evaluation of various neuro-inflammatory disorders (*153*).

4.1.2 Imaging leukocyte infiltration via ChP for mild TBI diagnosis

Due to its high sensitivity to physical forces, ChP is postulated to play a key role in the pathology of traumatic brain injury (TBI) (*154*). In particular, brain injuries are known to induce disruption of the BCSF barrier followed by leukocyte infiltration (*155*). We hypothesized that this unique attribute of ChP can be exploited to facilitate the clinical diagnosis of traumatic brain injury (TBI).

TBI, also called a silent epidemic, is a global challenge that represents one of the leading causes of death and disability worldwide with an estimated 69 million individuals affected each year (*156, 157*). TBI can be categorized into mild, moderate, and severe categories, with mild TBI (mTBI) accounting for approximately 70-90% of the reported cases (*158, 159*). While mTBI is characterized by transient neurophysiological alterations, long-term effects of mTBI can persist for months to years (*160, 161*). More importantly, mTBI is also associated with an increased risk of neuropsychiatric and neurodegenerative diseases, such as depression, dementia, and Parkinson's disease (*162-164*). Magnetic resonance imaging (MRI) is commonly used in evaluation of patients suspected of TBI, including mTBI (*165*). The most routinely used MRI contrast agents to enhance diagnostic efficiency are gadolinium (Gd(III))-based contrast agents (GBCAs) (*166*). However, even with the use of GBCAs, detection of mTBI remains a major challenge due to the transient nature of the posttraumatic symptoms as well as the lack of objective and measurable evidences of brain injury upon neuroimaging (*167*). Indeed, 60-90% of the mTBI cases can go underdiagnosed even after a clinical investigation (*168, 169*).

mTBI, though undetectable in conventional MRI, has been reported to induce physiologically relevant changes in CSF (*170, 171*). We hypothesized that the impact of this alteration is further amplified by leukocyte infiltration via the BCSF barrier, and thus imaging of immune cell infiltration into the ChP can potentially offer a diagnosis of sub-clinical mTBI. While many circulating immune cells are likely to infiltrate across the perturbed BCSF barrier, macrophages, owing to their superior inflammation-homing ability driven by the chemotactic gradient, are key players in brain infiltration (*172-175*).

4.1.3 Our approach

Here, we report a contrast agent that is specifically designed to leverage macrophage infiltration across the BCSF barrier. Specifically, we report **G**d(III)-**L**oaded **A**nisotropic **M**icropatches (GLAMs) that adhere to macrophages for improvement of mTBI diagnosis. GLAMs are hyaluronic acid-based discoidal microparticles, which bind to macrophages, but resist phagocytosis due to their anisotropic morphology, enabling stable loading of Gd(III) on the cell surface. GLAMs can be fabricated at scale and can incorporate Gd(III) with relaxivities remarkedly greater than commercial GBCAs. Studies in a porcine mTBI model confirm that macrophage-hitchhiking GLAMs provide a differential signal in the region of ChP and lateral ventricles of mTBI at Gd(III) doses 500-1000-fold lower than those used in the current clinical standard Gadavist® (**Figure 4.1**). Under the same mTBI conditions, Gadavist® did not offer a differential signal even at clinically used doses.

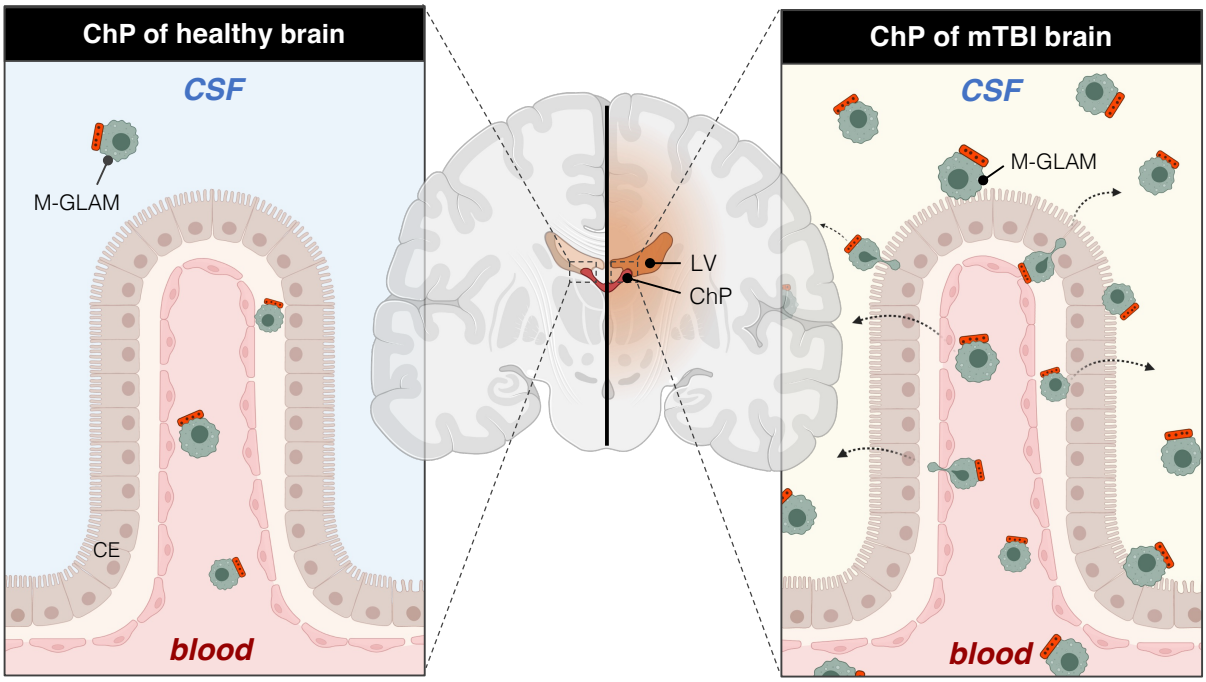

Figure 4.1: Schematic illustration of macrophage-hitchhiked Gd(III)-loaded anisotropic micropatches (M-GLAMs) crossing the brain-cerebrospinal fluid (CSF) barrier at choroid plexus (ChP) for mild TBI diagnosis. Upon the condition of mTBI, ChP serves as a gateway to facilitate M-GLAM infiltrating into the CSF of lateral ventricle (LV). This enhanced recruitment of M-GLAM in the inflamed brain, compared to the heathy one, leads to a differential MRI signal in the region of interest (i.e., choroid plexus and lateral ventricle). CE: choroidal epithelium. Created with BioRender.com.

4.2 Materials and Methods

Materials. Regarding materials for GLAM fabrication, hyaluronic acid (HA, 250k) was purchased from Creative PEGWorks; gadolinium(III) oxide, methacrylic acid, methacrylic anhydride were obtained from Sigma; polydimethylsiloxane (PDMS; SYLGARD™ 184 Silicone Elastomer Kit) was purchased from Ellsworth Adhesives; poly(vinyl alcohol) (PVA) was obtained from Millipore Sigma; Alexa Fluor™ 555 Hydrazide, Alexa Fluor™ 488 Hydrazide, and 1-Ethyl-3-(3-dimethylaminopropyl)carbodiimide (EDC) were purchased from Thermo Fisher Scientific. For ICP-MS sample preparation and analysis, double distilled nitric acid was purchased from Spectrum Chemical; hydrochloric acid was obtained from Sigma;

RIPA lysis buffer was obtained from EMD Millipore; ICP Single-Component Standards (gadolinium, thulium, and indium) were purchased from High-Purity Standards. For cell culture and characterization, RPMI-1640 media, Dulbecco's modified eagle medium (DMEM) F12 media, fetal bovine serum (FBS), penicillin and streptomycin (Pen Strep), and heparin-coated plasma preparation tubes were obtained from Thermo Fisher Scientific; recombinant murine macrophage colony stimulating factor (M-CSF) was obtained from PeproTech; Bambanker cell freezing media was obtained from VWR International; cell staining buffer was purchased from Biolegend; CellTiter 96® AQueous One Solution Cell Proliferation Assay (MTS assays) was obtained from Promega. Female BALB/c mice (6–8 weeks old) were obtained from Charles River. Castrated male Yucatan miniature swine (6 month old) were were obtained from Sinclair Bio-Resources.

Synthesis and characterization of gadolinium methacrylate ($Gd(MAA)_3$). $Gd(MAA)_3$ was prepared by the method modified from Wang et al (*176*). Briefly, Gd_2O_3 (Sigma), methacrylic acid (Sigma), and DI water were mixed with a molar ratio of 1:10:20 into a 500-mL round-bottom flask, followed by reacting at 90˚C for 1 h. The hot solution was then quickly filtered by passing through the filter paper. Next, the filtrate was concentrated by rotary evaporator at 50˚C. $Gd(MAA)_3$ were precipitated as white solids by adding ethyl alcohol in excess to the filtrate. The precipitates were filtered off by filter paper, washed with additional ethyl alcohol twice, and finally dried under vacuum. The yield of the final product was about 64%. The Fourier transform infrared (FT-IR) spectra of the final product were recorded on a Nicolet™ iS50 FTIR Spectrometer and processed using the Bruker OPUS Spectroscopy Software to confirm the successful formation of $Gd(MAA)_3$.

Synthesis and characterization of methacrylated hyaluronic acid (HAMA). HAMA was synthesized according to a previously described procedure from Guvendiren et al (*177*). Briefly, 0.5 g of HA (250k Da, Creative PEGWorks) was dissolved in DI water (1 wt%) with stirring at RT overnight. Methacrylic anhydride (MA, Sigma) was added to the HA solution (1.25 mL MA per gram of HA) and reacted at pH 8-9 under stirring in ice bath for 8 h, followed by overnight stirring at 4 °C. Further reaction was performed by adding MA (0.5 ml MA per gram of HA) and reacting at pH 8-9 on ice for 4 h. For purification, the reaction solution was dialyzed (MWCO = 3.5 kDa, SpectraPor) against DI water for 48 h with water changed three times per day. Finally, the product was lyophilized and collected by the Labconco FreeZone Triad Freeze Dryer. The functionality and purity of the final product was determined by ^1H NMR (Bruker N400 NMR) in D_2O and the spectra were processed and plotted using the MestReNova software.

Fluorescent HAMA was prepared by conjugating Alexa Fluor™ 488 dye or Alexa Fluor™ 555 dye on HAMA. 0.1 g of HAMA was dissolved in DI water (1 wt%) with stirring at 37˚C for 1.5 h with a pH adjustment to the value of 5.5. 0.1 mL of 1-Ethyl-3-(3-dimethylaminopropyl)carbodiimide (EDC) in dimethyl sulfoxide (DMSO; 5 wt%) and 0.19 mL of Alexa Fluor™ 488 or 555 Hydrazide in DI water (0.5 wt%) were then prepared and quickly added to HAMA solution, followed by reaching for 2 h. The molar ratio of florescent dye, EDC, and HAMA was 0.3:10:100. Next, the sample was dialyzed (MW cutoff = 3.5 kDa, SpectraPor) against DI water for 48 h. The final product was obtained by lyophilization.

Hydrogel synthesis and rheology characterization. Our hydrogel was composed of an HAMA mixture (mass ratio of regular HAMA and fluorescent HAMA = 10:1), poly(ethylene glycol) dimethacrylate (PEGDMA, 1k Da, Polysciences), Gd(MAA)3, and Irgacure 2959 photoinitiator (I2959, Sigma). To prepare the hydrogel mixture, Gd(MAA)3 solution was first

prepared in DI water (1 wt%) with sonication. The regular HAMA and fluorescent HAMA were dissolved in Gd(MAA)3 solution at the concentration of 3 wt% at RT overnight. Next day, I2959 was dissolved in Gd-MAA solution (2.5 wt%) at 60˚C with stirring for at least 10 min, and PEGDMA solution was prepared in Gd-MAA solution (20 wt%) at 37˚C. The final hydrogel solution was prepared by mixing the solutions of regular HAMA, fluorescent HAMA, I2959, PEGDMA, and Gd(MAA)3 with a volume ratio of 10:1:4.2:1.7:1.

The rheological properties of hydrogels were determined by an HR 20 discovery hybrid rheometer (TA instruments) using a 20mm parallel plate with an accessory of UV curing system (Exfo OmniCure S2000). A series of rheological tests were performed, including oscillatory time-sweep, amplitude-sweep, and frequency-sweep experiments. To monitor the dynamic formation of crosslinked hydrogel, hydrogel precursor solution was first loaded on the plate, and the time-sweep rheological test was conducted at 0.5% strain and a fixed frequency of 10 rad/s, where the storage modulus (G') and loss modulus (G") were recorded over time at RT. At 30 sec, the sample was exposed to UV (365nm; 17 mW cm^{-2}) for 10 min. Next, a range of oscillatory amplitude from 0.01% to 157% was applied with a fixed angular frequency of 10 rad/s. This to confirm the previously selected strain (= 0.5%) is located in the linear viscoelastic region (LVR). The upper limit of LVR, defined as the point with 5% G' loss, was found between 37.9 and 79.2% oscillation amplitude (**Figure 4.3C**). This data ensured that the 0.5% strain for other studies was appropriately chosen. Finally, the frequency sweeps were taken at 0.5% strain with the frequencies ramping up from 0.1 rad/s to 100 rad/s.

Silicon Mold fabrication. Patterned silicon molds were prepared using standard photolithography by the methods modified from Zhang et al (*109*). Briefly, a 3-inch single-side polished silicon wafer (Addison Engineering, Inc.) was spin-coated with a thin layer of adhesion promoter, hexamethyldisilazane (HMDS), at 4000 rpm for 25 sec with a subsequent soft bake at 115˚C for 60 sec. On top of the adhesive layer, SU8-2002 negative photoresist (MicroChem Corp.) was spin-coated at 4000 rpm for 45 sec, followed by a soft bake at 95˚C for 60 sec. The wafer was then exposed to UV (H-line; 75 mJ cm^{-2}; MA/BA6 Mask Aligner, Süss MicroTec AG) with a chrome-patterned photomask of an array of transparent 8-μm circles with a 16 μm pitch (Photo Sciences, Inc.). A post-exposure bake was then applied to the wafers at 95˚C for 60 sec. Next, the baked wafer was developed in SU8 developer for 60 sec and rinsed with isopropyl alcohol to remove un-crosslinked polymers. A final hard bake was performed at 150˚C for at least 15min, which is critical to prevent the damage of the pattern in the following fabrication steps. A patterned silicon master with 8-μm cylindrical pillars was obtained.

PDMS template preparation. The PDMS templates were prepared by soft lithography according to a previously described procedure from Weibel et al (*178*). Briefly, a mixture was prepared by mixing PDMS base and curing agent (weight ratio = 10:1; Sylgard 184 kit), followed by pouring ~20 g of the mixture on top of the silicon mold contained in a 100-mm dish. To remove the bubble within the mixture, PDMS was degassed in a desiccator at RT for ~1 h. Dishes were then transferred to an oven to cure PDMS at 65˚C overnight. After curing, the PDMS mold with an array of 8-μm holes were formed and obtained by cutting the dishes and peeling PDMS from the patterned wafer.

GLAM fabrication. Hydrogel solution was prepared by the aforementioned method. PDMS templates were cut into 1x1 inch quadrants. To increase the hydrophilicity of PDMS for hydrogel deposition, quadrants were then plasma ashed with O_2 for 60 sec (Thierry Corp.). Immediately after plasma treatment, quadrants were spin-coated with 200 μL of the hydrogel

solution per quadrant at 4000 rpm for 90 sec (at a 500 rpm/sec ramp), followed by UV exposure (365 nm; 50 W; Analytik Jena) for 10min. The distance between the hydrogel and UV light source was critical for proper crosslinking. The residual hydrogel outside of the cylindrical holes was then removed by oxygen plasma etching (80 mTorr and 100 W) at 20˚C for 160 sec via the load-locked high plasma density etcher (PlasmaPro 100 Cobra 300; Oxford Instruments). GLAMs were formed within the holes of PDMS templates. Next, the etched samples were placed in a -80˚C freezer for better detachment of GLAMs from the PDMS substrate.

GLAMs were retrieved from PDMS templates by microcontact printing modified from Xia et al (*103*). Poly(vinyl alcohol) (PVA)-coated dishes, the printing substrate, were prepared by coating 2.5 mL of a 3% w/v PVA solution (13–23 kDa), followed by drying PVA in an oven at 65°C overnight. Before printing, the frozen samples were thawed at RT to prevent water condensation on the quadrant surface since the condensation can largely affect the printing yield. The coated side of a PVA dish was held ~2 cm over the beaker filled with DI water of 65°C for ~ 7-10 sec. A GLAM-containing PDMS quadrant was instantly pressed onto the warmed PVA dish. To collect printed GLAMs, 3mL of DI water or phosphate buffered saline (PBS) was added to reach dish with gentle wash twice. The collected solution was filtered through a 20μm cell strainer to remove any large debris, followed by centrifugation at 2000 x g for 2 min to obtain GLAMs.

Stability tests of Gd(III) loading in GLAMs. Two experiments were performed to examine the stability of GLAMs: long-term release of Gd(III) from GLAM and the effect of freeze-thaw process on Gd(III) loading in GLAM. For the release test, after harvesting from PVA dishes, GLAM were collected by centrifugation at 2000 x g for 2 min and were resuspended in BMM- (comprising 500 mL DMEM F12, 50 mL FBS, 5 mL Pen Strep, and 25 mL 200 mM GlutaMAX) at a concentration of $2.0x10^5$ particles/mL. 1 mL of GLAM solution were transferred and sealed in dialysis membrane tubes (MWCO = 3 kDa, SpectraPor). The tubes were then immersed in the vials containing warm BMM- and placed on a plate shaker at 200 rpm in a 37 °C oven. The samples, i.e., BMM- in the vial that contained the released Gd(III), was collected and replaced with fresh DMEM F12 at 1, 2, 4, 8, 24, 48, 168, and 336 h. The collected solutions were stored in -80 °C until future use. On the day of ICP-MS sample preparation, the collected solutions were thawed to RT, followed by transferring 200 μL of the thawed solution into a 15-mL conical tube. 3.8 mL of 2 % (v/v) HNO_3 and 1 mL of internal standard solution (1ng/mL of thulium and indium in 2 % (v/v) HNO_3; High-Purity Standards) was then added to the tube and used ICP-MS analysis. The concentration was determined using a calibration curve made with gadolinium ICP standard solution (High-Purity Standards).

Regarding the freeze-thaw study, the samples were prepared for ICP-MS analysis by the method modified from Marangoni et al (*179*). Briefly, the GLAMs were either freshly collected or harvest and frozen one day prior to ICP-MS sample preparation. Both samples were washed one more time with by PBS by centrifugation at 2000 x g for 2 min, followed by reconstitution in PBS at $4x10^6$ particles/mL. 200 μL of GLAM solutions were mixed with 400 μL of concentrated aqua regia (HNO3:HCl, 1:3) solution for 2 days, followed by an addition of 4.4 mL of 2 % (v/v) HNO_3. 4mL of the resulting solution was further mixed with 4 mL of 2 % (v/v) HNO_3 and 2 mL of internal standard solution (1ng/mL of thulium and indium in 2 % (v/v) HNO_3; High-Purity Standards), and the mixture was then used ICP-MS analysis. The concentration was determined using a calibration curve made with gadolinium ICP standard solution (High-Purity Standards).

Paramagnetic Properties of GLAMs. $Gd(MAA)_3$ and Gadavist® were dissolved in DI water at various concentrations (10, 1, 0.1, 0.01 mg/mL) in 200-µL PCR strip tubes. The T1-weighted MR images and quantitative T1 relaxation times were acquired by the MRI scanner. All T1 relaxation measurements were performed on a 7 T preclinical Bruker BioSpec scanner (Bruker, Billerica, MA). Spin-lattice (T1) relaxation times were measured using a Bruker T1-mapping sequence (TR: [1000, 2000, 3500, 5000, 7000, 9000, 12000] ms; TE: 18 ms; FOV: 5 cm; image size: 200 x 200; slice thickness: 1 mm). Relaxation time constants for each sample were measured by fitting signal decay curves to a standard model in ParaVision 6.0.1, the operating software for the Biospec platform. The relaxivity per Gd(III) can be obtained by calculating the slope of a linear regression of relaxation rate (1/T1) against the Gd concentration. Imaging was taken using T1-weighted MRI (TR: 1500 ms).

GLAMs loaded with high, medium, and low Gd(II) amount were reconstituted in PBS at various concentrations ($15x10^6$, $6.66x10^6$, $2x10^6$, $0.66x10^6$ particles/mL). Gadavist® was diluted by PBS to various concentrations (0.1, 0.01, 0.001 mg/mL). 100 µL of each GLAM and diluted Gadavist® solution was then mixed with 100µL of cold Matrigel by gently pipetting via pre-cold capillary piston pipette tips (Gilson Inc) in 200-µL PCR strip tubes. The resulting solutions were then spinned at 8000 rpm for 5 s to remove the bubble and quickly transferred to metal bath to allow the gelation of Matrigel. For MRI tests, the samples sealed in 200-µL PCR strip tubes were placed in a holder. All T1 relaxation measurements were performed using the parameters described above.

Murine marrow isolation. Progenitor cells were extracted from bone marrow according to previously described methods (*111*). Briefly, BALB/c mice (6–8 weeks old; Charles River Laboratories, Inc.) were euthanized by CO_2 inhalation. The tibias, femurs, and humeri were collected using sterile surgical scissors. Extracted bones were submerged in 70% ethanol, rinsed with PBS, and temporarily store in a separate PBS solution. The bones were transferred to a sterile environment, and epiphyses of each bone were cut. The bone marrow was then flushed out with PBS by a syringe with a 31 G needle into a 50-mL conical tube. Next, the collected solution was passed through a 40-µm cell strainer to remove clots and bone debris, followed by centrifugation at 400 x g for 10 min at 4°C. After removing the supernatant, cells were resuspended in Bambanker (2 mL per mouse equivalent; Lymphotec, Inc.) and stored in cryovials at -80°C.

Porcine marrow isolation. Rib cage was collected from castrated male Yucatan miniature swine (6 months old; Sinclair Bio-Resources) and stored on ice before collecting bone marrow. The surface of rib cage was cleaned with 70% ethanol and dried with sterile wipes before transferred to a sterile environment. Sterile surgical scissors were used to remove the residual meat and separate the sample into individual ribs. The individual ribs were cleaned by 70% ethanol and wipes again and placed on ice. Sterile surgical scissors were used to cut off ~0.5 cm of exposed rib head, followed by removing the costal cartilage from the other end. The rib was then cut into small pieces (~3-4 cm). The bone marrow was then flushed out with bone marrow extraction media (RPMI 1640 with 5mM K2 EDTA) by a syringe with a 21 G needle into a sterile 250-mL bottle. Next, the collected solution was passed through a 40-µm cell strainer to remove clots and bone debris, followed by centrifugation. After removing the supernatant, cells were resuspended in PBS, followed by another centrifugation. After removal of supernatant, the cells were resuspended in 5 mL of ACK lysing buffer for 2 minutes at RT, followed by an addition of 45 mL of PBS and centrifugation. Another PBS wash and centrifugation was then performed. After removing the supernatant, cells were resuspended in

MM- (i.e., 500 mL of RPMI 1640 with 1% Pen Strep and 10% FBS) with 20% DMSO at the concentration of 40 million cells/mL and stored in cryovials at -80°C until needed. All centrifugation steps were performed at 300 x g for 10 min at 4°C

Murine bone marrow-derived macrophages (BMDMs) culture. Murine BMDMs were cultured from bone marrow progenitor cells according to previously described methods (*98*). Briefly, a frozen vial of bone marrow was thawed in metal bath and quickly transferred to a sterile environment when a small ice crystal remained. The cell solution was then gently mixed and added into 8 mL of pre-warmed BMM- (i.e., 500 mL of DMEM F12, 50 mL of FBS, 5 mL of Pen Strep, and 25 mL 200 mM GlutaMAX), followed by centrifugation. After removing the supernatant, cells were resuspended in 1 mL of BMM+ (i.e., BMM- with 20 ng/mL M-CSF) and then counted. Cells were seeded in non-tissue culture (TC) treated T175 flasks containing 25 mL BMM+ at a density of ~$4x10^6$ bone marrow cells per flask, followed by further incubating at 37°C, 5% CO_2. 3 days and 7 days post seeding, 25 mL of additional BMM+ was added to the flask. On day 8, after aspiration of media, cells were washed by PBS and further incubated in 10 mL of cold Accumax (Innovative Cell Technologies) at 37°C for 15 min. Then, the flask was vigorously thumped several times to maximize the detachment of macrophages. Another 10 mL of Accumax was added, and cells were further incubated for 5 min, followed by vigorous thumps. The solution was then collected into a 50 mL conical tube with an equal volume of BMM- and centrifuged. The supernatant was aspirated, and cells are resuspended in BMM+. To prepare for GLAM binding study, murine BMDMs were counted and plated in non-TC-treated 24-well plates at a concentration of $1.5x10^5$ cells/well in a volume of 0.5 mL/well, followed by incubation at 37°C, 5% $CO_2$for 24 h. All centrifugation steps were performed at 400 x g for 10 min at 4°C.

Porcine bone marrow-derived macrophages (BMDMs) culture. Frozen vials of bone marrow were thawed in metal bath and quickly transferred to a sterile environment when a small ice crystal remained. The cell solution was then gently mixed and added into MM- at the volume ratio of 1:5, followed by centrifugation. After removing the supernatant, cells were resuspended in pre-warmed MM+ (i.e., MM- with 20 ng/mL M-CSF) and then counted. Cells were seeded in TC-treated 150-mm plates containing 25 mL MM+ at a density of ~$30x10^6$ bone marrow cells per plate, followed by further incubation at 37°C, 5% CO_2. 6 days post seeding, 20 mL of additional MM+ was added to the plate. On day 12-18, after aspiration of media, 10 mL of PBS was added to the plate and collected in 50-mL conical tubes. 15 mL of cold Accumax (Innovative Cell Technologies) at 37°C for 15-20 min, followed by collecting in 50-mL conical tubes. Further PBS addition and collection was performed twice with vigorously thumps to maximize the macrophage retrieval, followed by centrifugation. Cells in each tube was resuspended in 1 mL of MM- and combined into one single vial with a final centrifugation step. The supernatant was aspirated, and cells are resuspended in MM++ (i.e., MM+ with 20 ng/mL IL4). To prepare for GLAM binding study, porcine BMDMs were counted and plated in TC-treated 24-well plates ($1.5x10^5$ cells/well; 0.5 mL/well), followed by incubation at 37°C, 5% CO_2 for 24 h. To prepare M-GLAMs for porcine studies, porcine BMDMs were counted and plated in TC-treated 100-mm dishes at 37°C, 5% CO_2 for 3 days. All centrifugation steps were performed at 300 x g for 7.5 min at 4°C.

Preparation and characterization of M-GLAM. Frozen GLAM solution was thawed to RT. GLAMs collected by centrifugation at 2000 x g for 2 min and were resuspended in culture media. Concurrently, BMDMs cultured in 24-well plates for 24 h were transferred from the incubator, and the media was slowly aspirated and replaced by fresh culture media. Then, GLAMs were counted and added to each well to achieve different GLAM:MØ ratios (1.5:1,

2.25:1, 3:1) with a final incubation volume of 0.5 mL per well. BMDMs were then incubated with GLAMs at 37°C, 5% CO_2 for 1.5 h without disturbance. After incubation, the supernatant containing unbounded GLAMs was aspirated, and the cells were washed by addition of 0.5mL PBS and aspiration. To harvest M-GLAMs, 0.5mL of Accumax was added to each well and incubate for 15 min at 37°C, 5% CO_2. The plate was removed from a cell culture incubator and gently thumped on the side several times. The solution was collected into 5-mL tubes with equal volume of culture media, followed by centrifugation at 300 x g for 5 min at 4°C.

For adhesion studies, after aspirating supernatant, M-GLAMs were reconstitute in 150 μL of stain buffer (Biolegend) and loaded in a U-bottom 96 well plate. The adhesion was quantified via flow cytometry (Cytek Aurora). For shear studies, after removing supernatant, M-GLAMs were resuspended in 1 mL of media and then loaded in a 1-mL syringe with a 27g blunt needle (McMaster Carr #75165A688, 75165A763). The syringe was fixed on a syringe pump and dispensed with predetermined flow rates to apply various wall shear stresses on M-GLAMs. The theoretical shear stresses were obtained with two assumptions: Cell solution is Newtonian fluid, and the flow in the pipe is laminar flow with a parabolic-shaped velocity distribution in the cross-section view. Thus, at the syringe wall, the shear stress of the fluid is $\tau = -4\mu(Q/\pi R^3)$, where τ is shear stress, μ is dynamic viscosity, Q is volumetric flowrate, and R = radius of the syringe. After experiencing shear forces, M-GLAMs were examined for attachment via flow cytometry (Cytek Aurora). Culture media were BMM- (for murine MØ) or MM- (for porcine MØ).

Cell viability test. The cell viability of GLAM-laden macrophages was evaluated by CellTiter 96® AQueous One Solution Cell Proliferation Assay (MTS assays, Promega, Cat. No. RG3580). The murine BMDMs were cultured in a non-TC 96-well plate ($5x10^3$ cells/well) using BMM+ for 24 h. GLAMs were harvested and collected by centrifugation at 2000 x g for 2 min and were resuspended in BMM+. Then, GLAMs were counted and added to each well to achieve different GLAM:MØ ratios (1.5:1, 3:1, 6:1, 12:1) with a final incubation volume of 0.1 mL per well. BMDMs were then incubated with GLAMs at 37°C, 5% CO_2 for 2 h without disturbance. The solution was aspirated with PBS wash for twice, and the cells were incubated for another 24 h. After incubation, the media was discarded and replaced by 10 μL MTS solution and 90 μL fresh BMM+, followed by incubation for 2.5 h. The solution was transferred to another 96-well transparent ELISA plate and measured the absorption at 490 nm using a microplate reader.

Biodistribution of Gadavist®, GLAMs, and M-GLAMs in mice. Mouse experiments were conducted in accordance with protocols approved by Harvard University's Institutional Animal Care and Use Committee. Healthy female BALB/c mice were intravenously administered with Gadavist® (0.1 mmol/kg), GLAMs ($10x10^6$/mL in saline, 200μL), or M-GLAMs ($6x10^6$/mL in saline, 200μL). Certain timepoints after administration (15min, 1h, and 24h for Gadavist® group; 1h, 4h, 8h and 24h for GLAMs and M-GLAMs group), submandibular blood was collected, and the mice were immediately euthanatized. Next, the major organs (brain, lungs, heart, liver, spleen, and kidneys) were extracted, washed in PBS, and weighted. The organs were then transferred into 14-mL round bottom tubes, and RIPA lysis buffer (EMD Millipore) was added to each organ (1 mL for brain, lung, heart, kidney; 5 mL for liver; 0.5 mL for spleen) prior to homogenization. Also, 0.4 mL of RIPA was added to 0.1 mL of blood samples. The homogenized samples were mixed with concentrated aqua regia solution (HNO3:HCl = 1:3; 0.5 mL for brain, lung, heart, kidney; 2.5 mL for liver; 0.25 mL for spleen; 0.1 mL for blood) for 2 days. The resulting solutions were then diluted by DI water (4.75 mL for brain, lung, heart, kidney; 4 mL for spleen and blood) with no dilution for liver sample, followed by

centrifugation at 1200 x g for 5 min to obtain clear samples without tissue debris. 4 mL of supernatants were slowly transferred to 15-mL conical tubes and subsequently mixed with 1 mL of internal standard solution (1ng/mL of thulium and indium in 2 % (v/v) HNO_3; High-Purity Standards). The mixture was then used ICP-MS analysis, and the concentration was determined using a calibration curve made with gadolinium ICP standard solution (High-Purity Standards).

Porcine mTBI model. Pig experiments were conducted in accordance with protocols approved by Boston Children's Hospital Institutional Animal Care and Use Committee. Six-month-old castrated male Yucatan miniature swine (n = 13) were used for this study. The animals were obtained from Sinclair Bio-Resources (Auxvasse, MO). Animals were randomly assigned to received either a sham procedure (n = 6) or a closed head impact (n = 7, mild TBI). Sham animals were subjected to anesthesia only. The injury procedure was performed as previously described (*180*). Swine were anesthetized with telazol 2.2–6.6 mg/ kg, xylazine 1.1–2.2 mg/kg and atropine 0.04 mg/kg and vital signs (heart rate, respiratory rate, pulse oximetry, and core body temperature) were monitored throughout the procedure. After induction, blood was drawn via the superior vena cava (SVC) and a catheter was placed in the ear of the animal. Anesthetized swine were then placed in a modified Panepinto sling (Morgantown, WV) attached to an impact device. The head of the animal was cradled in a thin membrane parallel to the floor. The impact device was positioned to make impact at a midline site, delineated by the intersection of two lines drawn from the medial aspect of each ear flap to the contralateral medial canthus of the eye – the midline between the nasofrontal and frontal parietal sutures. The impactor device was set at a 35 degree angle (1.5 m height from the head of the swine) and with a 15.9 kg total weight of the impactor arm. These parameters were a priori calculated to deliver a total gforce of ~120 g, in the middle of the range reported in the clinical literature (*181*). Once set in position, the release lever was pressed and injury was delivered, resulting in rotational acceleration of the head through the thin membrane. Animals were allowed to recover in their cages.

MRI and Contrast Administration. Each animal received two MRI scans – a pre-injection scan (without contrast) and a post-injection scan (with contrast) at two days post-injury. The animals were scanned using a 3 T scanner (Skyra; Siemens, Erlangen, Germany) located within the Radiology Department of Boston Children's Hospital. Within the sham and mild TBI conditions, animals were randomly assigned to received either the clinically-available contrast agent Gadavist® (1 mmol/mL, dose of 0.1 mL/kg) (Bayer, Leverkusen, Germany) or M-GLAMs (~75-175 million/10 mL of saline, 10mL per pig) (sham Gadavist®: n = 4, sham M-GLAMs: n = 2, mTBI Gadavist®: n = 4, mTBI M-GLAMs: n = 3). Swine were anesthetized with telazol 2.2–6.6 mg/ kg, xylazine 1.1–2.2 mg/kg and atropine 0.04 mg/kg and vital signs (heart rate, respiratory rate, pulse oximetry, and core body temperature) were monitored throughout the procedure. Once induced, another blood draw was performed via SVC. The animal was transported to the MRI and securely positioned on their back (supine) within the scanner with a 64-channel head and neck coil (Siemens Siemens, Erlangen, Germany). An magnetization-prepared 2 rapid acquisition gradient echo (MP2RAGE) sequence was used with the following parameters: TR = 4000 ms, TI1/TI2 = 700, 2500 ms, $\alpha1/\alpha2$ = 4, 5 degrees, BW = 230Hz/pix, 3x GRAPPA acceleration, acquisition time = 9 min. 1mm isotropic images were acquired with a FOV of 43.6 x 20 cm. This sequence generates images with each of the individual inversion times as well as a T1 map with the same spatial resolution as the other sequences.

Following the pre-injection scans, the animal received the contrast agent. In the case of the animals receiving Gadavist®, the animal began its post-injection scan ~5 minutes after injection, which is comparable to the time delay used clinically. In the case of the animals receiving the M-GLAMs, the animal received its post-injection scan one hour later, allowing the M-GLAMs to traffic into the brain. During this time, the animal's body temperature was maintained using Bair Hugger (3M, Maplewood, MN). The post contrast-injection scans were taken using the same parameters as described above. Following the scans, the animal was returned to its cage to recover.

Euthanasia. Animals were euthanized 6 days after injury (4 days after scan). Swine were anesthetized with telazol 2.2–6.6 mg/kg and xylazine 1.1–2.2 mg/kg and injected with lithium heparin (200 units/kg) intracardially to prevent blood clotting. Animals were then euthanized using intracardial Fatal Plus (110mg/kg) and the brains were immediately removed. Brain tissue was placed in 4% paraformaldehyde upon removal and stored at 4 ˚C for approximately 3 weeks, after which they were placed in phosphate buffered saline (pH = 7.4). Following brain removal, the ribs were collected and placed on ice for macrophage collection. The heart, lung, liver, kidney, and spleen were all also dissected and placed in 4% paraformaldehyde and stored at 4 ˚C for approximately 3 weeks, after which they were placed in phosphate buffered saline (pH = 7.4).

MRI data analysis. The subtracted T1-relaxivity maps (i.e., post-scans subtracted by pre-scans) were obtained by first doing a registration to align the pre- and post-scans via ITK-SNAP, followed by subtraction via convert3D of ITK-SNAP. For registration, the post-scans were loaded as the main image, and the pre-scans were loaded as the additional image into ITK-SANP. The registration was then performed by doing manual alignment, auto alignment (rigid, mutual, 4x + 2x), and last manual alignment to check the quality of registration. The registered scans were then linearly resliced and converted from the Digital Imaging and Communications in Medicine (DICOM) format to the Neuroimaging Informatics Technology Initiative (NIfTI) format, followed by being subtracted via convert3D.
For quantitative imaging analysis, the resliced post-scans in NIfTI format were loaded in ORS-Dragonfly®. Regions of interest (ROI; i.e., ChP and LV) and cerebral background were identified and manually segmented using ROI Painter Tools of ORS-Dragonfly®. The mean and standard deviation (STD) of the pixel intensities in the selected segments were reported via the Histogram tool of ORS-Dragonfly®. The mean signal intensities of muscle were obtained by the probe function of ORS-Dragonfly® with a probe size of 6.85 mm (37 pixels).

Relative mean intensity of ROI to muscle based on the post-scans was obtained by $Mean_{ROI}$ / $Mean_{muscle}$**.** Relative mean intensity changes of ROI to cerebral background based on the post-scans, calculated by ($Mean_{ROI}$ – $Mean_{background}$) / $Mean_{background}$**.** The percentage of MRI signal enhancement in the ROI of mTBI pigs over sham pigs were calculated as - [(A ± dA) - (B ± dB)]/(B ± dB)], where A = $Mean_{ROI}$ of mTBI pigs, dA = STD_{ROI} of mTBI pigs, B = $Mean_{ROI}$ of sham pigs, dB = STD_{ROI} of sham pigs, and the errors were propagated using statistical error propagation analysis (*182*). SNR was calculated by $Mean_{ROI}$ / $STD_{background}$, and CNR was acquired by ($Mean_{ROI}$ – $Mean_{background}$) / $STD_{background}$. Coefficient of variations of ROI and background were calculated by STD_{ROI} / $Mean_{ROI}$ and $STD_{background}$ / $Mean_{background}$, respectively.

Statistical analysis. All the experiments were conducted with at least three replicates. All statistical analyses were represented as mean ± standard error using GraphPad Prism 8 software. To determine statistical significance, unpaired student's t test and one-way or two-way

ANOVA with Tukey's HSD (honestly significant difference) test were applied, as applicable. Significance was determined at the following cutoff points (ns = $P > 0.05$; * = $P \leq 0.05$; ** = $P \leq 0.01$; ***. $P \leq 0.001$).

4.3 Results

4.3.1 Design and fabrication of Gd(III)-loaded anisotropic micropatches (GLAMs)

T1 MRI signals arising from the Gd(III)-based contrast agent necessitates close water proton-Gd(III) interactions. Hence, a hydrogel-based material was chosen as the foundation of GLAM to encapsulate Gd(III) and provide a water-rich internal microenvironment. Further, hyaluronic acid was selected as the material of choice due to its well-known biocompatibility and interactions with cells via CD44 (*183*). To achieve stable loading of Gd(III) into the hydrogel network, a gadolinium methacrylic acid ($Gd(MAA)_3$) precursor was synthesized and reacted with AlexaFlour 555-labeled methacrylated hyaluronic acid (HAMA) and poly(ethylene glycol) dimethacrylate (PEGDMA) using the photo-initiated free radical polymerization reaction (**Figure 4.2**). The fabrication method of Gd(III)-loaded hydrogels was first validated as a bulk material. A series of rheological tests, including oscillatory time-sweep, amplitude-sweep, and frequency-sweep experiments, using a rheometer with a UV curing accessory confirmed the formation of hydrogels (**Figure 4.3)**. The onset of gelation occurred at 7 sec after UV exposure as indicated by the crossover of loss modulus and storage modulus ($G' = G''$) (**Figure 4.3A**) (*184*). The storage modulus G' reached the plateau after 2 minutes of UV exposure, suggesting the completion of crosslinking. Formation of stable and covalently crosslinked hydrogel network was further confirmed through the frequency-sweep test (*185*). A frequency-independent G' and G'' was observed **(Figure 4.3B)**, and the averaged storage modulus reached 10.25 ± 0.58 kPa, confirming the formation of a relatively strong gel.

Transferring the bulk Gd(III) hydrogel chemistry to the microscale to fabricate GLAMs is a significant technical challenge. Specifically, the discoidal structure of GLAM is a key feature since disc-shaped particles have been demonstrated to adhere to macrophages without internalization (*186*). However, preparing anisotropic micron-sized hydrogel disks with dimensions smaller than the cell is a challenging task. Two techniques have been previously used to fabricate anisotropic subcell-sized microparticles at scale: particle replication in non-wetting templates (PRINT) (*187*) and discontinuous dewetting in a degassed mold (*188*). Neither of these methods, however, has been employed for biopolymers with a high molecular weight and viscosities (*189*). Hence, a new methodology was engineered to fabricate disk-shaped micropatches comprising Gd(III)-loaded hyaluronic acid.

A PDMS template was first prepared using soft lithography (*190*) (**Figure 4.4A**) which was then employed to form GLAMs using imprint lithography (*191*) and reactive ion etching (*192*) (**Figure 4.4B**). Plasma treatment was used to increase surface energy of the PDMS template, leading to a greater hydrophilicity to enable hydrogel deposition (*193*). PDMS templates with 8-mm hole array were spin-coated with Gd(III) hydrogel precursors and crosslinked by UV exposure. An interconnecting hydrogel film is inherently formed during spin-coating due to the high surface energy of PDMS (*194*), preventing the formation of individual GLAMs (**Figure 4.4C (i)**). Therefore, inductively coupled plasma - reactive ion etching via oxygen was applied to remove this embossed film. GLAMs were then printed on a PVA-coated surface. High efficiency of the printing process was achieved by freezing of the PDMS template post-UV exposure at -80˚C overnight. This freezing step led to a 16-fold improvement in the efficiency of printing (**Figure 4.5A**), likely due to the differential thermal-expansion

coefficient of PDMS and hydrogel that enhanced separation of GLAMs from the template (*195*). Printed GLAMs were collected in PBS and purified via centrifugation. The final collected GLAMs were imaged by fluorescence microscopy, showing a suspension of GLAMs with a discoidal shape (**Figure 4.4C (ii)**). Loading and stability of Gd(III) in GLAMs were quantified using inductively coupled plasma mass spectrometry (ICP-MS). Negligible (< 0.7%) free Gd(III) was detected in GLAMs. Moreover, the loading remained stable for at least 2 weeks (**Figure 4.5B**). Long-term storage of GLAMs under frozen conditions did not adversely impact the loading (**Figure 4.5C**).

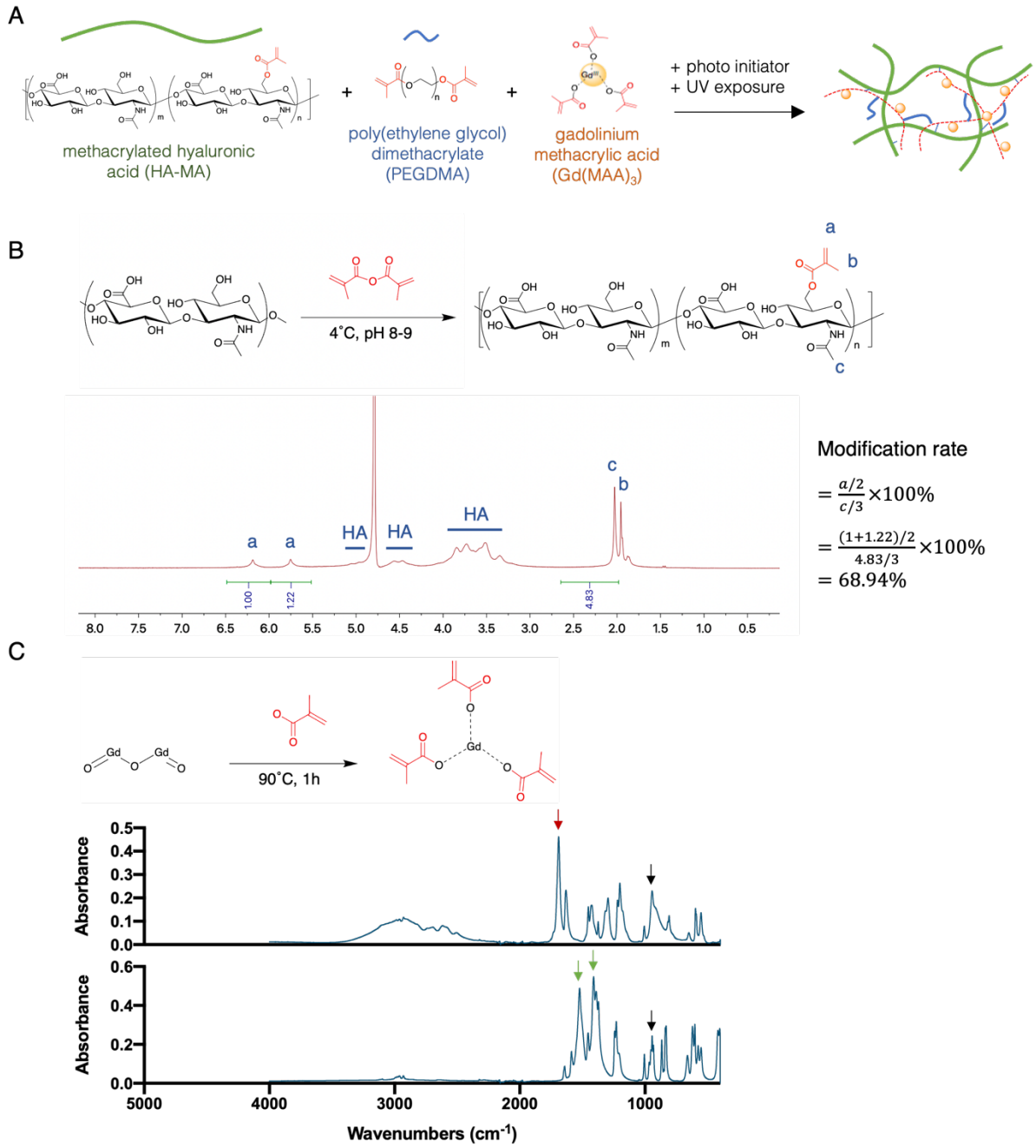

Figure 4.2: Design and characterization of hydrogel precursors for Gd(III)-loaded anisotropic micropatches (GLAMs). (A) The main components of GLAMs includes methacrylated hyaluronic acid (HAMA), poly(ethylene glycol) dimethacrylate (PEGDMA), and gadolinium methacrylic acid ($Gd(MAA)_3$). A hydrogel network can be formed by

photopolymerization upon the addition of Irgacure 2959 photoinitiator and exposure of the ultraviolet (UV) light. (B) Schematic illustration of chemical synthesis of HAMA and its NMR spectrum. The successful conjugation was validated by ^{1}H NMR with a modification efficiency of 68.94% (C) Schematic illustration of chemical synthesis of $Gd(MAA)_3$ and the FTIR spectrum of gadolinium oxide (Gd_2O_3, top) and $Gd(MAA)_3$ (bottom). The successful formation of $Gd(MAA)_3$ was verified by the FTIR spectra, where the bands corresponding to the non-ionized carboxyl groups of MAA disappeared (red arrow) and the bands associated with the coordination between gadolinium and carboxyl groups appeared (green arrows) after synthesis. In addition, the bands of reactive alkene on methacrylic acid were present in both MAA and $Gd(MAA)_3$ spectra (black arrow), indicating the photopolymerization capacity was not affected after complex formation.

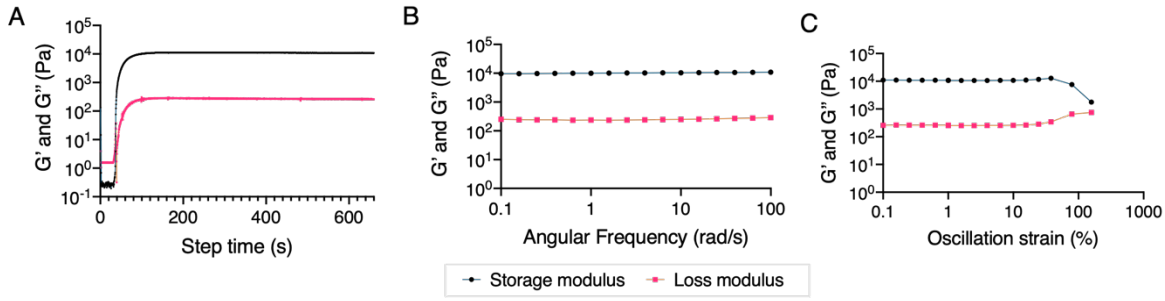

Figure 4.3: Dynamic oscillatory rheological characterization of the hydrogel. Time sweeps (A), frequency sweeps (B), and amplitude sweeps (C) were applied. Storage modulus (G') and loss modulus (G") were recorded in each test. The UV light was then applied at 30 sec. At 7 sec post UV exposure, the gelation starts as G' = G", corresponding to the gel point of the hydrogel. This also signified the fast kinetics of radical polymerization. Beyond the crossover point, G' > G" denoted the transition of the hydrogel from liquid (viscous) to solid phase (elastic) (*184*). In addition, G' reached the plateau of 10.98 kPa at 136.65 sec.

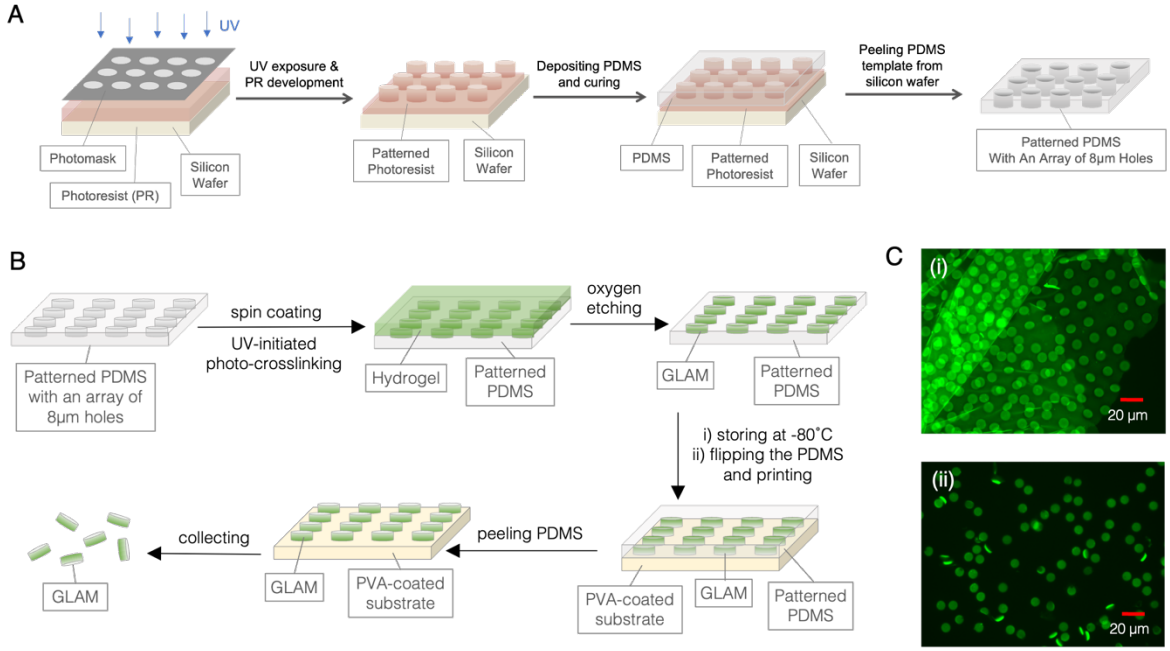

Figure 4.4: Fabrication of GLAMs. The GLAM preparation includes two parts: *PDMS template fabrication* (A) and *backpack formation, refinement, and collection* (B). The silicon wafer spin-coated with the negative photoresist was exposed to UV under a mask with an array

of circles (8 µm in diameters). The photoresist was then developed, and a patterned silicon master with cylindrical pillars was obtained. A PDMS template with an array of 8-µm holes was produced by pouring PDMS solution on a patterned silicon master, followed by curing PDMS at 65˚C overnight and peeling the cured template from silicon wafers. Next, PDMS templates were spin-coated with Gd(III) hydrogel precursors and crosslinked by UV exposure. The residual hydrogel outside of the cylindrical holes was subsequently removed via oxygen plasma etching. The PDMS template post-etching was frozen at -80˚C overnight for better detachment. Finally, GLAMs were printed on a PVA-coated surface, followed by collecting GLAMs in an aqueous solution and purifying via centrifugation. (C) Fluorescence microscopy images of GLAMs without (i) and with the oxygen etching step (ii) in PBS.

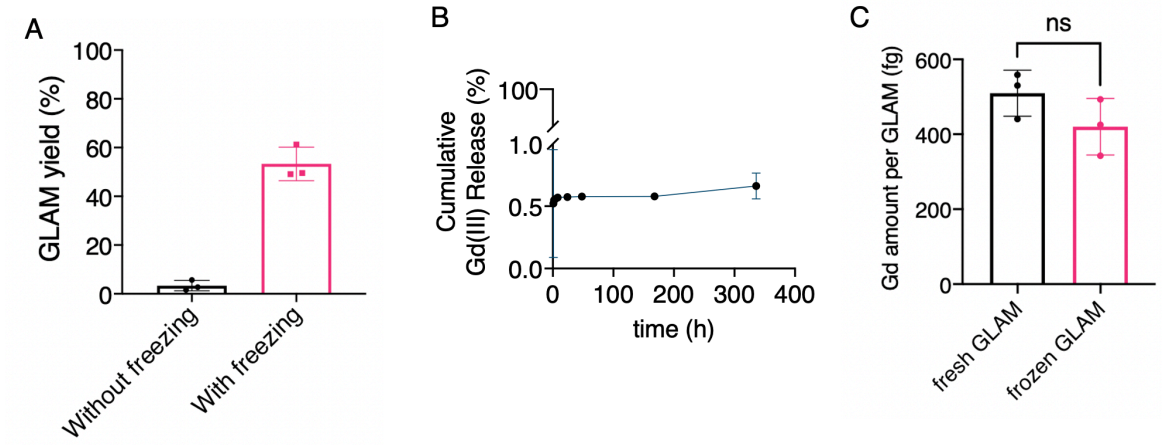

Figure 4.5: Characterization and stability of GLAMs. (A) GLAM yields with or without freezing step. After incorporating freezing step into the fabrication process, the yield of GLAMs increased from 3.33 % to 53.29% (n=3). (B) Cumulative release of Gd(III) from the GLAMs over 14 days in cell culture media (n=3). (C) The Gd(III) amount per freshly prepared GLAM or GLAMs experienced the freeze-thaw process. Data were analyzed using unpaired t-test.; ns, not significant.

4.3.2 Paramagnetic properties of $Gd(MAA)_3$ and GLAMs

Relaxivities of $Gd(MAA)_3$ and GLAMs were assessed using a 7T MRI scanner with a longitudinal T1 mapping sequence. A clinical standard MRI contrast agent - Gadavist® was employed as a comparator (**Figure 4.6A**). Both Gadavist® and free $Gd(MAA)_3$, the precursor of GLAM, demonstrated a Gd(III) concentration-dependent T1 contrast (**Figure 4.6B**). A concentration-dependent quenching effect was seen for Gadavist® and $Gd(MAA)_3$, where the T1 signal peaked and decreased with further increase in Gd(III) concentration, a phenomenon arising likely from the dominance of the T2 effects at a high gadolinium concentration (*196, 197*). Prior to the saturation threshold, the relaxivity of $Gd(MAA)_3$ (9.95 $mM^{-1}s^{-1}$) was markedly higher than that of Gadavist® (3.63 $mM^{-1}s^{-1}$) (**Figure 4.6C; Figure 4.7, A&B**), demonstrating the potential of $Gd(MAA)_3$ in itself as an effective T1 contrast agent.

GLAMs also exhibited a concentration-dependent relaxivity (**Figure 4.6D**). The relaxivity per Gd(III) in GLAMs increased when the payload increased from low $Gd(MAA)_3$ loading to medium loading (25.14 to 34.69 $mM^{-1}s^{-1}$), while it dropped in the case of high $Gd(MAA)_3$ loading (26.09 $mM^{-1}s^{-1}$). Still, the relaxivity per Gd(III) was 8-11 fold higher in GLAM compared to that in Gadavist® (**Figure 4.6E; Figure 4.7, C-F**). High relaxivity of Gd(III) in the particulate form compared to the free form has been previously reported in the literature

(*198, 199*). The enhancement of relaxivity of Gd(III) in GLAMs compared to Gadavist® can be contributed to the reduced mobility of Gd(III) in the hydrogel, thus reducing the orientational freedom within the particle and the increase in the rotational correlation time (*200-202*). Relaxivity per GLAM particle, calculated by multiplying the amount of Gd(III) ions per GLAM with the relaxivity per Gd(III), exhibited a monotonic correlation with $Gd(MAA)_3$ loading (**Figure 4.6F**). Therefore, GLAMs with high $Gd(MAA)_3$ loading were chosen for future studies.

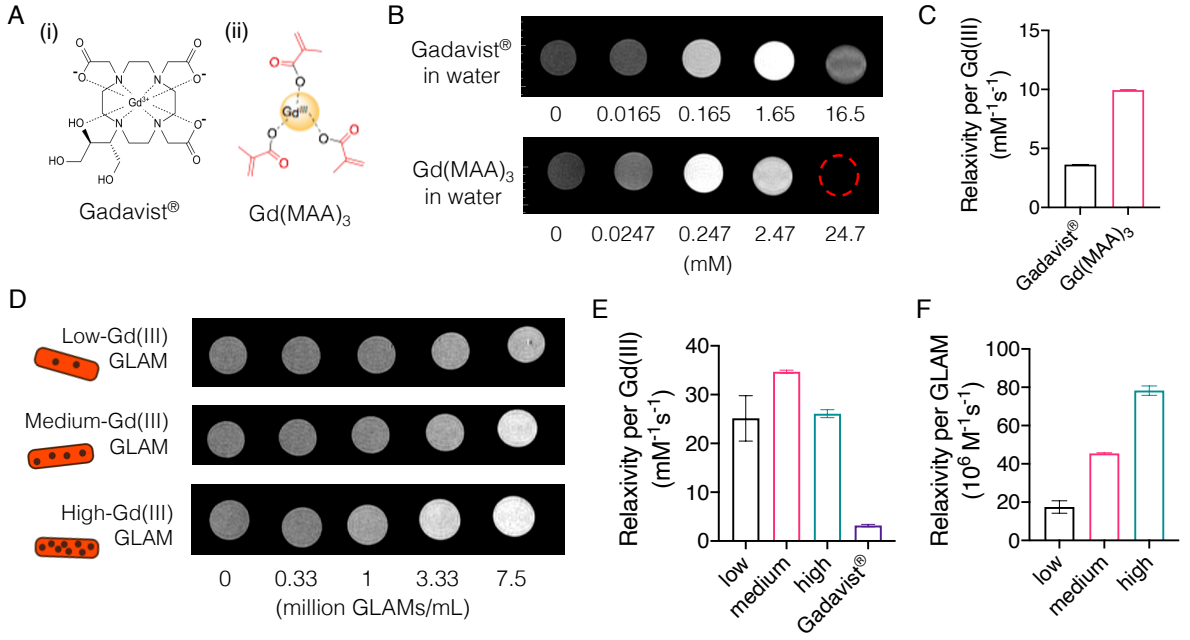

Figure 4.6: Paramagnetic properties of Gadavist®, $Gd(MAA)_3$ and GLAMs. (A) The T1-weight MR images of small molecule contrast agents: Gadavist®, $Gd(MAA)_3$ dissolved in DI water at various concentrations at 7T. (B) The plot of T1 (longitudinal) relaxation rate versus Gd(III) concentration at 7T for Gadavist® (i) and $Gd(MAA)_3$ (ii). (C) The T1-weight MR images (top) and T1 relaxation rate plot (bottom) of GLAMs suspended in the Matrigel at various particle concentrations 7 T. GLAMs are loaded with different amount of Gd(III) from low (i), medium (ii), to high (iii). (iv) Gadavist® in the Matrigel were also examined.

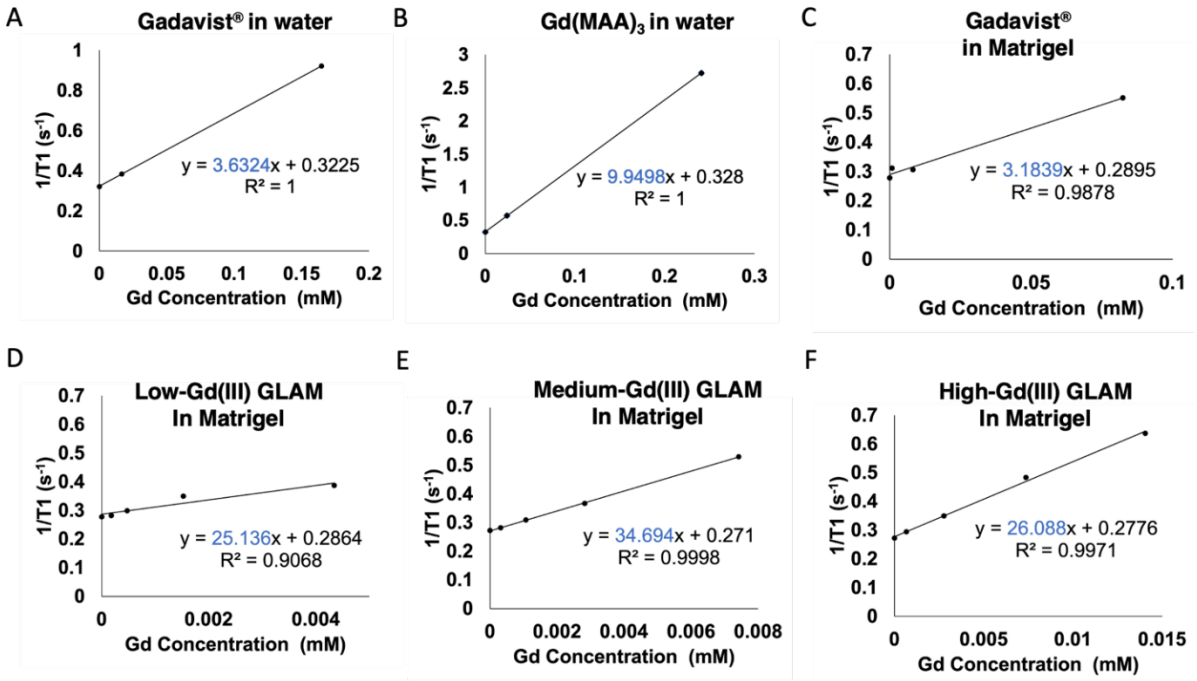

Figure 4.7: The plots of T1 (longitudinal) relaxation rate versus Gd(III) concentration at 7 T of various contrast agents. Gadavist® (A) and $Gd(MAA)_3$ (B) were dissolved at different concentrations in DI water in 0.2 mL strip tubes. (C) Gadavist® at different concentrations were dissolved in Matrigel. GLAMs loaded with different amount of Gd(III) from low (D), medium (E), to high (F) were resuspended in Matrigel at various particle concentrations. The relativity of Gd(III) in each system was obtained by the slope of the T1 relaxation rate plot (highlighted in blue).

4.3.3 M-GLAM preparation and characterization

GLAMs exhibited high adhesion to macrophages (M-GLAMs), as confirmed by fluorescence microscopy (**Figure 4.8A**). The efficiency of GLAM adhesion to murine macrophages (MØ) increased with increasing GLAM:MØ ratios. Specifically, as the GLAM:MØ ratio increased from 1.5:1 to 3:1, the adhesion efficiency increased from 51% to 72% (**Figure 4.8B**). Comparable efficiencies were also seen in porcine macrophages, thus confirming that GLAM adhesion to macrophages was species-independent (**Figure 4.8C**). GLAMs did not induce toxicity to macrophages, as assessed by their viability (**Figure 4.8D**). Macrophage viability remained at approximately 100% throughout all the tested ratios. GLAMs remained adhered to MØ under physiological shear stresses (0-20 Pa) (**Figure 4.8E**). Previously frozen GLAMs exhibited higher adhesion compared to freshly collected GLAMs (**Figure 4.8F**), indicating the freeze-thaw step did not adversely affect MØ binding.

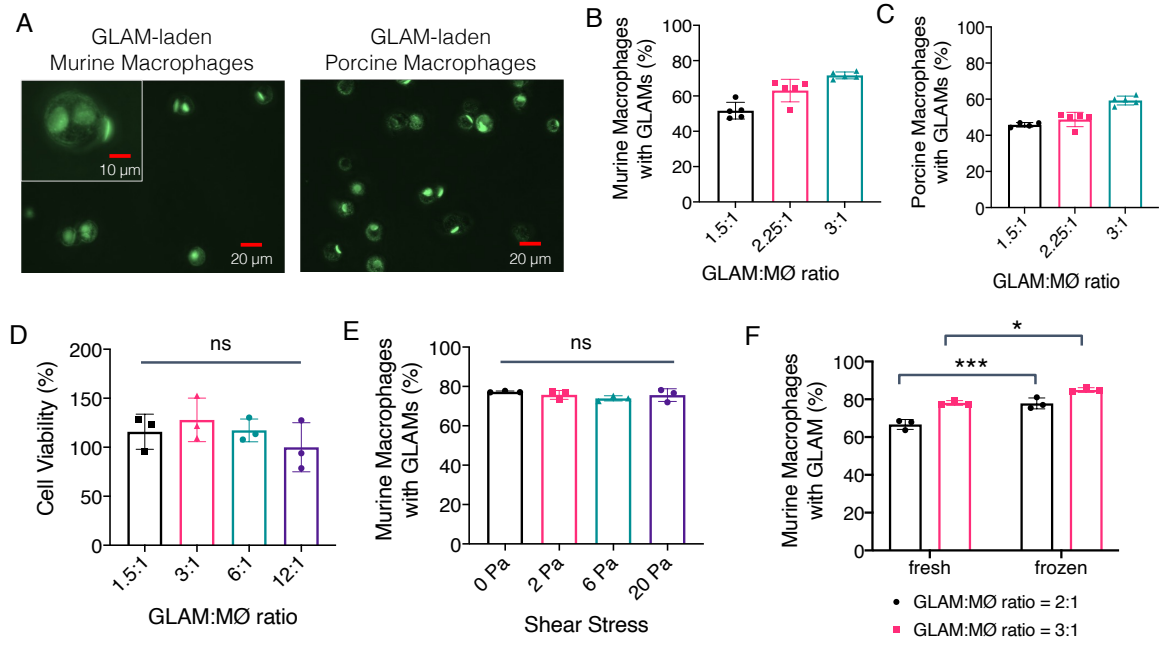

Figure 4.8: Characterization of M-GLAM and its stability. (A) Fluorescence microscopy images of GLAM-laden murine (left) or porcine macrophages (right). Association of GLAMs with primary murine (B) and porcine macrophages (C) at various GLAM to macrophages (GLAM:MØ) ratios in vitro ($n \geq 4$). (D) Effect of GLAMs on the cell viability by MTS assays at various GLAM:MØ ratios in vitro ($n = 3$). (E) Effect of shear stresses on adhesion efficiency ($n = 3$). (F) Effect of freeze-thaw process on adhesion efficiency ($n = 3$). Freshly prepared GLAMs (fresh) or GLAMs that underwent freeze-thaw process (frozen) were tested. For D & E, data were analyzed by one-way ANOVA with Tukey's HSD test; ns, not significant. For F, data were analyzed by two-way ANOVA with Tukey's HSD test. *$P < 0.05$; *** $P<0.001$.

4.3.4 Biocompatibility of GLAMs and M-GLAMs

Biocompatibility and biodistribution of GLAMs and M-GLAMs were assessed in mice with a particular focus on comparison to a clinically available GBCA - Gadavist®. GBCA accumulation in the kidneys is known to elevate the risk of systematic kidney fibrosis in patients with existing renal diseases and is contra-indicated in these patients (*203, 204*). Injections of Gadavist®, GLAMs and M-GLAMs were well tolerated by mice. Gadavist® exhibited significant renal accumulation in mice at 15 min post injection (**Figure 4.9A**). GLAMs, on the other hand, were mainly distributed in the lung, followed by liver and spleen, and barely accumulated in the kidney (**Figure 4.9B**). M-GLAMs exhibited a similar gadolinium accumulation pattern with GLAMs (**Figure 4.9C**). Negligible renal accumulation of GLAMs and M-GLAMs revealed that the gadolinium was stably conjugated in particles without leakage. Only about 8%, 0.3%, 0.0027% of Gadavist® were detected in all the collected organs at 15 min, 1h, and 24h post injection, respectively (**Figure 4.10**), suggesting that Gadavist® was rapidly cleared and almost completely excreted from the body within 24 hours. In contrast, GLAMs and M-GLAMs demonstrated stable retention in the vital organs (~ 80%) over a period of 24 hours, showing the potential feasibility of employing M-GLAMs for long-term disease monitoring. Note that while M-GLAMs remained in the body for an extended time, the delivered Gd(III) dose from M-GLAMs was ~580-times lower than that from Gadavist® (2 µmole/mouse for Gadavist® and 3.4 nmole/mouse for M-GLAMs), thus keeping body's exposure to Gd(III) to very low levels.

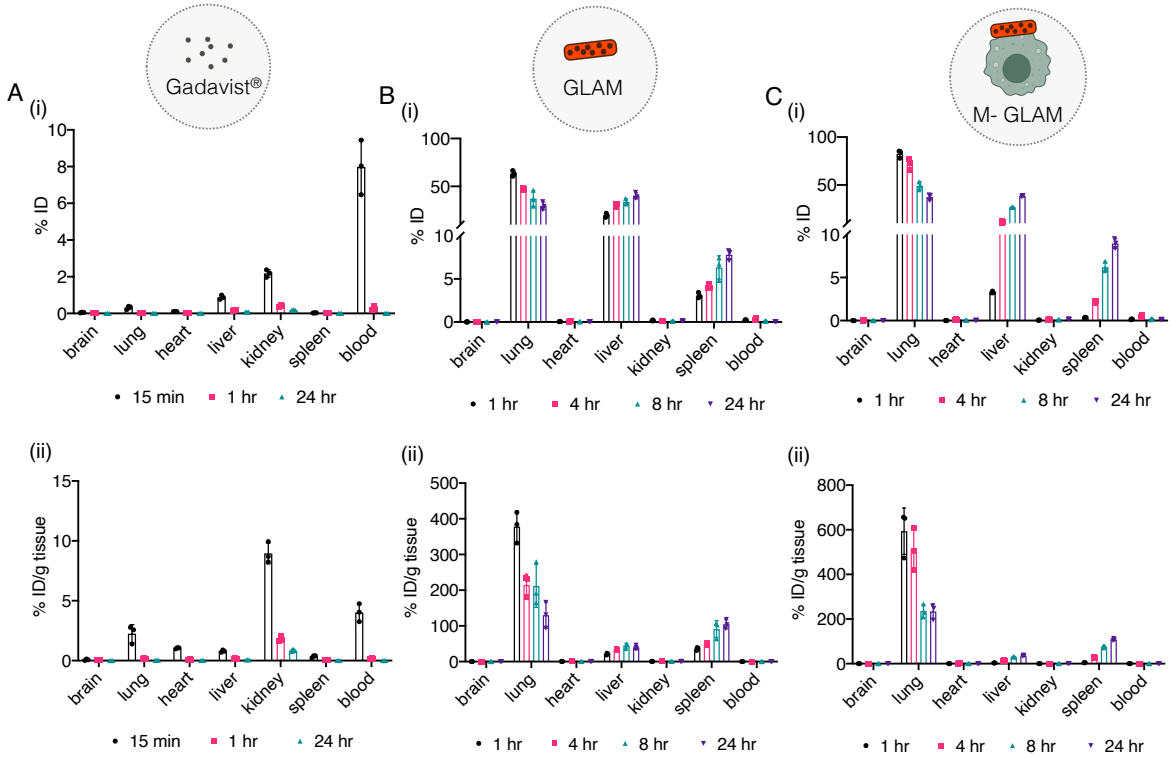

Figure 4.9: In vivo biodistribution study of different contrast systems in healthy BALB/c mice. Mice were injected with Gadavist® (A), GLAMs (B), and M-GLAM (C). For Gadavist® group, mice were sacrificed at 15min, 1h, and 24h post injection (n = 3), while the GLAM and M-GLAM administered mice were sacrificed at 1h, 4h, 8h and 24h post injection (n = 3). After that, the organs were immediately collected and processed for quantifying Gd(III) amount in each organ via ICP-MS. Both percent of injected dose (% ID) and percent of injected dose per gram of tissue (% ID/g) were presented.

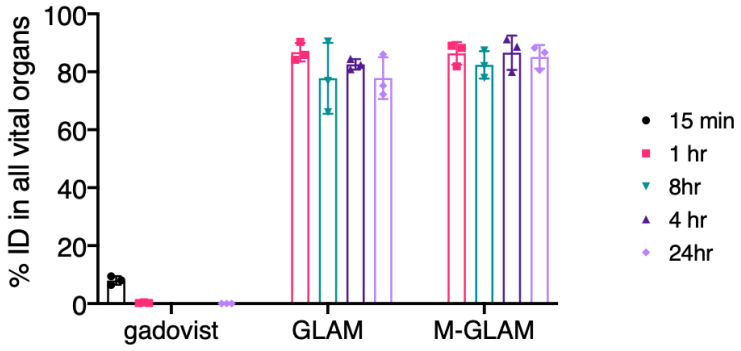

Figure 4.10: The sum of injected dosage of each contrast system in all vital organs at various time points (n = 3). Organs included brain, lung, heart, liver, kidney, and spleen.

4.3.5 Evaluation of M-GLAMs for mTBI diagnosis in the porcine model

The utility of M-GLAMs in diagnosing mTBI was assessed in a porcine model. The model was chosen due to the compositional, structural, anatomical, and biomechanical similarity under trauma between porcine and human brains (*205, 206*). Synthesis of GLAMs was scaled to provide a sufficient dose in pigs. Gadavist® and M-GLAM were administered in sham and mild

TBI pigs, and high-resolution T1 maps were acquired by a 3T MRI scanner. Gadavist® (0.1 mmol /kg; ~2.2-2.8 mmole/animal) or M-GLAMs (~75-175 million/animal) were successfully delivered in sham and mTBI animals. Gadavist® dose was selected to match a typical clinical recommendation so as to serve as a clinical comparator. M-GLAM dose was selected to maintain the dose of injected macrophages to a level comparable to previously reported values for adoptive macrophage therapies in the clinic (*22*). Mild facial edema and/or hives was observed on the injection side of the pig in three out of five pigs administered with M-GLAMs. Red rash was shown in one out of eight pigs administered with Gadavist®. However, all symptoms and changes were transient and self-resolved during the recovery time of pigs from anesthesia. To assess the potential of ChP as a region of interest (ROI) for mTBI, images were analyzed based on subtracted T1-relaxivity maps (i.e., post-scans subtracted by pre-scans) using ITK-SNAP (*207*).

Gadavist®, as a small molecule, distributed throughout the brain and clearly delineated the brain structure (**Figure 4.11A**). However, no discernable differences were noted between the sham and mild TBI pigs. Subtracted T1 maps of the pigs with M-GLAM injection were overall dimmer compared to those with Gadavist® administration, at least in part due the fact that the Gd(III) dose in M-GLAMs was 500-1000-fold lower than that in the case of Gadavist®. However, a significant difference was observed in the ChP and lateral ventricle (LV) between sham and mTBI pigs in case of M-GLAMs (dashed rectangles; **Figure 4.11A**). Current clinical neuroimaging for TBI diagnosis usually focuses on finding the bloody lesions associated with the blood-brain barrier (BBB) in the brain parenchyma owing to the lack of other apparent differences (*208*), M-GLAMs, on the other hand, open a new potential region of interest (ROI) in the vicinity of the BCSF barrier for mTBI diagnosis.

To assess the ability of ChP to serve as a clinically usable ROI for mTBI, in the absence of the availability of pre-trauma scans, as often is the case, only post-scans were used to define the MRI signals in the ROI and its surrounding cerebral background by extracting the pixels of both areas via ORS-Dragonfly® (**Figure 4.11B**). The mean intensity in the ROI ($\bar{I}_{ROI}$) was significantly different between the sham and mTBI pigs administered with M-GLAMs, whereas no difference was seen in case of Gadavist® (**Figure 4.11C**). Further, given that MRI automatically adjusts to prevent the saturation of the signals, we aimed to mitigate this bias through normalizing $\bar{I}_{ROI}$ by the average muscle mean intensity ($\bar{I}_{muscle}$). Normalized intensity ($\bar{I}_{ROI}/\bar{I}_{muscle}$) exhibited a significant difference in sham and mTBI pig brains for the M-GLAM group, but not for the Gadavist® group (**Figure 4.11D**).

Enhancement of the mean ROI intensity ($\bar{I}_{ROI}$) compared to that in the surrounding background tissue (cerebral parenchyma, $\bar{I}_{background}$) offers another means to assess mTBI. In the M-GLAM group, the normalized intensity ($\left[\bar{I}_{ROI} - \bar{I}_{background}\right]/\bar{I}_{background}$) increased from 16.9% in sham pigs to 28.08% in mTBI pigs (**Figure 4.11E**, $p < 0.05$). In contrast, no difference was observed in the sham and mTBI pigs when injected with Gadavist® (22.33% in sham vs. 25.85% in mTBI, $p = 0.6$). The signal-to-noise ratio (SNR, $\bar{I}_{ROI}/\Delta_{background}$), contrast-to-noise ratio (CNR, $\left[\bar{I}_{ROI} - \bar{I}_{background}\right]/\Delta_{background}$), and the coefficient of variation for ROI and background (CoV, $\Delta_{ROI}/\bar{I}_{ROI}$ and $\Delta_{background}/\bar{I}_{background}$) were also obtained (**Figure 4.11, F&G; Figure 4.12**), where Δ is standard deviation of the signal. Both SNR and CNR were significantly different between sham and mTBI pigs only in the case of M-GLAMs, but not in the case of Gadavist®, with a particularly striking difference observed in the case of CNR (**Figure 4.11G**). A lower CoV of ROI in the M-GLAM groups over Gadavist® implied the M-GLAMs provides a more uniform MRI signals in the ROI (**Figure 4.12**).

Tolerance of M-GLAMs and Gadavist® was assessed by histopathology (**Figure 4.13**). Vital organs were harvested, fixed, sectioned, and stained with H&E for histological analysis at 4 days post-injection. No significant histological abnormality was seen in the organs of either Gadavist® or M-GLAM-injected animals, as assessed by an independent board-certified veterinary pathologist. Some insignificant changes, observed in liver, lung, and kidney of both groups, were attributed to the euthanasia and fixation procedures.

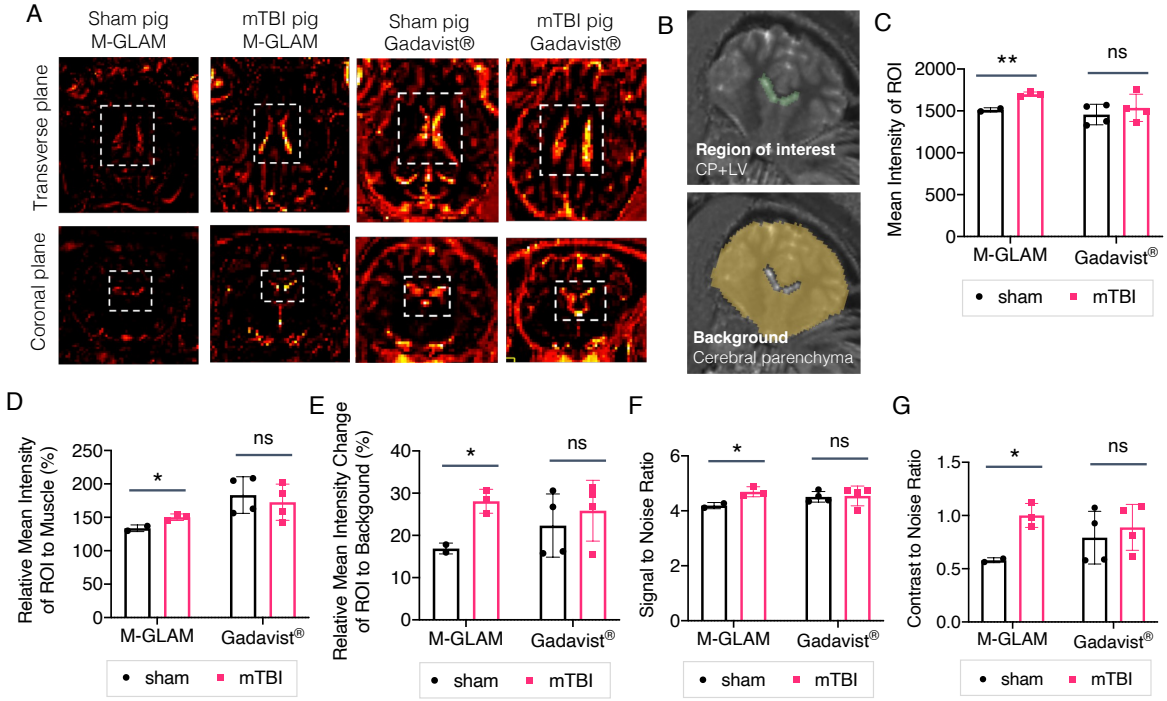

Figure 4.11: MRI studies for mild TBI diagnosis in the porcine model. (A) Representative subtracted T1-relaxivity maps of the pigs injected with M-GLAM and Gadavist®. T1 maps were acquired before (pre-scans) and after administration of imaging agents (post-scans). Subtracted images were then obtained by registering both scans via ITK-SNAP, followed by subtracting post-scans with pre-scans via convert3D of ITK-SNAP. Dotted square indicates the lateral ventricle (LV) and choroid plexus (ChP), which is the region of interest (ROI). (B) Representative post-scans of MRI-generated T1 maps painted with ROI (top) and background (bottom) via ORS-Dragonfly®. (C) Quantitative analysis of MR signal intensities in the ROI of sham injected with M-GLAM (n = 2) or Gadavist® (n = 4) as well as mTBI pigs injected with M-GLAM (n = 3) or Gadavist® (n = 4) by the mean pixel intensity ($\bar{I}_{ROI}$). Post-scans were used. (D) Relative mean intensity of ROI to muscle based on the post-scans, obtained by $\bar{I}_{ROI}/\bar{I}_{muscle}$. (E) Relative mean intensity changes of ROI to cerebral background based on the post-scans, calculated by $(\bar{I}_{ROI} - \bar{I}_{background})/\bar{I}_{background}$. Signal-to-noise ratio (SNR) (F) and contrast-to-noise ratio (CNR) (G) of the post-scans. SNR was calculated by $\bar{I}_{ROI}/\Delta_{background}$, and CNR was acquired by $(\bar{I}_{ROI} - \bar{I}_{background})/\Delta_{background}$. Δ, standard deviation. For C to G, data were analyzed using unpaired t-test.; ns, not significant, *P<0.05, **P<0.01.

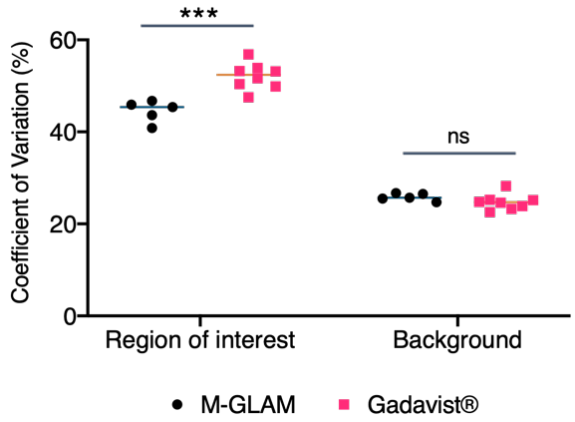

Figure 4.12: Coefficient of variation of ROI and cerebral background in the post-scans of the pigs injected with M-GLAM and Gadavist®. Coefficient of variations of ROI and background were calculated by $\Delta_{ROI}/\bar{I}_{ROI}$ and $\Delta_{background}/\bar{I}_{background}$, respectively. Data were analyzed using unpaired t-test.; ns, not significant, ***P<0.001.

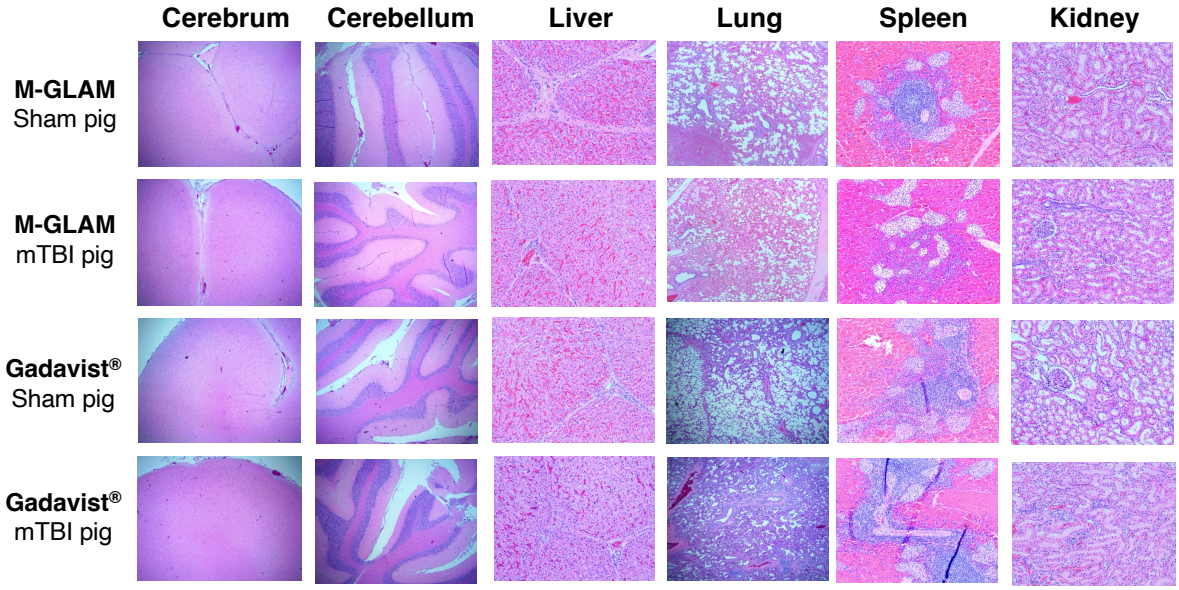

Figure 4.13: Evaluation of the toxicity of M-GLAM and Gadavist® in vivo. Histological data (H&E staining) obtained in the major organs (cerebrum, cerebellum, liver, spleen, lung, and kidney) of the mice 4 days after injection under various conditions. Images were taken at 2x for cerebrum, cerebellum, lung, and kidney, and at 10x for liver and spleen. No significant histological abnormality was seen in the organs of either Gadavist® or M-GLAM-injected animals. Some insignificant changes were observed: The pigs were not exsanguinated before organ collection, thus erythrocytes within normal limits were shown in the liver tissues of all groups; The minor edema and erythrocyte presentation in the lung were mainly due to the suboptimal fixation and the effect of euthanasia drugs; Minor autolysis and wider lumens in tubules of the kidney tissues mainly attributed to the fixation.

4.4 Discussion

M-GLAMs, macrophage-hitchhiking **G**d(III)-**L**oaded **A**nisotropic **M**icropatches, provide a novel means of using immune cells for diagnosing mTBI. GLAMs were prepared using a new fabrication process to build hydrogels into discoidal microparticles. To our knowledge, this is

the first demonstration of fabrication of anisotropic hyaluronic acid-based microparticles of these dimensions at scale. The results presented here demonstrate that Gd(III) can be incorporated into GLAMs with at least an 8-fold enhancement in relaxivity. More importantly, the GLAMs were stable upon the freeze-thaw process which is critical in improving the particle yield and essential for long-term shortage. Of note, GLAMs are made of materials (i.e., hyaluronic acid and polyethylene glycol), which have been widely used in FDA-approved products (*209, 210*).

M-GLAMs were prepared by incubating GLAMs with allogeneic macrophages. Stable binding of GLAMs to the macrophage surface results from the balance between the factors that promote and impede phagocytosis. Macrophages, body's professional phagocytes, are highly effective in binding, engulfing, and eliminating particulates with dimensions larger than 0.5 μm (*211*). They are capable of proficiently internalizing even un-opsonized particles by scavenger receptor-mediated phagocytosis via the zipper mechanism (*212-215*). The shape of the particle significantly affects the phagocytosis process; specifically, particles with a high aspect ratio can evade phagocytosis by preventing the formation of the actin structures required for particle ingestion (*216, 217*). The balance of these two opposite facets provides the niche for GLAMs to attach to the macrophage surface with prolonged retention times. This feature enables the stable loading of Gd(III) on the cell surface through preventing degradation of Gd(III)-loaded particles by intracellular enzymes or acidic conditions, and it also avoids the change of relaxivity of Gd(III) due to changes in pH (*218*). GLAMs are compatible with the carrier cells and can stably adhere to macrophages under different physiological shear stresses that they may encountered upon injection, circulation, extravasation, and migration (*219*). Together, the optimized manufacturing process, biocompatibility of materials, and stability of the system favor the clinical translation of this technology.

M-GLAMs provided a biodistribution profile that addresses current clinical challenges associated with GBCAs. Specifically, high concentrations of GBCAs are often needed for clinical diagnosis (*220*), thus the use of GBCAs is contraindicated in patients with existing kidney dysfunctions due to the potential nephrotoxicity of Gd(III) and increased risk of nephrogenic systemic fibrosis in these subjects (*221*). M-GLAMs were delivered at a dose 500-1000-fold lower compared to Gadavist®. Further, M-GLAMs exhibited negligible renal accumulation of Gd(III), thus altogether reducing renal exposure to Gd(III). The bulk structure of GLAMs is expected to be degraded in vivo by hyaluronidase (*222*), while the covalent bonds formed by the methacrylate groups are expected to be relatively stable (*223, 224*). This can allow Gd(III) to be released from GLAMs in a macromolecular form which possesses a higher stability and thus a lower tissue toxicity compared to small Gd(III) chelates (*225, 226*).

In the current clinical settings, diagnosis of mTBI remains a major challenge (*227*). The result of porcine studies presented here showed the M-GLAMs are able to differentiate healthy and pathological mTBI brains by providing differential MRI signals in the region of ChP and LV. This can be attributed to the active trafficking ability of immune cells to the inflamed brain via ChP, in line with the findings reported by others that myeloid cells traveled to the brain via the BCSF barrier after trauma (*228, 229*). This migration is driven by the release of ChP-regulated chemokines and cytokines in synergy with adhesion molecules in several physiological events in the CNS (*230*). In addition, the high blood flow rate at ChP (i.e., five to ten-fold faster than that in other tissues) and fenestrated ChP capillaries provide an exceptional niche for circulating immune cells to access and interact with ChP stroma (*231*), and these features may lead to the enhanced infiltration of M-GLAMs into the CSF via the BSCF barrier. While blood-brain barrier (BBB) can potentially provide another route for immune cells to penetrate into

the injured brain (*232*), we did not observe any overt change in BBB or nearby brain parenchyma in the MRI scans. This can potentially be attributed to the large surface of BBB (i.e., 5000-fold compared to the BCSF barrier) (*233*) that may hinder localization of the contrast agents to achieve the critical concentration required for detectable MRI signals.

4.5 Conclusion

In summary, the living contrast agent – *M-GLAM*, enable the BCSF barrier and its vicinity (i.e., ChP and LV) to serve as a new region of interest for mTBI diagnosis. Future applications of M-GLAM can be expended to diagnose other CNS disorders that involves the pathological changes at ChP (*234*). In the studies presented here, allogenic macrophages were used to prepare M-GLAMs. Clinical applications of M-GLAMs could potentially make use of engineered allogenic macrophages that can be manufactured at scale (*235, 236*). With further research focused on safety and manufacturing, M-GLAMs, a living contrast agent can open new opportunities in sensitive diagnosis of CNS disorders.

Chapter 5: Conclusions and Future Directions

5.1 Conclusions

A variety of biomaterials have been reported to broaden the dimensions of immune cell engineering, including *i*) nanoparticles that can be engulfed and carried inside the cells (*237, 238*), *ii*) polymers or particulate formulations that can be decorated on the cell surface (*174, 239, 240*), *iii*) scaffolds that can accommodate the loaded or infiltrated immune cells (*31, 241*). Among them, cell surface-bound biomaterials offer a unique opportunity not only for exploiting the chemotactic capability of immune cells to breach biological barriers and arrive hard-to-reach pathological tissues *(242)* but providing more stable cargo loading on the cell surface compared to their counterparts with intracellular payload. Specifically, when loaded with therapeutics, cell surface-associated biomaterials prevent intracellularly drug release and the consequential toxicity to the cells as well as protect the cargos from being damaged or compromised by intracellular enzymes or acidic conditions (*243*). On the other hand, given that fluorescence or contrast efficacy of imaging agents can be affected by the surrounding pH values (*244, 245*), surface-bound biomaterials prevent the change of imaging efficacy caused by intracellularly pH value shifts. Further, these biomaterials can also avoid intracellular release of imaging agents and the resulting cytotoxicity (*246, 247*).

We have demonstrated the usage of macrophage surface-associated discoidal microparticles for both therapeutic and diagnostic applications. When bounded on the cell membrane, anisotropic microparticles overcome the obstacles encountered in the case of nanoparticles. First, surface-bound particles should prevent extensively shielding or functionally compromising cell-surface molecules that are critical to cell functions (*24*). The micro-disk of 8 μm in diameter only occupied 1/25 to 1/8 of the cell surface, allowing the sufficient membrane proteins to be retained, while nanoparticles, depending on the particle to cell ratio, can block a larger cell surface area (*248-250*). Second, owing to the dynamic nature of cell membrane, the components (e.g., lipids and proteins) of the plasma membrane are constantly internalized and degraded (*251*). This turnover of cell membrane may lead to premature internalization of small particles (*252*). However, discoidal microparticles avoid cell internalization and retain on the cell surface thanks to its anisotropic shape (*217*). Third, the volume of an 8-μm disk is ~10^{10}-fold higher than that of a nanoparticle with a diameter of 200 nm. This comparison persists even with the consideration of the fact that about 70-2000 nanoparticles can be attached on one cell (*248-250, 253*). This feature enables discoidal microparticles with a greater capacity for cargo loading.

In the Chapter 3, we presented the cytokine-loaded discoidal microparticles attaching on macrophages for 4T1 breast cancer treatment. Mouse 4T1 breast tumor model is well-known for its high metastatic rate and immunosuppressive tumor microenvironment, and it has a similar pattern of progressive spread with that of human mammary cancer (*254*). Current clinical standards for malignant breast cancers include chemotherapy, hormonal therapy, immunotherapy, and targeted therapy. However, chemotherapy usually causes severe side effects and increases the risk of drug resistance (*255*); hormonal therapy and targeted therapy require certain molecule expressions on the breast cancer cell surface; immunotherapy, e.g., PD-L1, is ineffective in cold breast cancers, where the tumors possess relatively low T cell infiltration and thus are immunosuppressive (*255*). Our approach has potential to minimize the side effects caused by pro-inflammatory cytokines due to the local delivery, make the cold tumors into hot ones, and induce therapeutic effects without the necessity of certain molecule expression. Although the intra-tumoral injection we used in this project may not be translatable to the clinic, we expect to bring this technology further using the intravenous administration route in the future.

In the Chapter 4, we demonstrated the contrast agent-loaded discoidal microparticles attaching on macrophages for mild TBI diagnosis. We identified a new region of interest, i.e., the blood-CSF barrier at ChP and its vicinity, which can be applied with conventional MRI. Indeed, conventional MRI is good for detecting brain structural alterations in the clinic, yet these findings are sometimes missing in the mild TBI cases and conventional MRI provides limited information in pathophysiology and cellular processes underlying these structural alterations (*256*). Our approach images immune cell infiltration into the blood-CSF barrier at ChP, offering a new sensitive imaging modality to diagnose mild TBI and new insights into the pathophysiology of mild TBI. However, we note that other brain disorders that involve immune cell regulation at ChP can also result in enhanced MRI signals when this cell-based MRI imaging system is applied. Thus, a combination of our approach (a tool that provides the information of cellular responses) and other advanced neuroimaging tools (e.g., diffusion tensor imaging to assess the brain's microstructure; magnetic resonance spectroscopy and positron emission tomography to evaluate metabolism or protein deposition) may be required to provide a precise diagnosis of CNS disorders.

We envision the discoidal microparticles can be prepared in a modular fashion to fit the needs of diverse indications and carrier cell types. That is, the fabrication process presented in Chapter 4 provides the opportunities to incorporate various therapeutic and/or diagnostic agents in a single discoidal microparticle with a great loading efficiency. While we only demonstrated the incorporation of proinflammaroty cytokine IFNγ and MRI contrast agents gadolinium, a range of other payloads can be considered, such as tumor-encoded amino acid substitutions that facilitate adaptive immune responses toward a backpack-based vaccine (*147*), cytokines that promote anti-inflammatory phenotypes to aid in tissue regeneration or repair for autoimmune diseases (*257, 258*), and CT contrast agents for cell tracking (*259*). Further, the anisotropic microparticles can be decorated with various antibodies for efficiently attaching to the required carrier cell. In this thesis, macrophages are chosen to be the model cell for anisotropic microparticle hitchhiking, yet other immune cells with stronger chemotactic ability can also be employed (*108, 260, 261*). Altogether, the discoidal microparticles-laden leukocyte platform paves the way for a myriad of applications in the body.

5.2 Future Directions

5.2.1 Exploration of other strategies for cargo loading

In Chapter 3, we incorporated proinflammaroty cytokine IFNγ into particles using a hydrophilic middle layer sandwiched between two PLGA layers. However, this method does not offer stable loading or controlled release of the cargos, i.e., a burst release was observed in the first few hours of release. Hydrogel-based anisotropic microparticles, demonstrated in Chapter 4, provide an opportunity to liberate the payloads in a responsive manner (*262*). Specifically, the cargos requiring controlled release can be conjugated to hyaluronic acid backbone using stimulus-sensitive linkage, for example, pH-sensitive aconityl linkage (*263*), enzyme-cleavable linkers (*264*), redox-responsive linkers (*265*). On the other hand, for the cargos that does not need to be released (e.g., imaging agents), we also demonstrated the capability of hydrogel-based anisotropic microparticles to be stably loaded with MRI contrast agents.

5.2.2 Further optimization of fabrication process for anisotropic microparticle production

In Chapter 4, we presented a fabrication process that enables production of hydrogel-based anisotropic microparticles at scale, yet some steps can further be optimized. First, the technique we used for hydrogel deposition is spin-coating, by which > 50% of materials was lost during the spin. The Bong group demonstrated a strategy, called "discontinuous dewetting in a degassed mold" to fabricate polymeric microparticles (*188*), where degassed mold is employed for solution deposition on PDMS templates and discontinuous dewetting is used to remove the unwanted embossed film. Although discontinuous dewetting does not apply to remove the film made of polymers with high molecular weights, degassed mold could be a potential replacement for spin-coating to effectively deposit the hydrogel solution with a lower material loss. Second, the current collection method shown in Chapter 4 includes freezing, printing, and collecting by aqueous solution. This procedure is applicable but time-consuming. A potential alternative is to add water directly on the etched template (where the embossed film has already removed), followed by freezing it into an ice block and peeling the ice from the mold to detach the microparticles that attach to the ice (*188*), by which Kim et al. demonstrated a high recovery yield of hydrogel particles.

5.2.3 Exploration of other carrier cells

While immune cell-based strategies hold great promise in the clinic, safety remains a challenge (*34*). In the porcine study described in Chapter 4, we polarized carrier cells into anti-inflammatory M2-like macrophages with interleukine-4 (*266*) with the aim of preventing the cytokine release syndrome caused by pro-inflammatory M1-like macrophages (*267*). However, mild symptoms were still present in pigs after the M-GLAM administration. These transient anaphylactic reactions can attribute to M2 macrophage-mediated hypersensitivity (*268, 269*). Recently, the Klemke group presents a genetically edited, enucleated cell carrier to serve as a new type of cell-derived delivery system (*270*). The cells were modified to express the proteins of choice for active targeting, followed by nucleus removal to prevent uncontrollable in vivo proliferation and the downstream side effect of the cell therapy yet preserving the essential organelles required for energy and protein production. These enucleated cells offer a new opportunity to serve as a safer carrier for particle hitchhiking.

1. M. Martino *et al.*, CART-cell therapy: recent advances and new evidence in multiple myeloma. *Cancers* **13**, 2639 (2021).
2. F. Sivandzade, L. Cucullo, Regenerative stem cell therapy for neurodegenerative diseases: An overview. *International Journal of Molecular Sciences* **22**, 2153 (2021).
3. T. Kitada, B. DiAndreth, B. Teague, R. Weiss, Programming gene and engineered-cell therapies with synthetic biology. *Science* **359**, eaad1067 (2018).
4. M. A. Fischbach, J. A. Bluestone, W. A. Lim, Cell-based therapeutics: the next pillar of medicine. *Science translational medicine* **5**, 179ps177-179ps177 (2013).
5. Z. Zhao, A. Ukidve, J. Kim, S. Mitragotri, Targeting Strategies for Tissue-Specific Drug Delivery. *Cell* **181**, 151-167 (2020).
6. A. C. Anselmo, S. Mitragotri, Cell-mediated delivery of nanoparticles: taking advantage of circulatory cells to target nanoparticles. *Journal of controlled release* **190**, 531-541 (2014).
7. D. T. Riglar, P. A. Silver, Engineering bacteria for diagnostic and therapeutic applications. *Nat Rev Microbiol* **16**, 214-225 (2018).
8. S. R. Bailey, M. V. Maus, Gene editing for immune cell therapies. *Nature biotechnology* **37**, 1425-1434 (2019).
9. T. R. Heathman *et al.*, The translation of cell-based therapies: clinical landscape and manufacturing challenges. *Regenerative medicine* **10**, 49-64 (2015).
10. A. De Pieri, Y. Rochev, D. I. Zeugolis, Scaffold-free cell-based tissue engineering therapies: advances, shortfalls and forecast. *NPJ Regenerative Medicine* **6**, 1-15 (2021).
11. E. W. Weber, M. V. Maus, C. L. Mackall, The emerging landscape of immune cell therapies. *Cell* **181**, 46-62 (2020).
12. A. D. Luster, R. Alon, U. H. von Andrian, Immune cell migration in inflammation: present and future therapeutic targets. *Nature immunology* **6**, 1182-1190 (2005).
13. H. Gonzalez, C. Hagerling, Z. Werb, Roles of the immune system in cancer: from tumor initiation to metastatic progression. *Genes & development* **32**, 1267-1284 (2018).
14. R. S. Goldszmid, A. Dzutsev, G. Trinchieri, Host immune response to infection and cancer: unexpected commonalities. *Cell host & microbe* **15**, 295-305 (2014).
15. Z. Julier, A. J. Park, P. S. Briquez, M. M. Martino, Promoting tissue regeneration by modulating the immune system. *Acta biomaterialia* **53**, 13-28 (2017).
16. R. Andreesen, B. Hennemann, S. W. Krause, Adoptive immunotherapy of cancer using monocyte-derived macrophages: rationale, current status, and perspectives. *Journal of leukocyte biology* **64**, 419-426 (1998).
17. J. A. Wagner *et al.*, CD56 bright NK cells exhibit potent antitumor responses following IL-15 priming. *The Journal of clinical investigation* **127**, 4042-4058 (2017).
18. K. C. Conlon *et al.*, Redistribution, hyperproliferation, activation of natural killer cells and CD8 T cells, and cytokine production during first-in-human clinical trial of recombinant human interleukin-15 in patients with cancer. *Journal of clinical oncology* **33**, 74 (2015).
19. W. H. West *et al.*, Constant-infusion recombinant interleukin-2 in adoptive immunotherapy of advanced cancer. *New England Journal of Medicine* **316**, 898-905 (1987).
20. N. A. Ivica, C. M. Young, in *Healthcare*. (MDPI, 2021), vol. 9, pp. 1062.
21. K. Pan *et al.*, CAR race to cancer immunotherapy: from CAR T, CAR NK to CAR macrophage therapy. *Journal of Experimental & Clinical Cancer Research* **41**, 1-21 (2022).

22. S. Lee, S. Kivimäe, A. Dolor, F. C. Szoka, Macrophage-based cell therapies: the long and winding road. *Journal of Controlled Release* **240**, 527-540 (2016).
23. K. J. Brempelis *et al.*, Genetically engineered macrophages persist in solid tumors and locally deliver therapeutic proteins to activate immune responses. *Journal for immunotherapy of cancer* **8**, (2020).
24. M. T. Stephan, D. J. Irvine, Enhancing cell therapies from the outside in: cell surface engineering using synthetic nanomaterials. *Nano today* **6**, 309-325 (2011).
25. Y. C. Dong, M. Bouche, S. Uman, J. A. Burdick, D. P. Cormode, Detecting and monitoring hydrogels with medical imaging. *ACS Biomaterials Science & Engineering* **7**, 4027-4047 (2021).
26. M. A. Evans *et al.*, Macrophage-Mediated Delivery of Hypoxia-Activated Prodrug Nanoparticles. *Advanced Therapeutics* **3**, 1900162 (2020).
27. J. Xia *et al.*, Catalase-laden microdevices for cell-mediated enzyme delivery. *Langmuir* **32**, 13386-13393 (2016).
28. D. J. Irvine, E. L. Dane, Enhancing cancer immunotherapy with nanomedicine. *Nature Reviews Immunology* **20**, 321-334 (2020).
29. J. I. Andorko, C. M. Jewell, Designing biomaterials with immunomodulatory properties for tissue engineering and regenerative medicine. *Bioengineering & translational medicine* **2**, 139-155 (2017).
30. O. S. Fenton, K. N. Olafson, P. S. Pillai, M. J. Mitchell, R. Langer, Advances in biomaterials for drug delivery. *Advanced Materials* **30**, 1705328 (2018).
31. A. S. Cheung, D. K. Y. Zhang, S. T. Koshy, D. J. Mooney, Scaffolds that mimic antigen-presenting cells enable ex vivo expansion of primary T cells. *Nat Biotechnol* **36**, 160-169 (2018).
32. C. W. Shields *et al.*, Cellular backpacks for macrophage immunotherapy. *Science Advances* **6**, eaaz6579 (2020).
33. D. Salthouse, K. Novakovic, C. M. Hilkens, A. M. Ferreira, Interplay between biomaterials and the immune system: challenges and opportunities in regenerative medicine. *Acta Biomaterialia*, (2022).
34. L. L. W. Wang *et al.*, Cell therapies in the clinic. *Bioengineering & translational medicine* **6**, e10214 (2021).
35. D. Seimetz, K. Heller, J. Richter, Approval of first CAR-Ts: have we solved all hurdles for ATMPs? *Cell Medicine* **11**, 2155179018822781 (2019).
36. B. Gharaibeh, J. E. Anderson, B. M. Deasy, Combating the threat of stem cell tourism through patient education and government regulation. *Innovation and Entrepreneurship in Health* **3**, 15 (2016).
37. S. Gottipamula, S. Bhat, R. N. Seetharam, Mesenchymal Stromal Cells: Basics, Classification, and Clinical Applications. *Journal of Stem Cells* **13**, 23-47 (2018).
38. . vol. 2020.
39. L. Zaulyanov, R. S. Kirsner, A review of a bi-layered living cell treatment (Apligraf®) in the treatment of venous leg ulcers and diabetic foot ulcers. *Clinical interventions in aging* **2**, 93 (2007).
40. E. Basad, B. Ishaque, G. Bachmann, H. Stürz, J. Steinmeyer, Matrix-induced autologous chondrocyte implantation versus microfracture in the treatment of cartilage defects of the knee: a 2-year randomised study. *Knee surgery, sports traumatology, arthroscopy* **18**, 519-527 (2010).

41. R. V. Shevchenko, S. L. James, S. E. James, A review of tissue-engineered skin bioconstructs available for skin reconstruction. *Journal of the Royal Society Interface* **7**, 229-258 (2010).
42. B. J. Huang, J. C. Hu, K. A. Athanasiou, Cell-based tissue engineering strategies used in the clinical repair of articular cartilage. *Biomaterials* **98**, 1-22 (2016).
43. H. G. Klein, D. J. Anstee, *Mollison's blood transfusion in clinical medicine*. (John Wiley & Sons, 2014).
44. . vol. 2020.
45. J. Jayaraman *et al.*, CAR-T design: Elements and their synergistic function. *EBioMedicine* **58**, 102931 (2020).
46. L. G. Rodriguez-Cartagena *et al.*, Chimeric Antigen Receptor T-Cells: Successful Translation of the First Cell and Gene Therapy From Bench to Bedside. *Clinical and translational science* **11**, 537 (2018).
47. . vol. 2020.
48. . vol. 2020.
49. M. Wang *et al.*, KTE-X19 CAR T-cell therapy in relapsed or refractory mantle-cell lymphoma. *New England Journal of Medicine* **382**, 1331-1342 (2020).
50. T. Takayama *et al.*, Adoptive immunotherapy to lower postsurgical recurrence rates of hepatocellular carcinoma: a randomised trial. *The Lancet* **356**, 802-807 (2000).
51. J. H. Lee *et al.*, Adjuvant immunotherapy with autologous cytokine-induced killer cells for hepatocellular carcinoma. *Gastroenterology* **148**, 1383-1391. e1386 (2015).
52. V. Rocha, E. Gluckman, Clinical use of umbilical cord blood hematopoietic stem cells. *Biology of Blood and Marrow Transplantation* **12**, 34-41 (2006).
53. E. Gluckman *et al.*, Outcome of cord-blood transplantation from related and unrelated donors. *New England Journal of Medicine* **337**, 373-381 (1997).
54. . vol. 2020.
55. F. Gao *et al.*, Mesenchymal stem cells and immunomodulation: current status and future prospects. *Cell death & disease* **7**, e2062-e2062 (2016).
56. H. Zhu, B. Yu, L. Yang, Exogenous and Endogenous Stem Cells for Skeletal Regeneration. *Stem Cells International* **2018**, (2018).
57. O. Levy *et al.*, Shattering barriers toward clinically meaningful MSC therapies. *Science Advances* **6**, eaba6884 (2020).
58. Y. B. Park, C. W. Ha, C. H. Lee, Y. C. Yoon, Y. G. Park, Cartilage regeneration in osteoarthritic patients by a composite of allogeneic umbilical cord blood-derived mesenchymal stem cells and hyaluronate hydrogel: results from a clinical trial for safety and proof-of-concept with 7 years of extended follow-up. *Stem cells translational medicine* **6**, 613-621 (2017).
59. L. J. Scott, Darvadstrocel: A Review in Treatment-Refractory Complex Perianal Fistulas in Crohn's Disease. *BioDrugs* **32**, 627-634 (2018).
60. J. Kurtzberg *et al.*, A phase 3, single-arm, prospective study of remestemcel-l, ex vivo culture-expanded adult human mesenchymal stromal cells for the treatment of pediatric patients who failed to respond to steroid treatment for acute graft-versus-host disease. *Biology of Blood and Marrow Transplantation*, (2020).
61. M. A. Cheever, C. S. Higano, PROVENGE (Sipuleucel-T) in prostate cancer: the first FDA-approved therapeutic cancer vaccine. *Clinical Cancer Research* **17**, 3520-3526 (2011).
62. R. F. AFRC, Probiotics in man and animals. *Journal of applied bacteriology* **66**, 365-378 (1989).

63. N. T. Williams, Probiotics. *American Journal of Health-System Pharmacy* **67**, 449-458 (2010).
64. J. Suez, N. Zmora, E. Segal, E. Elinav, The pros, cons, and many unknowns of probiotics. *Nature medicine* **25**, 716-729 (2019).
65. P. W. O'Toole, J. R. Marchesi, C. Hill, Next-generation probiotics: the spectrum from probiotics to live biotherapeutics. *Nature microbiology* **2**, 1-6 (2017).
66. R. J. Brentjens *et al.*, Eradication of systemic B-cell tumors by genetically targeted human T lymphocytes co-stimulated by CD80 and interleukin-15. *Nature medicine* **9**, 279-286 (2003).
67. M. Kalos *et al.*, T cells with chimeric antigen receptors have potent antitumor effects and can establish memory in patients with advanced leukemia. *Science translational medicine* **3**, 95ra73-95ra73 (2011).
68. D. L. Porter, B. L. Levine, M. Kalos, A. Bagg, C. H. June, Chimeric antigen receptor–modified T cells in chronic lymphoid leukemia. *N engl j Med* **365**, 725-733 (2011).
69. M. Sadelain, I. Rivière, R. Brentjens, Targeting tumours with genetically enhanced T lymphocytes. *Nature Reviews Cancer* **3**, 35-45 (2003).
70. D. D. Chaplin, Overview of the immune response. *Journal of Allergy and Clinical Immunology* **125**, S3-S23 (2010).
71. A. M. Abel, C. Yang, M. S. Thakar, S. Malarkannan, Natural killer cells: development, maturation, and clinical utilization. *Frontiers in immunology* **9**, 1869 (2018).
72. A. Gardner, B. Ruffell, Dendritic cells and cancer immunity. *Trends in immunology* **37**, 855-865 (2016).
73. H. Yu, Y. Tian, Y. Wang, S. Mineishi, Y. Zhang, Dendritic cell regulation of graft-vs.-host disease: immunostimulation and tolerance. *Frontiers in immunology* **10**, 93 (2019).
74. R. M. Kratofil, P. Kubes, J. F. Deniset, Monocyte conversion during inflammation and injury. *Arteriosclerosis, thrombosis, and vascular biology* **37**, 35-42 (2017).
75. V. Kumar, in *Macrophage at the Crossroads of Innate and Adaptive Immunity*. (IntechOpen, 2019).
76. A. Y. Lee, N. Mahler, C. Best, Y.-U. Lee, C. K. Breuer, Regenerative implants for cardiovascular tissue engineering. *Translational research* **163**, 321-341 (2014).
77. V. Kuhn *et al.*, Red blood cell function and dysfunction: redox regulation, nitric oxide metabolism, anemia. *Antioxidants & redox signaling* **26**, 718-742 (2017).
78. M. Holinstat, Normal platelet function. *Cancer and Metastasis Reviews* **36**, 195-198 (2017).
79. C. Chabannon *et al.*, Hematopoietic stem cell transplantation in its 60s: a platform for cellular therapies. *Science translational medicine* **10**, (2018).
80. D. Hutt, in *The European Blood and Marrow Transplantation Textbook for Nurses*. (Springer, Cham, 2018), pp. 259-270.
81. S. A. Agnihotri, N. N. Mallikarjuna, T. M. Aminabhavi, Recent advances on chitosan-based micro- and nanoparticles in drug delivery. *Journal of Controlled Release* **100**, 5-28 (2004).
82. I. Ullah, R. B. Subbarao, G. J. Rho, Human mesenchymal stem cells-current trends and future prospective. *Bioscience reports* **35**, (2015).
83. A. M. Vargason, A. C. Anselmo, Clinical translation of microbe-based therapies: Current clinical landscape and preclinical outlook. *Bioengineering & translational medicine* **3**, 124-137 (2018).

84. C. S. Hinrichs *et al.*, IL-2 and IL-21 confer opposing differentiation programs to CD8+ T cells for adoptive immunotherapy. *Blood, The Journal of the American Society of Hematology* **111**, 5326-5333 (2008).
85. L. Gattinoni *et al.*, Wnt signaling arrests effector T cell differentiation and generates CD8+ memory stem cells. *Nature medicine* **15**, 808-813 (2009).
86. Y. Chen, S. Pal, Q. Hu, Recent advances in biomaterial-assisted cell therapy. *Journal of Materials Chemistry B*, (2022).
87. A. L. Facklam, L. R. Volpatti, D. G. Anderson, Biomaterials for personalized cell therapy. *Advanced materials* **32**, 1902005 (2020).
88. C. W. Shields IV, L. L. W. Wang, M. A. Evans, S. Mitragotri, Materials for immunotherapy. *Advanced Materials* **32**, 1901633 (2020).
89. L. Milling, Y. Zhang, D. J. Irvine, Delivering safer immunotherapies for cancer. *Adv Drug Deliv Rev* **114**, 79-101 (2017).
90. D. N. Khalil, E. L. Smith, R. J. Brentjens, J. D. Wolchok, The future of cancer treatment: immunomodulation, CARs and combination immunotherapy. *Nature Reviews Clinical Oncology* **13**, 273–290 (2016).
91. A. N. Miliotou, L. C. Papadopoulou, CAR T-cell Therapy: A New Era in Cancer Immunotherapy. *Curr Pharm Biotechnol* **19**, 5-18 (2018).
92. G. Hucks, S. R. Rheingold, The journey to CAR T cell therapy: the pediatric and young adult experience with relapsed or refractory B-ALL. *Blood Cancer J* **9**, 10 (2019).
93. S. Lee, S. Kivimae, A. Dolor, F. C. Szoka, Macrophage-based cell therapies: The long and winding road. *J Control Release* **240**, 527-540 (2016).
94. T. A. Wynn, A. Chawla, J. W. Pollard, Macrophage biology in development, homeostasis and disease. *Nature* **496**, 445-455 (2013).
95. F. O. Martinez, S. Gordon, The M1 and M2 paradigm of macrophage activation: time for reassessment. *F1000Prime Reports* **6**, 1-13 (2014).
96. J. M. Brown, L. Recht, S. Strober, The Promise of Targeting Macrophages in Cancer Therapy. *Clin Cancer Res* **23**, 3241-3250 (2017).
97. J. L. Schultze, A. Schmieder, S. Goerdt, Macrophage activation in human diseases. *Semin Immunol* **27**, 249-256 (2015).
98. M. A. Evans *et al.*, Macrophage-mediated delivery of light activated nitric oxide prodrugs with spatial, temporal and concentration control. *Chem Sci* **9**, 3729-3741 (2018).
99. C. B. Williams, E. S. Yeh, A. C. Soloff, Tumor-associated macrophages: unwitting accomplices in breast cancer malignancy. *npj Breast Cancer* **2**, 15025 (2016).
100. J. A. Champion, S. Mitragotri, Role of target geometry in phagocytosis. *Proc Natl Acad Sci U S A* **103**, 4930-4934 (2006).
101. N. Doshi *et al.*, Cell-based drug delivery devices using phagocytosis-resistant backpacks. *Adv Mater* **23**, H105-109 (2011).
102. A. C. Anselmo *et al.*, Monocyte-mediated delivery of polymeric backpacks to inflamed tissues: a generalized strategy to deliver drugs to treat inflammation. *J Control Release* **199**, 29-36 (2015).
103. J. Xia *et al.*, Asymmetric biodegradable microdevices for cell-borne drug delivery. *ACS Appl Mater Interfaces* **7**, 6293-6299 (2015).
104. R. Polak *et al.*, Liposome-Loaded Cell Backpacks. *Adv Healthc Mater* **4**, 2832-2841 (2015).

105. Z. Wang *et al.*, Facile functionalization and assembly of live cells with microcontact-printed polymeric biomaterials. *Acta Biomater* **11**, 80-87 (2015).
106. N. L. Klyachko *et al.*, Macrophages with cellular backpacks for targeted drug delivery to the brain. *Biomaterials* **140**, 79-87 (2017).
107. Z. Wang *et al.*, Fabrication of carbon nanotube-laden microdevices for Raman labeling of macrophages. *Biomedical Physics & Engineering Express* **3**, 025012 (2017).
108. B. Huang *et al.*, Active targeting of chemotherapy to disseminated tumors using nanoparticle-carrying T cells. *Science Translational Medicine* **7**, 291ra294 (2015).
109. P. Zhang, J. Guan, Fabrication of multilayered microparticles by integrating layer-by-layer assembly and microcontact printing. *Small* **7**, 2998-3004 (2011).
110. M. Weis *et al.*, Evaluation of Hydrogels Based on Oxidized Hyaluronic Acid for Bioprinting. *Gels* **4**, 82 (2018).
111. X. Zhang, R. Goncalves, D. M. Mosser, The isolation and characterization of murine macrophages. *Curr Protoc Immunol* **Chapter 14**, Unit 14 11 (2008).
112. R. Andreesen *et al.*, Adoptive Transfer of Tumor Cytotoxic Macrophages Generated in Vitro from Circulating Blood Monocytes: A New Approach to Cancer Immunotherapy. *Cancer Research* **50**, 7450-7456 (1990).
113. A. Pusuluri *et al.*, Role of synergy and immunostimulation in design of chemotherapy combinations: An analysis of doxorubicin and camptothecin. *Bioeng Transl Med* **4**, e10129 (2019).
114. C. W. Shields IV, L. L. Wang, M. A. Evans, S. Mitragotri, Materials for Immunotherapy. *Adv Mater*, e1901633 (2019).
115. C. Baer *et al.*, Suppression of microRNA activity amplifies IFN-gamma-induced macrophage activation and promotes anti-tumour immunity. *Nat Cell Biol* **18**, 790-802 (2016).
116. K. Schroder, P. J. Hertzog, T. Ravasi, D. A. Hume, Interferon-gamma: an overview of signals, mechanisms and functions. *J Leukoc Biol* **75**, 163-189 (2004).
117. F. C. Vasconcellos, A. J. Swiston, M. M. Beppu, R. E. Cohen, M. F. Rubner, Bioactive Polyelectrolyte Multilayers: Hyaluronic Acid Mediated B Lymphocyte Adhesion. *Biomacromolecules* **11**, 2407-2414 (2010).
118. L. Maródi *et al.*, Enhancement of macrophage candidacidal activity by interferon-gamma. *J Clin Invest* **91**, 2596-2601 (1993).
119. P. Tripathi, P. Tripathi, L. Kashyap, V. Singh, The role of nitric oxide in inflammatory reactions. *FEMS Immunology & Medical Microbiology* **51**, 443-452 (2007).
120. V. Steimle, C. Siegrist, A. Mottet, B. Lisowska-Grospierre, B. Mach, Regulation of MHC class II expression by interferon-gamma mediated by the transactivator gene CIITA. *Science* **265**, 106-109 (1994).
121. C. Wu *et al.*, IFN-gamma primes macrophage activation by increasing phosphatase and tensin homolog via downregulation of miR-3473b. *J Immunol* **193**, 3036-3044 (2014).
122. A. M. Labrousse *et al.*, Frustrated phagocytosis on micro-patterned immune complexes to characterize lysosome movements in live macrophages. *Front Immunol* **2**, 51 (2011).
123. A. Mularski, F. Marie-Anaïs, J. Mazzolini, F. Niedergang, *Observing Frustrated Phagocytosis and Phagosome Formation and Closure Using Total Internal Reflection Fluorescence Microscopy (TIRFM)*. G. Rousselet, Ed., (Humana Press New York, NY, 2018).

124. K. Mittal, J. Ebos, B. Rini, Angiogenesis and the tumor microenvironment: vascular endothelial growth factor and beyond. *Semin Oncol* **41**, 235-251 (2014).
125. A. L. Doedens *et al.*, Macrophage expression of hypoxia-inducible factor-1 alpha suppresses T-cell function and promotes tumor progression. *Cancer Res* **70**, 7465-7475 (2010).
126. P. Scodeller *et al.*, Precision Targeting of Tumor Macrophages with a CD206 Binding Peptide. *Sci Rep* **7**, 14655 (2017).
127. C. B. Williams, E. S. Yeh, A. C. Soloff, Tumor-associated macrophages: unwitting accomplices in breast cancer malignancy. *NPJ Breast Cancer* **2**, (2016).
128. R. Deng *et al.*, Inhibition of Tumor Growth and Alteration of Associated Macrophage Cell Type by an HO-1 Inhibitor in Breast Carcinoma-Bearing Mice. *Oncology Research Featuring Preclinical and Clinical Cancer Therapeutics* **20**, 473-482 (2012).
129. W. Durante, F. K. Johnson, R. A. Johnson, Arginase: A critical regulator of nitric oxide synthesis and vascular function. *Clin Exp Pharmacol Physiol* **34**, 906-911 (2007).
130. C. Perrotta *et al.*, Nitric Oxide Generated by Tumor-Associated Macrophages Is Responsible for Cancer Resistance to Cisplatin and Correlated With Syntaxin 4 and Acid Sphingomyelinase Inhibition. *Front Immunol* **9**, 1186 (2018).
131. Y. W. Choo *et al.*, M1 Macrophage-Derived Nanovesicles Potentiate the Anticancer Efficacy of Immune Checkpoint Inhibitors. *ACS Nano* **12**, 8977-8993 (2018).
132. Y. Wang *et al.*, Polymeric nanoparticles promote macrophage reversal from M2 to M1 phenotypes in the tumor microenvironment. *Biomaterials* **112**, 153-163 (2017).
133. M. Song, T. Liu, C. Shi, X. Zhang, X. Chen, Bioconjugated Manganese Dioxide Nanoparticles Enhance Chemotherapy Response by Priming Tumor-Associated Macrophages toward M1-like Phenotype and Attenuating Tumor Hypoxia. *ACS Nano* **10**, 633-647 (2016).
134. S. Zanganeh *et al.*, Iron oxide nanoparticles inhibit tumour growth by inducing pro-inflammatory macrophage polarization in tumour tissues. *Nat Nanotechnol* **11**, 986-994 (2016).
135. J. L. Guerriero *et al.*, Class IIa HDAC inhibition reduces breast tumours and metastases through anti-tumour macrophages. *Nature* **543**, 428-432 (2017).
136. C. X. Li *et al.*, Artificially Reprogrammed Macrophages as Tumor-Tropic Immunosuppression-Resistant Biologics to Realize Therapeutics Production and Immune Activation. *Adv Mater* **31**, e1807211 (2019).
137. S. Edin *et al.*, The distribution of macrophages with a M1 or M2 phenotype in relation to prognosis and the molecular characteristics of colorectal cancer. *PLoS One* **7**, e47045 (2012).
138. A. Yuan *et al.*, Opposite Effects of M1 and M2 Macrophage Subtypes on Lung Cancer Progression. *Sci Rep* **5**, 14273 (2015).
139. Y. Zhang *et al.*, High-infiltration of tumor-associated macrophages predicts unfavorable clinical outcome for node-negative breast cancer. *PLoS One* **8**, e76147 (2013).
140. C. D. Mills, L. L. Lenz, R. A. Harris, A Breakthrough: Macrophage-Directed Cancer Immunotherapy. *Cancer Res* **76**, 513-516 (2016).
141. T. O'Sullivan *et al.*, Cancer immunoediting by the innate immune system in the absence of adaptive immunity. *J Exp Med* **209**, 1869-1882 (2012).

142. L. F. Tremble, P. F. Forde, D. M. Soden, Clinical evaluation of macrophages in cancer: role in treatment, modulation and challenges. *Cancer Immunology, Immunotherapy* **66**, 1509-1527 (2017).
143. A. Ramesh, S. Kumar, D. Nandi, A. Kulkarni, CSF1R- and SHP2-Inhibitor-Loaded Nanoparticles Enhance Cytotoxic Activity and Phagocytosis in Tumor-Associated Macrophages. *Adv Mater*, e1904364 (2019).
144. N. N. Parayath, A. Parikh, M. M. Amiji, Repolarization of Tumor-Associated Macrophages in a Genetically Engineered Nonsmall Cell Lung Cancer Model by Intraperitoneal Administration of Hyaluronic Acid-Based Nanoparticles Encapsulating MicroRNA-125b. *Nano Lett* **18**, 3571-3579 (2018).
145. Y. Liu *et al.*, Blockade of IDO-kynurenine-AhR metabolic circuitry abrogates IFN-gamma-induced immunologic dormancy of tumor-repopulating cells. *Nat Commun* **8**, 15207 (2017).
146. C. H. Miller, S. G. Maher, H. A. Young, Clinical Use of Interferon-gamma. *Ann N Y Acad Sci* **1182**, 69-79 (2009).
147. B. M. Carreno *et al.*, A dendritic cell vaccine increases the breadth and diversity of melanoma neoantigen-specific T cells. *Science* **348**, 803-808 (2015).
148. T. Wang *et al.*, A cancer vaccine-mediated postoperative immunotherapy for recurrent and metastatic tumors. *Nat Commun* **9**, 1532 (2018).
149. K. Javed, V. Reddy, F. Lui, in *StatPearls [Internet]*. (StatPearls Publishing, 2021).
150. J.-F. Ghersi-Egea *et al.*, Molecular anatomy and functions of the choroidal blood-cerebrospinal fluid barrier in health and disease. *Acta neuropathologica* **135**, 337-361 (2018).
151. A. C. Yang *et al.*, Dysregulation of brain and choroid plexus cell types in severe COVID-19. *Nature* **595**, 565-571 (2021).
152. C. Kaur, G. Rathnasamy, E.-A. Ling, The choroid plexus in healthy and diseased brain. *Journal of Neuropathology & Experimental Neurology* **75**, 198-213 (2016).
153. V. Hubert *et al.*, Clinical imaging of choroid plexus in health and in brain disorders: a mini-review. *Frontiers in molecular neuroscience* **12**, 34 (2019).
154. C. Johanson, E. Stopa, A. Baird, H. Sharma, Traumatic brain injury and recovery mechanisms: peptide modulation of periventricular neurogenic regions by the choroid plexus–CSF nexus. *Journal of neural transmission* **118**, 115-133 (2011).
155. C. N. Bodnar, J. B. Watson, E. K. Higgins, N. Quan, A. D. Bachstetter, Inflammatory regulation of cns barriers after traumatic brain injury: A tale directed by interleukin-1. *Frontiers in Immunology* **12**, 688254 (2021).
156. A. I. Maas *et al.*, Traumatic brain injury: integrated approaches to improve prevention, clinical care, and research. *The Lancet Neurology* **16**, 987-1048 (2017).
157. M. C. Dewan *et al.*, Estimating the global incidence of traumatic brain injury. *Journal of neurosurgery* **130**, 1080-1097 (2018).
158. Q. Statements, VA/DoD clinical practice guideline for management of concussion/mild traumatic brain injury. *J. Rehabil. Res. Dev* **46**, 1-60 (2009).
159. J. D. Cassidy *et al.*, Incidence, risk factors and prevention of mild traumatic brain injury: results of the WHO Collaborating Centre Task Force on Mild Traumatic Brain Injury. *Journal of rehabilitation medicine* **36**, 28-60 (2004).
160. L. Holm, J. D. Cassidy, L. J. Carroll, J. Borg, Summary of the WHO collaborating centre for neurotrauma task force on mild traumatic brain injury. *Journal of rehabilitation medicine* **37**, 137-141 (2005).

161. D. I. Katz, S. I. Cohen, M. P. Alexander, Mild traumatic brain injury. *Handbook of clinical neurology* **127**, 131-156 (2015).
162. S. C. Hellewell, C. S. Beaton, T. Welton, S. M. Grieve, Characterizing the risk of depression following mild traumatic brain injury: a meta-analysis of the literature comparing chronic mTBI to non-mTBI populations. *Frontiers in neurology* **11**, 350 (2020).
163. D. E. Barnes *et al.*, Association of mild traumatic brain injury with and without loss of consciousness with dementia in US military veterans. *JAMA neurology* **75**, 1055-1061 (2018).
164. R. C. Gardner *et al.*, Mild TBI and risk of Parkinson disease: a chronic effects of neurotrauma consortium study. *Neurology* **90**, e1771-e1779 (2018).
165. J. J. Kim, A. D. Gean, Imaging for the diagnosis and management of traumatic brain injury. *Neurotherapeutics* **8**, 39-53 (2011).
166. P. Caravan, J. J. Ellison, T. J. McMurry, R. B. Lauffer, Gadolinium (III) chelates as MRI contrast agents: structure, dynamics, and applications. *Chemical reviews* **99**, 2293-2352 (1999).
167. S. Mondello *et al.*, The challenge of mild traumatic brain injury: role of biochemical markers in diagnosis of brain damage. *Medicinal research reviews* **34**, 503-531 (2014).
168. W. Rutland-Brown *et al.*, Traumatic brain injuries after mass-casualty incidents: lessons from the 11 September 2001 World Trade Center attacks. *Prehospital and disaster medicine* **22**, 157-164 (2007).
169. M. Jodoin *et al.*, Incidence rate of mild traumatic brain injury among patients who have suffered from an isolated limb fracture: upper limb fracture patients are more at risk. *Injury* **47**, 1835-1840 (2016).
170. H. Zetterberg, D. H. Smith, K. Blennow, Biomarkers of mild traumatic brain injury in cerebrospinal fluid and blood. *Nature Reviews Neurology* **9**, 201-210 (2013).
171. A. Sharma *et al.*, Mild traumatic brain injury exacerbates Parkinson's disease induced hemeoxygenase-2 expression and brain pathology: Neuroprotective effects of co-administration of TiO2 nanowired mesenchymal stem cells and cerebrolysin. *Progress in Brain Research* **258**, 157-231 (2020).
172. B.-Z. Qian *et al.*, CCL2 recruits inflammatory monocytes to facilitate breast-tumour metastasis. *Nature* **475**, 222-225 (2011).
173. K. Rezai-Zadeh, D. Gate, G. Gowing, T. Town, How to get from here to there: macrophage recruitment in Alzheimer's disease. *Current Alzheimer Research* **8**, 156-163 (2011).
174. N. L. Klyachko *et al.*, Macrophages with cellular backpacks for targeted drug delivery to the brain. *Biomaterials* **140**, 79-87 (2017).
175. A. Alam *et al.*, Cellular infiltration in traumatic brain injury. *Journal of neuroinflammation* **17**, 1-17 (2020).
176. C. Wang *et al.*, Self-polymerization and co-polymerization kinetics of gadolinium methacrylate. *Journal of Rare Earths* **36**, 298-303 (2018).
177. M. Guvendiren, J. A. Burdick, Stiffening hydrogels to probe short-and long-term cellular responses to dynamic mechanics. *Nature communications* **3**, 1-9 (2012).
178. D. B. Weibel, W. R. DiLuzio, G. M. Whitesides, Microfabrication meets microbiology. *Nature Reviews Microbiology* **5**, 209-218 (2007).

179. V. S. Marangoni *et al.*, Enhancing T1 magnetic resonance imaging contrast with internalized gadolinium (III) in a multilayer nanoparticle. *Proceedings of the National Academy of Sciences* **114**, 6960-6965 (2017).
180. R. Mannix *et al.*, Internal jugular vein compression collar mitigates histopathological alterations after closed head rotational head impact in swine: A pilot study. *Neuroscience* **437**, 132-144 (2020).
181. K. M. Guskiewicz, J. P. Mihalik, Biomechanics of sport concussion: quest for the elusive injury threshold. *Exercise and sport sciences reviews* **39**, 4-11 (2011).
182. J. Taylor, *Introduction to error analysis, the study of uncertainties in physical measurements*. (1997).
183. G. Huang, H. Huang, Application of hyaluronic acid as carriers in drug delivery. *Drug delivery* **25**, 766-772 (2018).
184. G. Stojkov, Z. Niyazov, F. Picchioni, R. K. Bose, Relationship between structure and rheology of hydrogels for various applications. *Gels* **7**, 255 (2021).
185. S. Gu, G. Cheng, T. Yang, X. Ren, G. Gao, Mechanical and Rheological Behavior of Hybrid Cross-Linked Polyacrylamide/Cationic Micelle Hydrogels. *Macromolecular Materials and Engineering* **302**, 1700402 (2017).
186. N. Doshi *et al.*, Cell-Based drug delivery devices using Phagocytosis-Resistant backpacks. *Advanced Materials* **23**, H105-H109 (2011).
187. T. J. Merkel *et al.*, The effect of particle size on the biodistribution of low-modulus hydrogel PRINT particles. *Journal of controlled release* **162**, 37-44 (2012).
188. H. U. Kim, Y. H. Roh, S. J. Mun, K. W. Bong, Discontinuous dewetting in a degassed mold for fabrication of homogeneous polymeric microparticles. *ACS Applied Materials & Interfaces* **12**, 53318-53327 (2020).
189. R. J. Jackman, D. C. Duffy, E. Ostuni, N. D. Willmore, G. M. Whitesides, Fabricating large arrays of microwells with arbitrary dimensions and filling them using discontinuous dewetting. *Analytical chemistry* **70**, 2280-2287 (1998).
190. Y. Xia, G. M. Whitesides, Soft lithography. *Angewandte Chemie International Edition* **37**, 550-575 (1998).
191. M. E. Helgeson, S. C. Chapin, P. S. Doyle, Hydrogel microparticles from lithographic processes: Novel materials for fundamental and applied colloid science. *Current opinion in colloid & interface science* **16**, 106-117 (2011).
192. J. Menges, P. Kleinschmidt, H.-J. Bart, E. Oesterschulze, A precision structured smart hydrogel for sensing applications. *Journal of Applied Physics* **122**, 134501 (2017).
193. S. Hassanpour-Tamrin, A. Sanati-Nezhad, A. Sen, A simple and low-cost approach for irreversible bonding of polymethylmethacrylate and polydimethylsiloxane at room temperature for high-pressure hybrid microfluidics. *Scientific Reports* **11**, 1-12 (2021).
194. S. D. Oberdick, G. Zabow, Patterned Surface Energy in Elastomeric Molds as a Generalized Approach to Polymer Particle Fabrication. *ACS applied polymer materials* **2**, 846-852 (2020).
195. T. Rutt *et al.*, Thermal expansion of substrate may affect adhesion of Chinese hamster fibroblasts to surfaces during freezing. *Cryobiology* **86**, 134-139 (2019).
196. A. D. Elster, W. T. Sobol, W. H. Hinson, Pseudolayering of Gd-DTPA in the urinary bladder. *Radiology* **174**, 379-381 (1990).
197. G. E. Hagberg, K. Scheffler, Effect of r1 and r2 relaxivity of gadolinium-based contrast agents on the T1-weighted MR signal at increasing magnetic field strengths. *Contrast media & molecular imaging* **8**, 456-465 (2013).

198. P. Eriksson *et al.*, Cerium Oxide Nanoparticles with Entrapped Gadolinium for High T 1 Relaxivity and ROS-Scavenging Purposes. *ACS Omega*, (2022).
199. J. S. Ananta *et al.*, Geometrical confinement of gadolinium-based contrast agents in nanoporous particles enhances T 1 contrast. *Nature nanotechnology* **5**, 815-821 (2010).
200. M. W. Rotz *et al.*, High relaxivity Gd (III)–DNA gold nanostars: investigation of shape effects on proton relaxation. *ACS nano* **9**, 3385-3396 (2015).
201. P. Caravan, Strategies for increasing the sensitivity of gadolinium based MRI contrast agents. *Chemical Society Reviews* **35**, 512-523 (2006).
202. V. Jacques *et al.*, High relaxivity MRI contrast agents part 2: Optimization of inner-and second-sphere relaxivity. *Investigative radiology* **45**, 613 (2010).
203. E. V. Soloff, C. L. Wang, Safety of gadolinium-based contrast agents in patients with stage 4 and 5 chronic kidney disease: A radiologist's perspective. *Kidney360* **1**, 123 (2020).
204. A. Z. Khawaja *et al.*, Revisiting the risks of MRI with Gadolinium based contrast agents—review of literature and guidelines. *Insights into imaging* **6**, 553-558 (2015).
205. S. K. Shin, E. E. Kaiser, F. D. West, Alcohol induced brain and liver damage: advantages of a porcine alcohol use disorder model. *Frontiers in Physiology* **11**, 592950 (2021).
206. R. Vink, Large animal models of traumatic brain injury. *Journal of neuroscience research* **96**, 527-535 (2018).
207. P. A. Yushkevich *et al.*, User-guided 3D active contour segmentation of anatomical structures: significantly improved efficiency and reliability. *Neuroimage* **31**, 1116-1128 (2006).
208. B. Lee, A. Newberg, Neuroimaging in traumatic brain imaging. *NeuroRx* **2**, 372-383 (2005).
209. A. Fallacara, E. Baldini, S. Manfredini, S. Vertuani, Hyaluronic acid in the third millennium. *Polymers* **10**, 701 (2018).
210. H. Zhong, G. Chan, Y. Hu, H. Hu, D. Ouyang, A comprehensive map of FDA-approved pharmaceutical products. *Pharmaceutics* **10**, 263 (2018).
211. E. Uribe-Querol, C. Rosales, Phagocytosis: our current understanding of a universal biological process. *Frontiers in Immunology* **11**, 1066 (2020).
212. Q. Taban, P. T. Mumtaz, K. Z. Masoodi, E. Haq, S. M. Ahmad, Scavenger receptors in host defense: from functional aspects to mode of action. *Cell Communication and Signaling* **20**, 1-17 (2022).
213. A. Palecanda, L. Kobzik, Receptors for unopsonized particles: the role of alveolar macrophage scavenger receptors. *Current molecular medicine* **1**, 589-595 (2001).
214. A. Khanam, J. Yu, J. Zempleni, Class A scavenger receptor-1/2 facilitates the uptake of bovine milk exosomes in murine bone marrow-derived macrophages and C57BL/6J mice. *American Journal of Physiology-Cell Physiology* **321**, C607-C614 (2021).
215. V. Jaumouillé, C. M. Waterman, Physical constraints and forces involved in phagocytosis. *Frontiers in immunology* **11**, 1097 (2020).
216. D. Paul *et al.*, Phagocytosis dynamics depends on target shape. *Biophysical journal* **105**, 1143-1150 (2013).
217. J. A. Champion, S. Mitragotri, Role of target geometry in phagocytosis. *Proceedings of the National Academy of Sciences* **103**, 4930-4934 (2006).

218. S. Laus, A. Sour, R. Ruloff, E. Toth, A. E. Merbach, Rotational dynamics account for pH-dependent relaxivities of PAMAM dendrimeric, Gd-based potential MRI contrast agents. *Chemistry–A European Journal* **11**, 3064-3076 (2005).
219. C. Mondadori *et al.*, Advanced microfluidic models of cancer and immune cell extravasation: a systematic review of the literature. *Frontiers in bioengineering and biotechnology* **8**, 907 (2020).
220. J. Qiao *et al.*, Molecular imaging of EGFR/HER2 cancer biomarkers by protein MRI contrast agents. *JBIC Journal of Biological Inorganic Chemistry* **19**, 259-270 (2014).
221. J. Davies, P. Siebenhandl-Wolff, F. Tranquart, P. Jones, P. Evans, Gadolinium: pharmacokinetics and toxicity in humans and laboratory animals following contrast agent administration. *Archives of Toxicology*, 1-27 (2022).
222. K. J. Wolf, S. Kumar, Hyaluronic acid: incorporating the bio into the material. *ACS biomaterials science & engineering* **5**, 3753-3765 (2019).
223. P. M. Kharkar, K. L. Kiick, A. M. Kloxin, Designing degradable hydrogels for orthogonal control of cell microenvironments. *Chemical Society Reviews* **42**, 7335-7372 (2013).
224. C. C. Schuurmans *et al.*, Hydrolytic (In) stability of Methacrylate Esters in Covalently Cross-Linked Hydrogels Based on Chondroitin Sulfate and Hyaluronic Acid Methacrylate. *ACS omega* **6**, 26302-26310 (2021).
225. M. Yokoyama, K. Shiraishi, Stability evaluation of Gd chelates for macromolecular MRI contrast agents. *Magnetic Resonance Materials in Physics, Biology and Medicine* **33**, 527-536 (2020).
226. M. Rogosnitzky, S. Branch, Gadolinium-based contrast agent toxicity: a review of known and proposed mechanisms. *Biometals* **29**, 365-376 (2016).
227. F. Amyot *et al.*, A review of the effectiveness of neuroimaging modalities for the detection of traumatic brain injury. *Journal of neurotrauma* **32**, 1693-1721 (2015).
228. J. Szmydynger-Chodobska *et al.*, Posttraumatic invasion of monocytes across the blood—cerebrospinal fluid barrier. *Journal of cerebral blood flow & metabolism* **32**, 93-104 (2012).
229. J. Szmydynger-Chodobska, N. Strazielle, B. J. Zink, J.-F. Ghersi-Egea, A. Chodobski, The role of the choroid plexus in neutrophil invasion after traumatic brain injury. *Journal of Cerebral Blood Flow & Metabolism* **29**, 1503-1516 (2009).
230. D. Demeestere, C. Libert, R. E. Vandenbroucke, Clinical implications of leukocyte infiltration at the choroid plexus in (neuro) inflammatory disorders. *Drug discovery today* **20**, 928-941 (2015).
231. R. B. Meeker, K. Williams, D. A. Killebrew, L. C. Hudson, Cell trafficking through the choroid plexus. *Cell adhesion & migration* **6**, 390-396 (2012).
232. R. Shechter, A. London, M. Schwartz, Orchestrated leukocyte recruitment to immune-privileged sites: absolute barriers versus educational gates. *Nature Reviews Immunology* **13**, 206-218 (2013).
233. M. Feng, Assessment of blood-brain barrier penetration: in silico, in vitro and in vivo. *Current Drug Metabolism* **3**, 647-657 (2002).
234. P. Solár, A. Zamani, L. Kubíčková, P. Dubový, M. Joukal, Choroid plexus and the blood–cerebrospinal fluid barrier in disease. *Fluids and Barriers of the CNS* **17**, 1-29 (2020).
235. M. Klichinsky *et al.*, Human chimeric antigen receptor macrophages for cancer immunotherapy. *Nature biotechnology* **38**, 947-953 (2020).
236. S. Su *et al.*, Induced CAR-Macrophages as a Novel Therapeutic Cell Type for Cancer Immune Cell Therapies. *Cells* **11**, 1652 (2022).

237. P. Sun *et al.*, A smart nanoparticle-laden and remote-controlled self-destructive macrophage for enhanced chemo/chemodynamic synergistic therapy. *ACS nano* **14**, 13894-13904 (2020).
238. V. Alimardani *et al.*, Nanotechnology-based cell-mediated delivery systems for cancer therapy and diagnosis. *Drug Delivery and Translational Research*, 1-33 (2022).
239. P. Shi, N. Zhao, J. Coyne, Y. Wang, DNA-templated synthesis of biomimetic cell wall for nanoencapsulation and protection of mammalian cells. *Nature communications* **10**, 1-11 (2019).
240. D. Schmid *et al.*, T cell-targeting nanoparticles focus delivery of immunotherapy to improve antitumor immunity. *Nature communications* **8**, 1-12 (2017).
241. J. Weiden *et al.*, Robust Antigen-Specific T Cell Activation within Injectable 3D Synthetic Nanovaccine Depots. *ACS biomaterials science & engineering* **7**, 5622-5632 (2021).
242. C. Rodriguez-Mogeda *et al.*, Breaching Brain Barriers: B Cell Migration in Multiple Sclerosis. *Biomolecules* **12**, 800 (2022).
243. M. P. Stewart, A. Lorenz, J. Dahlman, G. Sahay, Challenges in carrier-mediated intracellular delivery: moving beyond endosomal barriers. *Wiley Interdisciplinary Reviews: Nanomedicine and Nanobiotechnology* **8**, 465-478 (2016).
244. M. M. Martin, L. Lindqvist, The pH dependence of fluorescein fluorescence. *Journal of Luminescence* **10**, 381-390 (1975).
245. C. Charpentier *et al.*, pH-Dependent Hydration Change in a Gd-Based MRI Contrast Agent with a Phosphonated Ligand. *Chemistry–A European Journal* **26**, 5407-5418 (2020).
246. A. Uosef *et al.*, Side effects of gadolinium MRI contrast agents. *Pediatria I Medycyna Rodzinna-Paediatrics and Family Medicine* **16**, 49-52 (2020).
247. S. Sabella *et al.*, A general mechanism for intracellular toxicity of metal-containing nanoparticles. *Nanoscale* **6**, 7052-7061 (2014).
248. A. Ukidve *et al.*, Erythrocyte-driven immunization via biomimicry of their natural antigen-presenting function. *Proceedings of the National Academy of Sciences* **117**, 17727-17736 (2020).
249. L. Wayteck, R. Xiong, K. Braeckmans, S. C. De Smedt, K. Raemdonck, Comparing photoporation and nucleofection for delivery of small interfering RNA to cytotoxic T cells. *Journal of Controlled Release* **267**, 154-162 (2017).
250. J. S. Brenner *et al.*, Red blood cell-hitchhiking boosts delivery of nanocarriers to chosen organs by orders of magnitude. *Nature communications* **9**, 1-14 (2018).
251. R. E. Cone, J. J. Marchalonis, R. T. Rolley, Lymphocyte membrane dynamics: metabolic release of cell surface proteins. *The Journal of Experimental Medicine* **134**, 1373-1384 (1971).
252. V. Francia, D. Montizaan, A. Salvati, Interactions at the cell membrane and pathways of internalization of nano-sized materials for nanomedicine. *Beilstein journal of nanotechnology* **11**, 338-353 (2020).
253. M. T. Stephan, J. J. Moon, S. H. Um, A. Bershteyn, D. J. Irvine, Therapeutic cell engineering with surface-conjugated synthetic nanoparticles. *Nature medicine* **16**, 1035-1041 (2010).
254. B. A. Pulaski, S. Ostrand-Rosenberg, Mouse 4T1 breast tumor model. *Current protocols in immunology* **39**, 20.22. 21-20.22. 16 (2000).

255. X. Wang, H. Zhang, X. Chen, Drug resistance and combating drug resistance in cancer. *Cancer Drug Resistance* **2**, 141 (2019).
256. T. L. Wiegand *et al.*, Translational neuroimaging in mild traumatic brain injury. *Journal of Neuroscience Research* **100**, 1201-1217 (2022).
257. T. M. Raimondo, D. J. Mooney, Functional muscle recovery with nanoparticle-directed M2 macrophage polarization in mice. *Proc Natl Acad Sci U S A* **115**, 10648-10653 (2018).
258. M.-A. Shahbazi *et al.*, Targeted Reinforcement of Macrophage Reprogramming Toward M2 Polarization by IL-4-Loaded Hyaluronic Acid Particles. *ACS Omega* **3**, 18444-18455 (2018).
259. J. Kim *et al.*, Use of nanoparticle contrast agents for cell tracking with computed tomography. *Bioconjugate chemistry* **28**, 1581-1597 (2017).
260. L. Tang *et al.*, Enhancing T cell therapy through TCR-signaling-responsive nanoparticle drug delivery. *Nat Biotechnol* **36**, 707-716 (2018).
261. H. I. Tong *et al.*, Monocyte Trafficking, Engraftment, and Delivery of Nanoparticles and an Exogenous Gene into the Acutely Inflamed Brain Tissue - Evaluations on Monocyte-Based Delivery System for the Central Nervous System. *PLoS One* **11**, e0154022 (2016).
262. R. Rodríguez-Rodríguez, H. Espinosa-Andrews, Z. Y. García-Carvajal, in *Functional Biomaterials*. (Springer, 2022), pp. 75-103.
263. T.-W. Wang *et al.*, Tailored design of multifunctional and programmable pH-responsive self-assembling polypeptides as drug delivery nanocarrier for cancer therapy. *Acta Biomaterialia* **58**, 54-66 (2017).
264. S. A. Abboud *et al.*, Enzyme-Cleavable Linkers for Protein Chemical Synthesis through Solid-Phase Ligations. *Angewandte Chemie International Edition* **60**, 18612-18618 (2021).
265. X. Guo *et al.*, Advances in redox-responsive drug delivery systems of tumor microenvironment. *Journal of Nanobiotechnology* **16**, 1-10 (2018).
266. D. Namgaladze *et al.*, Polarization of human macrophages by interleukin-4 does not require ATP-citrate lyase. *Frontiers in immunology* **9**, 2858 (2018).
267. C. B. Crayne, S. Albeituni, K. E. Nichols, R. Q. Cron, The immunology of macrophage activation syndrome. *Frontiers in immunology* **10**, 119 (2019).
268. I. R. Tizard, *Veterinary Immunology-E-Book*. (Elsevier Health Sciences, 2017).
269. N. Iwasaki *et al.*, Th2 cells and macrophages cooperatively induce allergic inflammation through histamine signaling. *Plos one* **16**, e0248158 (2021).
270. H. Wang *et al.*, Genetically engineered and enucleated human mesenchymal stromal cells for the targeted delivery of therapeutics to diseased tissue. *Nature biomedical engineering* **6**, 882-897 (2022).